

University of Belgrade  
Faculty of Physics

Jelena D. Pajović

**Biomolecule functionalized gold  
nanoparticles: photoexcitation processes  
and application in fluorescence  
microscopy**

Doctoral Dissertation

Belgrade, 2018

Univerzitet u Beogradu  
Fizički fakultet

Jelena D. Pajović

**Zlatne nanočestice funkcionalizovane  
biomolekulima: ispitivanje  
fotoekscitacionih procesa i primena u  
fluorescentnoj mikroskopiji**

Doktorska disertacija

Beograd, 2018

Mentor:

Dr Dušan K. Božanić, Senior Research Associate  
Vinča Institute of Nuclear Sciences  
University of Belgrade

Committee members:

Dr Dušan K. Božanić, Senior Research Associate  
Vinča Institute of Nuclear Sciences, University of Belgrade  
Dr Vladimir Đoković, Principal Research Fellow  
Vinča Institute of Nuclear Sciences, University of Belgrade  
Dr Slavica Maletić, Assistant Professor  
Faculty of Physics, University of Belgrade  
Dr Dušan Popović, Associate Professor  
Faculty of Physics, University of Belgrade

Thesis defense date: 15.10.2018.

---

# Acknowledgment

I would like to express my sincere gratitude to my mentor Dr Dušan K. Božanić and my co-mentor Dr Vladimir Đoković for their guidance, support, help and encouragement throughout my doctoral studies. Without their insightful suggestions and their endless patience, I could not have been where I am today. It has been my privilege to work with them and to learn from them (and not only about the research).

I am grateful to all of those whom I have had the pleasure to work with during this and other related projects. First in line is Dr Radovan Dojčilović, who has been a great team player in this pursuit of research. I express my enormous appreciation to my French scientific family, being DISCO crew at Synchrotron Soleil and friends. Thank you wholeheartedly Matthieu, Aleksandar, Frédéric, Gustavo, Suzie, François, Celine, Jade, Slavka and the rest, for making my two-year stay at the synchrotron an amazing experience and for making me feel very welcome (even though I did not speak any French). Also, my great appreciation goes to Julia, Estelle, Muriel, Anne-Marie and Jean-Marie for introducing me to the field of microbiology, and especially to Julia and Estelle for having fun even while doing microscopy late in the night during our beamtimes.

For several years during my PhD, I was a demonstrator in Laboratory of Physics I & II. I sincerely thank Prof Dr Đorđe Spasojević and to people whom he gathered around into an amazing team - Edi, Zoka, Čika Dule, Sveta, Nora, Kaća, Petar. Even though we were supposed to teach students, I learned a lot from Prof Đorđe about experiment design in physics. Also, I am profoundly grateful to Prof Dr Jablan Dojčilović and Dr Slavica Maletić for their support along my doctoral studies, as well as to Prof Dr Suzana Dimitrijević for teaching me my first steps in microbiology.

---



---

Additionally, I would like to thank all people at Laboratory for radiation chemistry and physics in Vinča Institute, especially Dr Vesna V. Vodnik, Dr Una Bogdanović and Dr Ivana Zeković who were always helpful throughout my experimental work done at the institute.

As I spent a very important part of my life in Petnica Science Center, where I did my first wanna-be scientific research, I owe a debt of gratitude to the incredible people who were there and made that possible.

I would also like to mention some admirable women who greatly influenced my educational path that I am very grateful for - Mirjana Ušak, Slavica Đukić, Ljiljana Vračar, late Desanka Lončar-Nikolić, Dr Jelena Grujić and Prof Dr Nataša Nedeljković.

Last but far from least, I would like to thank my friends and family whom I could always count on: Anđela, Saška, Vlada, Kaća, Milica, Erna, Tijana, Tamara, Tihana. Special thanks go to Marko, for being a great flatmate and support (not only but especially) in Gif sur Yvette and for all our night-long discussions on exactly everything. All of this would not be possible without endless support and encouragement of my parents Ljiljana and Dragomir, and my brother Filip, whom I am very proud of. Finally, thank you, Ivan, for being there for me.

Belgrade, June 2018

Jelena Pajović

---

---

## Abstract

In this dissertation, the investigation of the photoexcitation processes in hybrid nanostructures that comprise gold nanoparticles and fluorescent biomolecules (tryptophan and/or riboflavin) was carried out.

Transmission electron microscopy analysis showed that functionalization of the gold nanoparticles with tryptophan, riboflavin, and with both tryptophan and riboflavin did not affect the initial spherical shape of the nanoparticles. The average size of the fabricated nanostructured particles was approximately 8 nm. The study of the biomolecule-gold interactions by Raman spectroscopy revealed that the interaction at the interfaces takes place *via* indole functional groups (tryptophan) and benzene ring (riboflavin). Valence-level electronic structure of the hybrid nanomaterial was studied by vacuum-ultraviolet photoelectron spectroscopy on isolated nanoparticles and it was demonstrated that the adsorption of the biomolecule on the nanoparticle surface induces a shift of the Au 5*d* level toward lower binding energies. The investigation of the optical properties of the fabricated nanostructures revealed that photoluminescent properties of the biomolecules are preserved upon conjugation of the gold nanostructures. Tryptophan and riboflavin are a pair of molecules which, when in proximity to each other, exhibit resonance energy transfer (RET) upon excitation. It was shown that the efficiency of the RET is significantly improved if these molecules are immobilized on the surfaces of the gold nanoparticles than in the case when they were mixed in a solution. Deep-ultraviolet fluorescence microscopy was used to elucidate preferential locations of the functionalized nanoparticles in bacteria *Escherichia coli*, fungus *Candida albicans* and human hepatocellular carcinoma-derived cell line Huh7.5.1. By analysing the spatial distribution of the fluorescence signal, it was shown that the fabricated nanomaterials internalise in the cells. The property of bifunctionalized gold nanoparticles to efficiently transfer energy between tryptophan and riboflavin was employed as an additional criterion of distinguishing the fluorescence signal that originates in the nanostructures from the autofluorescence of the cancer cells. This method enabled localization of the RET nanostructures within the cells, even though the particles were of smaller size than the spatial resolution of the experimental set up.

---

---

**Keywords:** gold nanoparticles, functionalization, biomolecules, fluorophores, gas-phase vacuum-ultraviolet photoemission, DUV fluorescence microscopy, inorganic fluorescent probes, metal nanoparticles enhanced resonance energy transfer

**Scientific field:** Physics

**Scientific subfield:** Condensed matter physics and statistical physics

**UDC number:**

---

---

## Sažetak

U ovoj doktorskoj disertaciji izloženi su rezultati istraživanja fotoekscitacionih procesa u hibridnim nanostrukturama baziranih na zlatnim nanočesticama funkcionalizovanih biomolekulima triptofanom i riboflavinom.

Transmissionom elektronskom mikroskopijom pokazano je da funkcionalizacija nanočestica zlata triptofanom, riboflavinom i istovremeno triptofanom i riboflavinom nije uticala na promenu sfernog oblika nanočestica. Srednji prečnik dobijenih struktura je oko 8 nm. Analiza interakcije između biomolekula i nanočestica korišćenjem Raman spektroskopije pokazala je da se interakcija na granici između nanočestice i biomolekula odvija preko indol grupe (triptofan) i benzenskog prstena (riboflavin). Valentna elektronska struktura hibridnog nanomaterijala analizirana je pomoću fotoelektronske spektroskopije u vakuum-ultraljubičastom delu elektromagnetnog spektra na izolovanim nanočesticama u gasnoj fazi. Pokazano je da adsorpcija biomolekula na površinu nanočestica prouzrokuje pomeranje  $5d$  nivoa zlata ka nižim vezivnim energijama. Istraživanje optičkih osobina funkcionalizovanih nanostrukture potvrdilo je da su fotoluminescentne osobine biomolekula očuvane nakon njihove adsorpcije na površinu nanočestica. Triptofan i riboflavin čine par fluoroformora između kojih dolazi do rezonantnog transfera energije prilikom ekscitacije triptofana. Pokazano je da je efikasnost transfera značajno poboljšana u slučaju kada se biomolekuli nalaze na površini zlatnih nanočestica nego kada su u čistom rastvoru. Fluorescentna mikroskopija sa pobudom u ultraljubičastom delu elektromagnetnog spektra korišćena je za određivanje položaja nanočestica unutar bakterija *Escherichia coli*, gljiva *Candida albicans*, kao i u ćelijama raka jetre Huh7.5.1. Analizom prostorne distribucije fluorescentnog signala, pokazano je da dolazi do internalizacije nanostrukture unutar ćelijskih linija. Svojstvo bifunkcionalizovanih nanočestica zlata da efikasno prenose energiju sa triptofana na riboflavin iskorišćeno je kao dodatni kriterijum za razlučivanje fluorescentnog signala koji potiče od nanostrukture od autofluorescence ćelija. Ovaj metod je omogućio lokalizaciju nanostrukture koje ispoljavaju rezonantni prenos energije unutar ćelija, iako su čestice manje od prostorne rezolucije korišćenog mikroskopa.

---

---

**Ključne reči:** zlatne nanočestice, funkcionalizacija, biomolekuli, fluorofore, VUV fotoelektronska spektroskopija u gasnoj fazi, DUV fluorescentna mikroskopija, rezonantni prenos energije pojačan metalnim nanočesticama

**Naučna oblast:** Fizika

**Uža naučna oblast:** Fizika kondenzovane materije i statistička fizika

**UDK broj:**

---

---

# Contents

<b>1</b>	<b>Introduction</b>	<b>1</b>
<b>2</b>	<b>Hybrid nanosystems based on gold nanoparticles and biomolecules</b>	<b>5</b>
2.1	Noble metal nanoparticles . . . . .	5
2.1.1	Electronic structure of gold and its implication to the electronic properties of gold nanoparticles . . . . .	6
2.1.2	Optical properties of noble metal nanoparticles . . . . .	11
2.2	Interaction of noble metal nanoparticles and fluorophores . . . . .	28
2.3	Functionalization of noble metal nanoparticles . . . . .	38
2.3.1	Functionalization of gold nanoparticles . . . . .	39
2.3.2	Functionalization of gold nanoparticles with biomolecules . . . . .	43
2.3.3	Electronic structure of surface-modified gold nanoparticles . . . . .	45
2.4	Application of biomolecule-functionalized gold nanoparticles in bionanotechnology . . . . .	51
2.4.1	Biosensors based on gold nanoparticles . . . . .	51
2.4.2	Microscopy techniques involving gold nanolabelling - bioimaging . . . . .	54
2.4.3	Other applications of gold nanoparticles in bionanotechnology . . . . .	59
2.4.4	Fluorophore-bifunctionalized gold nanoparticles and nanogold influence on fluorescent properties of the fluorophore-pair . . . . .	61
<b>3</b>	<b>Sample preparation, experimental techniques and methods</b>	<b>70</b>

---

---

3.1	Sample preparation . . . . .	70
3.1.1	Synthesis of functionalized gold nanoparticles . . . . .	70
3.2	Characterization of functionalized gold nanoparticles . . . . .	73
3.2.1	Size and morphology of functionalized gold nanoparticles . . . . .	73
3.2.2	Electronic structure characterization of functionalized gold nanoparticles . . . . .	73
3.2.3	Optical properties of functionalized gold nanoparticles . . . . .	75
3.3	Deep-UV fluorescence microscopy of biological samples incubated with functionalized gold nanoparticles . . . . .	76
3.3.1	Preparation of biological samples for deep UV imaging . . . . .	76
3.3.2	Deep-UV fluorescence microscopy . . . . .	77
<b>4</b>	<b>Physical characterization of functionalized gold nanoparticles</b>	<b>80</b>
4.1	Size and morphology of functionalized gold nanoparticles . . . . .	81
4.2	Characterization of the electronic structure of functionalized gold nanoparticles . . . . .	81
4.2.1	Raman spectroscopy . . . . .	82
4.2.2	Photoelectron spectroscopy of free-standing functionalized gold nanoparticles . . . . .	89
4.3	Optical properties of functionalized gold nanoparticles . . . . .	96
4.3.1	Ultraviolet-visible absorbance spectroscopy . . . . .	97
4.3.2	Photoluminescence spectroscopy . . . . .	99
<b>5</b>	<b>Application of tryptophan and riboflavin functionalized gold nanoparticles in fluorescence microscopy</b>	<b>107</b>
5.1	Tryptophan-functionalized gold nanoparticles as fluorescence probes for imaging of bacteria <i>Escherichia coli</i> . . . . .	108
5.2	Riboflavin-functionalized gold nanoparticles as fluorescence probes for imaging of fungus <i>Candida albicans</i> . . . . .	111

---

---

5.3	Fluorescence imaging study of human hepatocellular carcinoma-derived Huh7.5.1 cells incubated with gold nanoparticles bifunctionalized by tryptophan and riboflavin . . . . .	114
<b>6</b>	<b>Conclusion</b>	<b>136</b>

---



---

# Chapter 1

## Introduction

Nanotechnology is a fast-growing research area because it opens a completely new perspective in material design [1]. More specifically, in comparison to conventional materials, the materials composed of particles of nanometre dimensions, i.e. the nanoparticles, exhibit a new set of physical properties as a direct consequence of their size. These characteristics include specific optical, electric, catalytic and thermal properties tuneable through changing the particle dimensions. Additionally, the nanomaterials can be easily modified by functionalization with a variety of molecules, which enables adaptations of a nanomaterial for specific applications in industry or medicine. In noble-metal nanoparticles (MNPs), the confined electron motion in the nanostructured volume results in the appearance of novel optical, electrical, catalytic and other properties that are different from the properties of their bulk counterparts. Characteristic optical properties of MNPs are the consequence of the pronounced contribution of surface plasmons to the interaction with external electromagnetic field. The surface plasmon resonance of the MNPs depends on the nanoparticles size, shape and the environment, and it is observed as a new absorption maximum in the visible domain of the electromagnetic spectrum.

Gold nanoparticles (Au NPs) are the most studied metal nanostructures [2, 3, 4, 5]. With respect to the other metal nanoparticles, they are relatively cheap and exhibit good chemical stability. Au NPs are very attractive for the application in biotechnology due to their biocompatibility, low cytotoxicity [6, 7] and sensitivity of the surface plasmon resonance to environmental influences. As gold interacts with

numerous biologically relevant molecules [8, 9, 10], gold nanoparticles do not possess any selectivity in the interaction with living biosystems. In turn, their reactivity makes nanosized gold an extraordinary platform for building complex entities. By adsorbing biomolecules on their surfaces, i.e. by their functionalization, it is possible to create the hybrid nanostructure with particular properties.

Functionalized Au NPs have been applied in different fields of biomedicine, including sensing [11, 12, 13, 14], microscopy [15, 16], and various cancer therapies (photothermal [17, 18], radio [19], photodynamic [20]). Specifically, low photostability of commercially available dyes for fluorescence microscopy of tissues and living cells resulted in developments of inorganic fluorescence nanoprobcs. Gold nanoparticles are highly promising materials in this type of research since they exhibit high stability and low cytotoxicity, while at the same time they can be easily functionalized by a variety of biomolecules. The interaction of functionalized gold nanoparticles with biological systems depends on the type of molecules used for functionalization [21]. For this reason, it is necessary to characterize the functionalized nanostructures prior to studying their interaction with the investigated biological systems [22]. Additionally, as the size reduction imposes new technological and experimental challenges, it is of high importance to explore new approaches for the analyses and characterization of functionalized nanomaterials.

In this doctoral dissertation, we present the results of our investigation of the photoexcitation processes of biocompatible fluorescent hybrid nanostructures that comprise gold nanoparticles and biomolecules tryptophan (amino acid) and/or riboflavin (vitamin). Also, we investigate these nanostructures as possible fluorescent probes for deep-ultraviolet fluorescence microscopy. The starting material, the gold nanoparticles, does not possess fluorescent properties. For that reason, we have developed methods for functionalization of nanoparticles with fluorescent biomolecules. The obtained hybrid nanostructures absorb and emit light in the UV part of the electromagnetic spectrum, which makes them good candidates for the role of fluorescent probes in deep-UV microscopy. Functionalized gold nanoparticles are analysed by a variety of spectroscopic methods. The fluorescence properties are mainly determined by the electron valence levels and they are studied by vacuum-ultraviolet

---

photoelectron spectroscopy. This approach provides information about the valence electronic structure of the components of our nanosystems (with the respect to the vacuum level), as well as about the changes in valence structure induced by their mutual interaction. The interaction of the biomolecules with gold nanoparticles is also investigated by Raman spectroscopy, whereas the functionalization of the nanoparticles is determined by the absorbance spectroscopy. The fluorescence properties of free biomolecules and biomolecule functionalized gold nanoparticles are studied by photoluminescence spectroscopy. Photoluminescence spectroscopy is also used to study the resonance energy transfer between tryptophan and riboflavin molecules in the solution and when they are attached to the surface of gold nanoparticles. The functionalized gold nanoparticles are investigated as potential fluorescence probes for DUV imaging of cells. They are tested on bacteria *Escherichia coli*, fungus *Candida albicans*, and human hepatocellular carcinoma-derived cell line Huh7.5.1. It is shown that the functionalized gold nanoparticles can be employed as luminescent tag for various biological systems. Furthermore, we demonstrate a novel approach for the detection of the nanostructures that are smaller than the resolution of deep-ultraviolet fluorescence microscopy set-up.

The thesis is organized as follows: Chapter 2 gives the overview of the literature results on the physical properties of metal nanoparticles and on their functionalization by fluorescent biomolecules. The influence of the nanoparticle-biomolecule interaction on the electronic structures of the bands of each of the constituents, and consequently on the optical properties of the fluorescent nanostructures are discussed. Special attention is given to the applicability of metal nanoparticles as emerging material in nanomedicine. In Chapter 3, the procedures for the synthesis and functionalization of gold nanoparticles employed in this work are presented. The experimental techniques used in the characterisation of the hybrid nanostructures are explained in detail. The results of the physical characterisation of the functionalized gold nanoparticles are discussed in Chapter 4. It covers biomolecule-gold nanoparticles interaction and the optical properties of the hybrid nanostructures. Finally, the results of the deep-ultraviolet fluorescence microscopy investigations of bacteria *Escherichia coli*, fungus *Candida albicans*, and human hepatocellular

---

carcinoma-derived Huh7.5.1 cells incubated with functionalized gold nanoparticles are presented in Chapter 5. The concluding remarks and the future prospects are given in Chapter 6.

---

## Chapter 2

# Hybrid nanosystems based on gold nanoparticles and biomolecules

In this Chapter, we present a review of the literature on the properties of metal nanoparticles (MNPs), their interaction with the environment, standard functionalization procedures, as well as the metal's influence on the general properties of the hybrid nanomaterial. We will also mention some applications of the functionalized metal nanoparticles in bionanotechnology, with a short overview on the resonance energy transfer (RET) between the pair fluorophores, and how MNPs affect the RET efficiency.

### 2.1 Noble metal nanoparticles

Nanoparticles can be any solid-state material with at least one dimension that is smaller than 1 micrometre. However, for the sake of univocally relating the characteristic dimension with their characteristic properties, in using the term nanoparticles we will consider only crystals of nanometre size that exhibit properties that are different than that of the macroscopic crystals of the same substance. The particle properties change continuously with a decrease in the crystal size. Below certain characteristic dimension, which depends on the type of material, the particle properties start to behave discretely, ending in an atom-like behaviour [23]. In this sense, the nanoparticle properties bridge the gap between the corresponding characteristics

of atoms or molecules and the solid state material [23, 24, 25].

The reason behind the continuous change in the particle properties with the change in size is in a continuous change in the ratio between the number of surface atoms and total number of atoms in a particle. In the case of macroscopic crystals, this ratio is close to zero, whereas for nanoclusters, comprised of few atoms, the ratio is almost one. This means that the surface phenomena contribute largely to the macroscopic properties of nanomaterials. For this reason, certain properties of the nanoparticles can be extrapolated from that of thin films of the same material [26]. When the nanoparticles are smaller than de Broglie wavelength of an electron in the particular crystal, which is typically of order of few nanometres, the electrons are confined in a nanoparticle volume that manifests as quantization effects in the energy distribution. In this case, the particles start to behave more like clusters of atoms than the macroscopic crystal. In the case of metal nanoparticles, the characteristic dimension is below 1 nm and this effect is called a metal-insulator transition.

### **2.1.1    Electronic structure of gold and its implication to the electronic properties of gold nanoparticles**

Noble metal elements, copper, silver and gold, belong to the 11th group of the Periodic table of elements. All three elements have  $(n - 1)d^{10}ns^1$  electronic configuration. Due to relativistic effects in heavy atoms,  $s$  (hybridized  $s-p$ ) shells tend to contract and stabilize, while  $d$  and  $f$  shells expand and destabilize [8, 27, 28]. As shown in Figure 2.1, these effects are the most pronounced in gold and they are responsible for a number of fine differences between otherwise very similar silver and gold atoms [28]. Furthermore, these effects allow electrons from  $(n - 1)d$  level to participate in bonding, which explains why gold atoms can have different oxidation states (up to +5), whereas silver is monovalent.

For the core atoms of nanoparticles, the lattice symmetry is conserved, e.g. lattice structure for noble metal nanoparticles is face-centered cubic, as it is for the macroscopic crystal. At room temperature, the lattice parameter of Au fcc

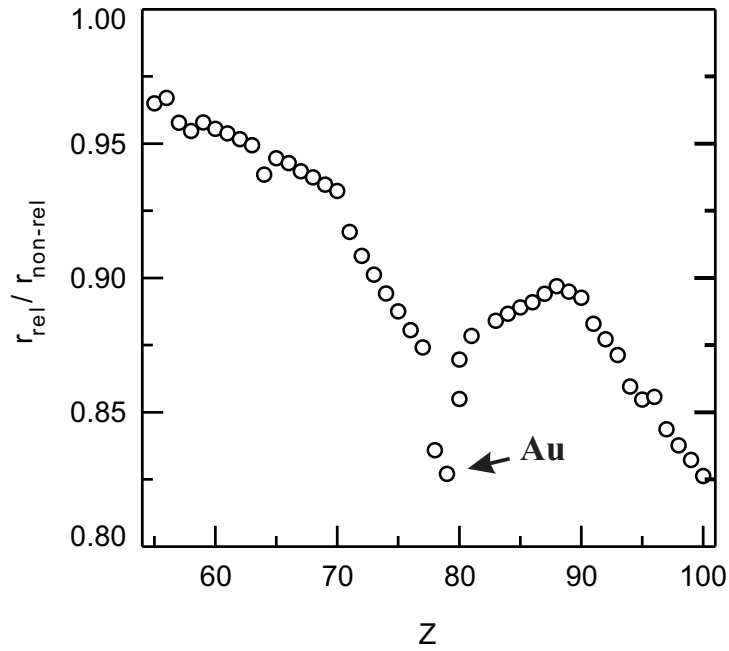


**Figure 2.1:** The relativistic contraction of the 6s shell in the elements from Cs ( $Z = 55$ ) to Fm ( $Z = 100$ ), shown as a ratio of the diameter of contracted ns orbital due to relativistic effect and nonrelativistic ns orbital as a function of the atomic number of elements. Taken from Ref. [28].

macroscopic crystal is 4.083 Å. Under the same conditions, gold nanoparticles show broadening of the diffraction peaks due to the size-induced strain in the crystal structure, while the lattice parameter of the nanoparticles does not show observable changes [29]. This indicates that in an analysis of energy bands of nanoparticles, a good starting point is the energy band distribution observed for the corresponding macroscopic crystals.

As already mentioned, the relativistic effects are the most pronounced in gold, therefore the calculations of this type will be considered. Ramchandani calculated energy band structure of gold crystals in both non-relativistic and relativistic regime [30]. The calculations were performed by employing the augmented plane wave method in a potential of muffin-tin type and the crystal potential was a superposition of 14 nearest atoms potentials in the fcc lattice. The Figure 2.2 shows the distribution of the number of electrons per atom per eV in bulk gold as a function of their energy. The histogram basically reflects the density of states (DOS) of electrons in Au fcc. The valence band structure was experimentally measured by Shirley

using high-resolution X-ray photoelectron spectroscopy (XPS) of single gold crystals at Al K radiation (1486 eV) photon energy [31], and the corresponding photoelectron spectrum (PES) is presented in Figure 2.2(b). By comparing the experimental PES with the theoretical DOS, it can be seen that the relativistic effect have to be considered for proper analysis of energy bands of gold crystals. Additionally, it was shown that the  $5d$  band starts at 2.04 eV below the Fermi level. A better resolution in the PES was achieved by a decrease in the photon energy.

The PES experimental data by Eastman and Cashion [32], obtained with the photon energies of 10.2, 11.6, 16.8, 21.2 and 26.9 eV, are shown in Figure 2.2(c). It can be seen that the  $5d$  band consists of 5 peaks with two main peaks positioned at 2.5 and 3.7 eV below the Fermi energy. Three low intensity peaks at 5.1, 5.8 and 6.3 eV were observed for the probing photons of 16.8 eV, as well as the bottom of  $5d$  band was observed at 7.8 eV below the Fermi energy. It was also noticed that with increasing in energy of the radiation, there is a lower contribution of the  $6s$  electrons to PES with respect to the contribution of  $5d$  electrons.

The photoelectron spectra, which represent the band structure of a given crystal, is highly sensitive to the experimental conditions, such as the photon energy or the incidence angle. The choice of the radiation energy, and consequently the range of the kinetic energy of the photoelectrons, defines the depths from which electrons can escape the material. At Al  $K\alpha$  radiation, the electron escape depth is around 2 nm, indicating that the XPS is a surface technique. The effect of the incidence angle on the PE spectra is pronounced in the case of the single crystals, where the angle defines the crystal plane that is exposed to the incident radiation. In the case of polycrystalline samples, on the other hand, the material is characterized by the presence of grain boundaries where atoms have low coordination. Consequently, the band structure of a polycrystalline sample would more closely resemble that of a corresponding nanoparticle.

Reported PE spectra of metal polycrystalline samples showed appearance of a shoulder close to the peak of electron bands that was shifted by  $\approx 0.4$  eV toward the Fermi level [33, 34, 35]. This was attributed to the surface effects, since surface atoms have narrower bands slightly shifted toward lower binding energies [33]. In addition,



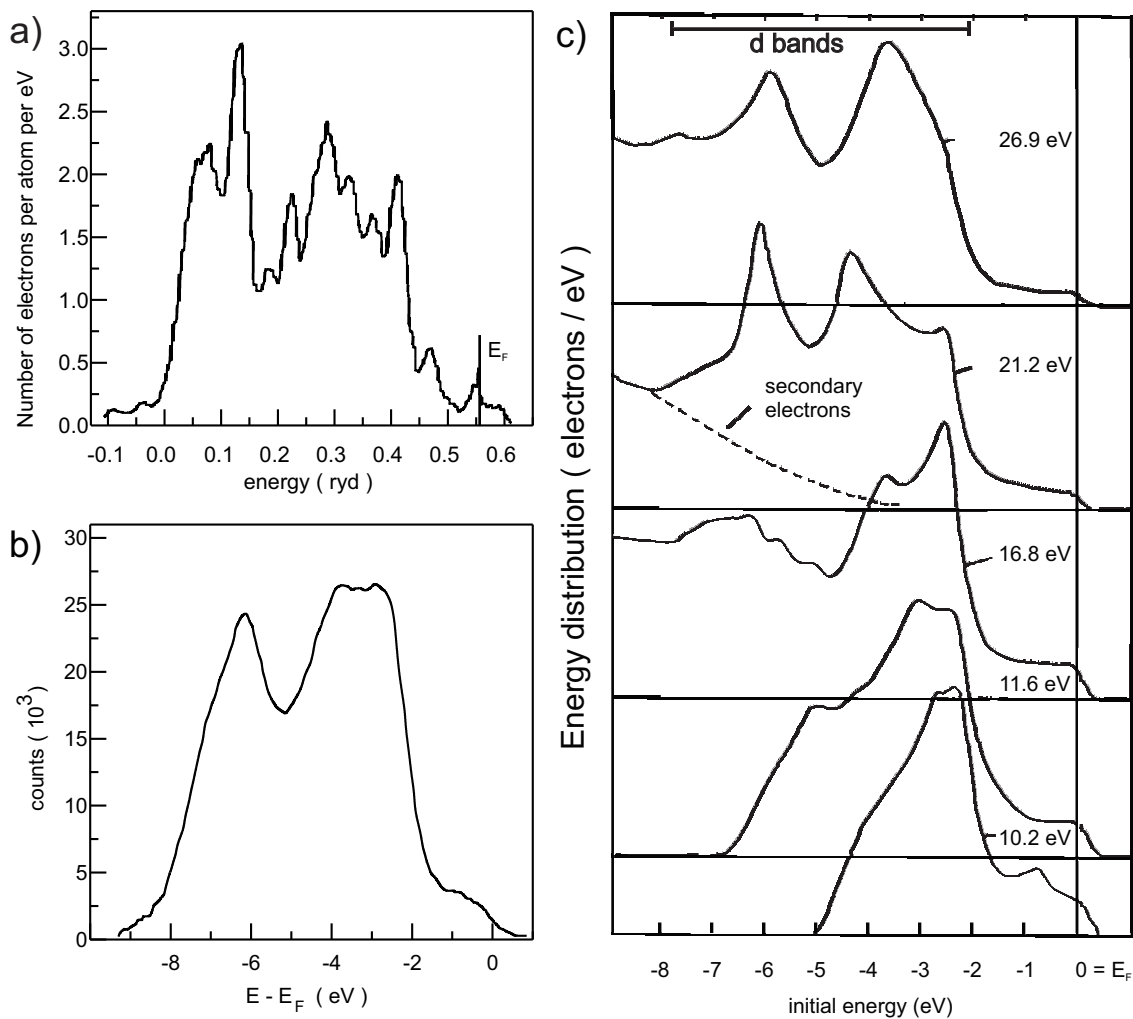


**Figure 2.2:** a) Theoretical density of states histogram calculated using relativistic augmented plane wave method. Energies are in rydbergs (1 ryd = -13.6 eV). Taken from Ref. [30]. (b) X-ray photoelectron spectrum of the gold valence bands by using Al K radiation and a single-crystal specimen. Taken from Ref. [31]. (c) Photoelectron spectra for gold, plotted versus the initial-state energy, with  $E_F$  set to zero. Taken from Ref. [32].

some levels show narrower bands with respect to the same levels for the atoms in bulk [33]. In the case of nanoparticles, which possess large number of the surface atoms, the mentioned effects will be overall even more pronounced. Visikovskiy *et al.* reported on electronic *d*-band properties of gold nanoclusters placed on the amorphous carbon [36]. They analysed the dependence of the photoelectron emission from *4f* and *5d* bands on the estimated number of atoms per nanocluster (from 11 to 1630 atoms) in the case of gold hemispheres grown on carbon. These results are presented in Figure 2.3. The binding energy of the bands was higher than for bulk value, and monotonically increased with a decrease in the cluster size. Interestingly, as the number of atoms in a cluster fell below 150 atoms per cluster, the position of *5d* band showed a steady increase of its binding energy, as shown in Figure 2.3, left axis. Furthermore, it was also shown that the  $4f_{7/2}$  levels changed in the same manner as the position of *5d* bands (Figure 2.3, right axis). However, for clusters consisting of more than 150 atoms, the binding energies for *5d* and *4f* levels remained virtually constant. Various mechanisms were suggested for this sudden change in energy. These include the change in the coordination number of the atoms in clusters, the contraction of Au-Au bonds, and the dynamic final state effects and nanoparticle-substrate interaction. The later two mechanisms were also identified by Hövel *et al.* [37]. They showed that the sharpness of Fermi level of silver clusters on graphite is influenced by photohole-substrate interaction at times of the order of femtoseconds. Similar experiment was carried out by Tanaka *et al.* with 5 nm silver nanoparticles passivated by dodecanethiolates and deposited on highly oriented pyrolytic graphite [38]. It was found that the steep slope of the *5s* band away from Fermi level is due to final-state effect, e.g. creation and neutralization of a photohole created after the ejection of photoelectron. The creation of a photohole shifts the energy of the corresponding photoelectron, while the neutralization process occurs *via* electron tunnelling from the substrate through the passivant.

As it will be seen in Section 4, within the experimental work conducted as a part of this thesis, we measured valence photoelectron spectra of isolated gold nanoparticles for the first time. These results provide direct information on the electronic structure of gold nanoparticles without the influence of the substrate.

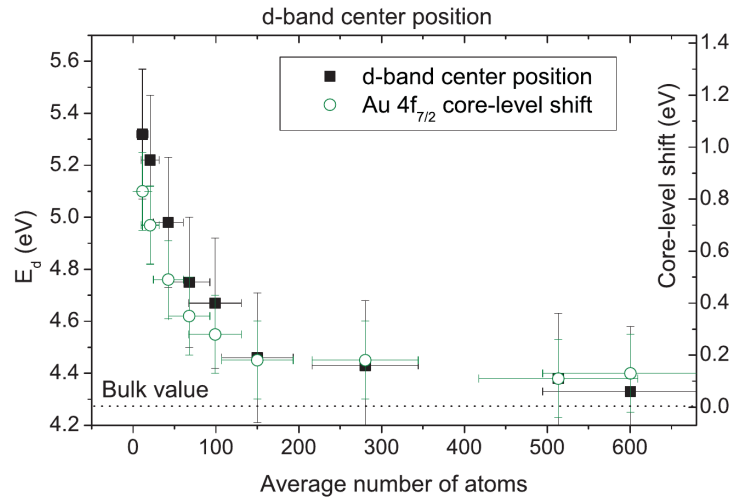


**Figure 2.3:** Experimentally derived position of the  $5d$  band (left axis) and the Au  $4f_{7/2}$  core-level shift (right) depending on the cluster size of gold nanoclusters grown on amorphous carbon supports. Taken from Ref. [36]

## 2.1.2 Optical properties of noble metal nanoparticles

Crystals of noble metals are of well-known colours. For copper and silver, it is popularly called metallic, meaning shiny. This is due to their bulk plasmon lying in ultraviolet part of the electromagnetic spectrum (3.5 eV for Ag with the respect to the  $E_F$ ), and therefore radiation below that value is being absorbed, while the rest is reflected on the surface. In the case of gold, again, it is golden in colour. Bulk plasmon for gold crystal is in green part of the spectrum (2.8 eV with the respect to the  $E_F$ ), and the crystal absorbs the blue and violet part of the radiation, while reflecting yellow and red [24, 25]. As it will be seen further in text and in Chapter 4, the optical properties of gold nanoparticles differ from that of the macroscopic crystals. In addition, they depend on the nanoparticle size, shape and environment. This characteristic behaviour will prove very valuable in accessing information on the investigated nanosystems by UV-absorption spectroscopy.

Optical properties of metal crystals can be described *via* their dielectric response to the external electromagnetic field [39, 40, 41]. The response is determined by the behaviour of free electron gas in the lattice (plasma sea), which consists of delocalized valence electrons of lattice metal atoms. The contribution of the ionic atom cores in lattice points is included through a modification of the effective mass of the free

electrons. Once exposed to the external EM radiation ( $E$ ), microscopic dipoles inside the material align, causing macroscopic polarization of the material. This polarization per unit volume is described by the polarization field  $P$ . The relation between  $P$  and  $E$  defines optical response of the metal and can be represented (in a linear regime) as:

$$\mathbf{P}(\mathbf{r}, t) = \int dt' \int d^3\mathbf{r}' \check{\chi}(\mathbf{r}; \mathbf{r} - \mathbf{r}'; t - t') \cdot \mathbf{E}(\mathbf{r}', t') \quad (2.1)$$

where  $\check{\chi}$  is dielectric susceptibility tensor. This can be simplified with the assumptions that the material is isotropic and has a locality in space (i.e. the polarization at a given point is determined by the electric field at the same point in space), which is a good approximation in this case [40]. Then, polarization field can be written as

$$\mathbf{P}(\mathbf{r}, t) = \int dt' \chi(\mathbf{r}; t - t') \cdot \mathbf{E}(\mathbf{r}, t') \quad (2.2)$$

where  $\chi$  represents the scalar dielectric susceptibility. Using Fourier transform to switch from time to frequency coordinate, the last equation becomes:

$$\tilde{\mathbf{P}}(\mathbf{r}, \omega) = \tilde{\chi}(\mathbf{r}, \omega) \cdot \mathbf{E}(\mathbf{r}, \omega). \quad (2.3)$$

The macroscopic Maxwell's equation that connects polarization field  $\mathbf{P}$  to the electric displacement field  $\mathbf{D}$ ,  $\mathbf{D} = \mathbf{E} + 4\pi\mathbf{P}$  can also be transferred to Fourier space:

$$\tilde{\mathbf{D}}(\mathbf{r}, \omega) = \tilde{\varepsilon}(\mathbf{r}, \omega) \cdot \mathbf{E}(\mathbf{r}, \omega) \quad (2.4)$$

where  $\tilde{\varepsilon}$  is complex dielectric relative permittivity of the medium. Therefore, it is given as:

$$\tilde{\varepsilon}(\mathbf{r}, \omega) = 1 + 4\pi\tilde{\chi}(\mathbf{r}, \omega). \quad (2.5)$$

In the free electron model, the interaction of the electrons in the plasma sea with the external electromagnetic field can be observed from a point of noninteracting particles in which the electron movement is influenced only by collisions with fixed ions that are described by damping factor  $\Gamma$ . This quantity is inversely proportional

to the average time between two collisions. If the moving of the electron along the  $x$  direction is influenced by the external EM field of the form  $E_x(t) = \text{Re}[E_0 e^{-i\omega t}]$ , the kinetics of the electron may be represented by the following formula:

$$m_e^* \frac{d^2 x(t)}{dt^2} + m_e^* \Gamma \frac{dx(t)}{dt} = -e \text{Re}[E_0 e^{-i\omega t}]. \quad (2.6)$$

Particular solution of the former equation gives the expression for the electron oscillations induced by the external EM field:

$$x(t) = \text{Re}[\tilde{x}_0 e^{-i\omega t}]. \quad (2.7)$$

Taking into account that there can be a phase shift between  $\mathbf{E}_0$  and the medium response, the complex amplitude  $\tilde{x}_0$  is given as:

$$\tilde{x}_0 = \frac{e}{m_e^* (\omega^2 + i\Gamma\omega)} E_0. \quad (2.8)$$

Summing the displacements of all  $N$  electrons in the gas, macroscopic polarization field in  $x$  direction is obtained as:

$$P_x(t) = -eNx(t) = -\text{Re} \left[ \frac{Ne^2}{m_e^* (\omega^2 + i\Gamma\omega)} E_0 e^{-i\omega t} \right]. \quad (2.9)$$

Finally, the expression for the dielectric function can be written as:

$$\tilde{\varepsilon}(\omega) = 1 - \frac{4\pi Ne^2}{m_e^* (\omega^2 + i\Gamma\omega)} = 1 - \frac{\omega_p^2}{\omega^2 + i\Gamma\omega}. \quad (2.10)$$

where  $\omega_p$  represents volume plasma frequency and  $\omega_p^2 = 4\pi Ne^2/m_e^*$ . The former expression for  $\tilde{\varepsilon}(\omega)$  is known as Drude free-electron model for metals [39]. When material is exposed to the radiation of the same frequency as the volume plasma frequency  $\omega_p$ , its complex dielectric constant becomes close to zero. Therefore, the polarization field becomes  $\mathbf{P} = -\mathbf{E}/4\pi$ , and it consequently becomes pure depolarization field. If every electron is slightly shifted in one direction, the fixed ions in the lattice will create a Coulomb restoring force. Consequently, the electron gas starts to oscillate in the lattice. This effect is called the bulk plasmon and it

represents the free electron gas oscillation inside a metal crystal.

The equation 2.10 can be written in the following form:

$$\tilde{\varepsilon}(\omega) = 1 - \frac{\omega_p^2}{\omega^2 + \Gamma^2} + i \frac{\omega_p^2 \Gamma}{\omega(\omega^2 + \Gamma^2)} \equiv \varepsilon_1(\omega) + i\varepsilon_2(\omega) \quad (2.11)$$

which separates the real and imaginary part of  $\tilde{\varepsilon}$ . Quantities  $\varepsilon_1$  and  $\varepsilon_2$  are related to the complex refractive index of the material as  $\tilde{\varepsilon}(\omega) = \tilde{n}^2$ , where  $\tilde{n} = n + ik$  ( $n$  is the refractive index of the material, while  $k$  is the attenuation coefficient of light inside the material and is called extinction coefficient). An example of the Drude model and experimentally obtained variables related to the metal dielectric function are shown in Figure 2.4. Figure 2.4(a) shows  $\varepsilon_1$  and  $\varepsilon_2$ , the associated complex refractive index and the normal reflectance as the function on the photon frequency for Drude model in the case when  $\Gamma < \omega_p$ , while experimentally obtained values for silver are represented in Figure 2.4(b). Some discrepancies are noticeable between the theoretical prediction and experimental results. They originate from contributions of the inter-band transitions to the imaginary part of the experimentally obtained dielectric function, which are manifested as losses due to absorbance of external radiation.

For metals, the values of the coefficient  $\hbar\Gamma$  are usually between 0.02 and 0.07 eV [42]. So, in most of the cases  $\omega_p \gg \Gamma$  and  $\tilde{\varepsilon}$  the can be approximated by:

$$\tilde{\varepsilon}(\omega) \approx 1 - \frac{\omega_p^2}{\omega^2}. \quad (2.12)$$

This expression describes the motion of the pure free electron gas in a metal, without dissipation. In this case, the negligible imaginary part of  $\tilde{\varepsilon}$  also means negligible absorption. For radiation with lower frequency than  $\omega_p$ , pure free electron gas behaves as a perfect mirror and for the frequencies higher than, it is almost completely transparent.

For alkali metals (Li, Na, K, Cs, Rb), Drude model for dielectric function is in good agreement with the experiments. But, for noble metals, the electrons from  $ns1$  shell do not behave as a perfect free electron gas. Due to already-mentioned relativistic effects, which are most pronounced in gold, there is a decrease in the

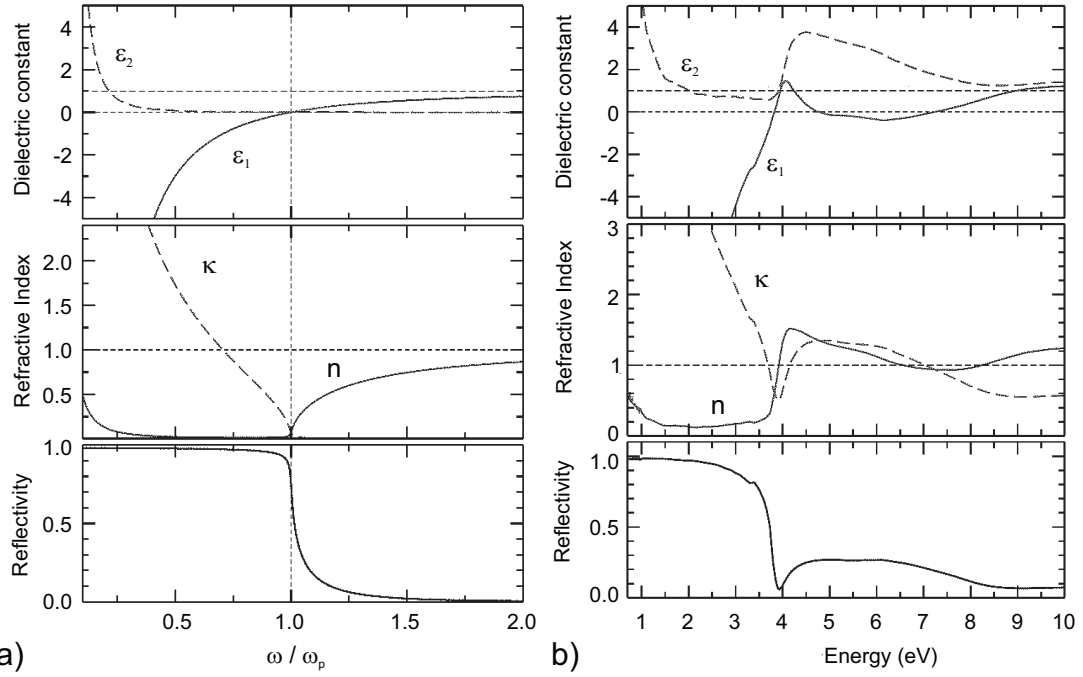


**Figure 2.4:** a) Dielectric function, refractive index and reflectivity of a simulated Drude model for perfect metal, for  $\hbar\omega_p = 10$  eV,  $\hbar\Gamma = 0.1$  eV. (b) Experimental dielectric function, refractive index and reflectivity of silver crystal. Taken from Ref. [40].

energy gap for the inter-band transition from  $(n - 1)d$  level to the conduction band [33]. In the case of gold, the gap width is around 2 eV [42, 43]. Consequently, this contribution has to be taken into account when studying the absorption behaviour of noble metals in the optical part of the EM spectrum. This implies that the model for the dielectric function should be carefully chosen and/or adapted to the problem at question. To accurately describe the optical properties of the noble metals, Drude model is usually modified by introducing the term  $\delta\tilde{\epsilon}_{\text{inter}}(\omega)$ , a complex function, which involves the contributions from the inter-band transitions. One possibility is to introduce term  $\epsilon_\infty$  instead of unity in the equation 2.10 :

$$\tilde{\epsilon}(\omega) = \epsilon_\infty - \frac{\omega_p^2}{\omega^2 + i\omega\Gamma}. \quad (2.13)$$

This is the modified Drude's dielectric function for metals, with typical values of  $\epsilon_\infty$  between 1 and 10 [42]. The constants in modified Drude dielectric function are usually determined experimentally, as fitting parameters. It turns out that values

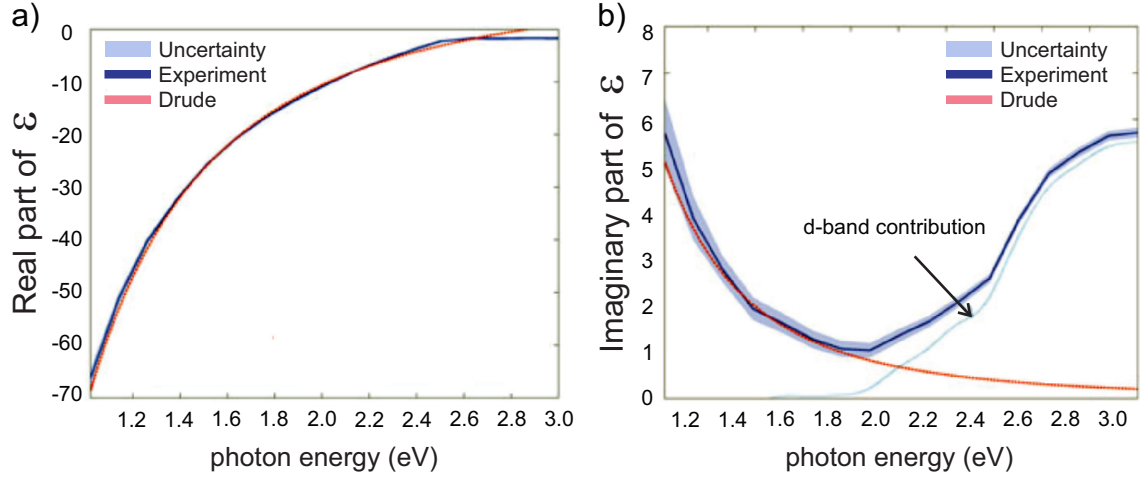


**Figure 2.5:** Comparison of real and imaginary dielectric function of gold between modified Drude model and the experimental results for  $\epsilon_\infty = 10$  and  $\Gamma_d = 0.1$  fs. The discrepancy in the imaginary part of the Drude dielectric function and experimental data is observable for the energies above 1.9 eV. Taken from Ref. [43].

vary among the studies [42, 43]. Figure 2.5 shows the comparison between the modified Drude model (Eq. 2.10) and the experimental results from the Ref [43].

There are other attempts for improving Drude model for gold, which also include the inter-band transitions [42]. For example, Derkachova *et al.* [42] added a simple term to the imaginary part of the dielectric function  $\tilde{\epsilon}_2$ :

$$\Delta\epsilon^{(\text{Au})}(\omega) = \frac{A}{1 + \exp(-(\omega - \omega_c)/\Delta)}, \quad (2.14)$$

accounting the frequency-dependent contribution of inter-band transition. Figure 2.6 shows the comparison between the experimental data with standard Drude and modified Drude dielectric functions for EM radiation in the range from 0.6 to 3 eV, with the inset showing specific contribution from the additional term for the  $\tilde{\epsilon}_2$ .

On the other hand, if the material has reduced dimensions, as in the case of nanoparticles, the size effect becomes important factor in the interactions with the external EM radiation [41]. If the MNPs diameter is of same order as electron's mean free path in the crystal ( $\approx 28, 42,$  and  $55$  nm for Cu, Ag and Au, respectively), then the electrons' collisions with the surface also influence the optical response of the MNPs. This correction can be incorporated in dielectric function of the MNPs by modifying damping factor  $\Gamma$ . If the frequency of collisions with the surface is



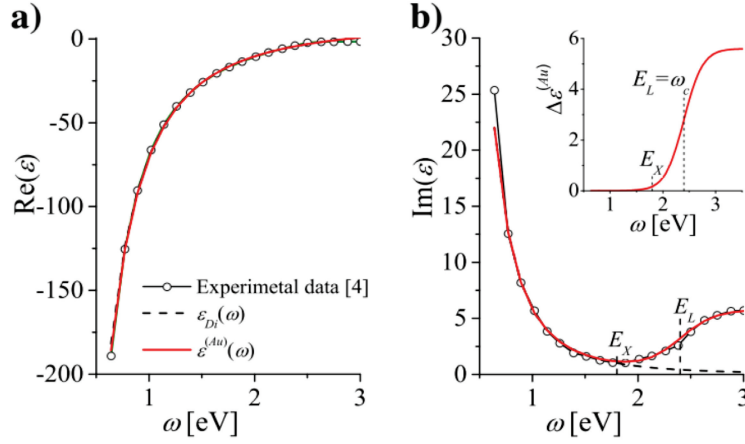


**Figure 2.6:** Comparison between the modified Drude model (black dashed line), the improved expression by Derkachova *et al.* (red solid line) and the experimental data (black line with empty circles) for the dielectric function for gold. Taken from Ref. [42].

estimated as inversely proportional to the time electron needs to cross the particle of diameter  $D$  with Fermi velocity  $v_F$ , then the total collision rate has the following form:

$$\Gamma = \Gamma_0 + g \frac{v_F}{D}, \quad (2.15)$$

where  $\Gamma_0$  is the damping factor of the bulk metal (Formula 2.6). The constant  $g$  is a proportionality factor with values between 1 and 3 (see Chapter 7 from [41]). It depends on the density of states of electrons in MNPs and the frequency of the external EM radiation but also on the surrounding medium of the MNPs. An empirical expression for damping factor in case of noble metal nanoparticles is of the order of  $\hbar g v_F / D \approx 1.3 / D \text{ eV nm}^{-1}$  [41].

Beside increasing the collision rate of electrons in metal nanoparticles, the radiation can interact with the material in another way, by exciting localized surface plasmon, which is commonly called surface plasmon resonance (SPR). The sizes of typical metal nanoparticles are usually smaller than the EM radiation wavelength, and, at the same time, comparable to the typical penetration lengths of EM radiation into the metal crystal (for example, 20 nm for Ag in the optical range). Consequently, the radiation can induce the oscillations of plasma electrons as in macroscopic crystals. These oscillations depend on the density of the free electrons, as well as of the geometry of the nanoparticle. Due to the small dimensions of

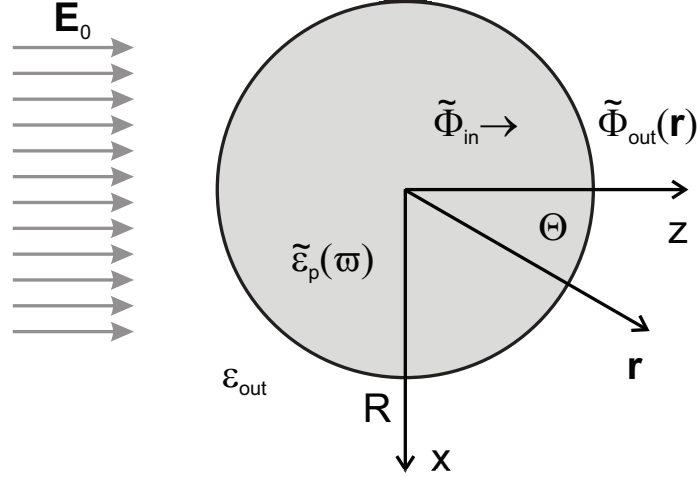


**Figure 2.7:** Schema of the metal nanoparticles of the radius  $R$  and complex dielectric function  $\tilde{\epsilon}$  that is located in the environment of the dielectric function  $\epsilon_0$ . The uniform external electromagnetic field of the amplitude  $E_0$  is oriented in  $z$  direction. The electrostatic potential in the nanoparticle is denoted as  $\Phi_{in}$  and in the surrounding as  $\Phi_{out}$ .

nanoparticles, the phase of the external EM radiation can be considered constant over the whole nanoparticle and the coupling can be generally analysed by using the quasi-static approximation [41].

The interaction of the uniform static electric field  $\mathbf{E}_0 = E_0 \mathbf{e}_z$  with spherical, isotropic, metal nanoparticle of a radius  $R$  is schematically presented in Figure 2.7. The dielectric constant of the MNP is denoted by  $\tilde{\epsilon}_p(\omega)$ , while the isotropic surrounding medium is characterized by  $\epsilon_{out}$ . In order to determine the expressions for the electric field inside and outside of the particle, the first step is to solve the Laplace equation  $\nabla^2 \tilde{\varphi}(r) = 0$  for the electrostatic potential  $\tilde{\varphi}$  in Fourier space [40]. The boundary conditions on the interface between the MNP and the medium yield the solution for  $\tilde{\varphi}(r)$ :

$$\tilde{\varphi}(r, \theta) = \sum_{l=0}^{\infty} [A_l r^l + B_l r^{-l(l+1)}] P_l(\cos \theta), \quad (2.16)$$

where  $P_l(\cos \theta)$  are the Legendre polynomials of order  $l$ , and  $\theta$  is the angle between the vector  $\mathbf{r}$  and the ort  $\mathbf{e}_z$ . The potential must be finite and therefore the potentials

inside  $\tilde{\varphi}_{in}$  and outside  $\tilde{\varphi}_{out}$  have the forms:

$$\tilde{\varphi}_{in}(r, \theta) = \sum_{l=0}^{\infty} A_l r^l P_l(\cos \theta), \quad (2.17)$$

$$\tilde{\varphi}_{out}(r, \theta) = \sum_{l=0}^{\infty} [B_l r^l + C_l r^{-l(l+1)}] P_l(\cos \theta). \quad (2.18)$$

Coefficients in these formulae can be determined by the boundary conditions (for  $r \rightarrow \infty$  and for  $r = R$ ), and the final expressions are ([40]):

$$\tilde{\varphi}_{in}(r, \theta) = -\frac{3\epsilon_{out}}{\tilde{\epsilon}_p(\omega) + 2\epsilon_{out}} E_0 r \cos(\theta), \quad (2.19)$$

$$\tilde{\varphi}_{out}(r, \theta) = -E_0 r \cos(\theta) + R^3 \frac{\tilde{\epsilon}_p(\omega) - \epsilon_{out}}{\tilde{\epsilon}_p(\omega) + 2\epsilon_{out}} E_0 \frac{\cos(\theta)}{r^2}. \quad (2.20)$$

The expression for  $\tilde{\varphi}_{out}$  has a form of a superimposed external field and an electric dipole moment located in the nanosphere. So by introducing it in the form of

$$\boldsymbol{\mu}_{sph} = \epsilon_{out} R^3 \frac{\tilde{\epsilon}_p(\omega) - \epsilon_{out}}{\tilde{\epsilon}_p(\omega) + 2\epsilon_{out}} \mathbf{E}_0, \quad (2.21)$$

the expression  $\tilde{\varphi}_{out}$  becomes of somewhat simplified form

$$\tilde{\varphi}_{out}(\mathbf{r}) = -\mathbf{E}_0 r + \frac{1}{\epsilon_{out}} \frac{\tilde{\boldsymbol{\mu}}_{sph} \cdot \mathbf{r}}{r^3}. \quad (2.22)$$

This means that the problem can be treated like the external electromagnetic field induces a dipole moment inside the nanoparticle. By defining an effective polarizability of the sphere  $\alpha_{sph}$  by  $\tilde{\boldsymbol{\mu}}_{sph} = \epsilon_{out} \alpha_{sph}(\omega) \mathbf{E}_0$ , as an approximation for a field that is uniform in the nanoparticle, the expression for  $\tilde{\alpha}_{sph}$  becomes:

$$\tilde{\alpha}_{sph} = R^3 \frac{\tilde{\epsilon}_p(\omega) - \epsilon_{out}}{\tilde{\epsilon}_p(\omega) + 2\epsilon_{out}}. \quad (2.23)$$

By calculating negative gradient of  $\tilde{\varphi}_{in}$  and  $\tilde{\varphi}_{out}$ , it is possible to obtain the expres-

sions for the electric field as:

$$\begin{aligned}\tilde{\mathbf{E}}_{in} &= \frac{3\epsilon_{out}}{\tilde{\epsilon}_p(\omega) + 2\epsilon_{out}} \mathbf{E}_0, \\ \tilde{\mathbf{E}}_{out} &= \mathbf{E}_0 + \frac{1}{\epsilon_{out}} \frac{3\mathbf{r}(\mathbf{r} \cdot \tilde{\boldsymbol{\mu}}_{sph}) - \tilde{\boldsymbol{\mu}}_{sph}}{r^3}.\end{aligned}\quad (2.24)$$

The later expressions qualitatively describe the changes in the electric field in the vicinity of MNPs due to the appearance of the dipole moment inside the nanoparticles. Depending on the dielectric functions of the metal and the surrounding medium, the electrical field near the NP can be enhanced or reduced. By setting the dielectric constant of the medium  $\epsilon_{out}$  to  $-\epsilon_p(\omega)/2$ , the effective polarizability  $\alpha_{sph}$  can have a resonant enhancement, which will manifest as a SPR maximum. The MNPs' mode that satisfies this so-called Frohlich condition is named the dipole localized surface plasmon. It implies that the real part of the nanoparticles has to be negative, which is usually obtained for metals. Therefore, by choosing appropriate medium, type of nanosphere material and the frequency of the external EM field, large field magnifications at the surface of the MNPs can appear. Also, the equations 2.24 also describe the influence of the medium on the surface plasma frequency of the MNPs. By increasing the dielectric constant of the medium, the SPR position red-shifts. This allows experimental detection of small changes in the medium by following the optical properties of metal nanoparticles. It is worth noting that in the expression for the dielectric function, there is no direct relation to the size of the MNPs. That implies that as long as the dielectric function does not change in particular size ranges, the SPR peak will have the same frequency. This is experimentally validated for the nanoparticles with intermediate sizes, from 5 to 30 nm [41].

Starting with the expression for the dielectric function of the metal of the nanoparticles, the SPR frequency can be derived as a function of the plasma frequency of the metal. In the case of ideal, free, lossless electron gas, from the Drude ideal free gas dielectric function (Eq. 2.10), the expression for SPR frequency as  $\omega_{SPR} = \frac{\omega_p}{\sqrt{1+2\epsilon_{out}}}$  was obtained. For the MNP in vacuum, the later expression takes the well-known form  $\omega_{SPR} = \frac{\omega_p}{\sqrt{3}}$ .

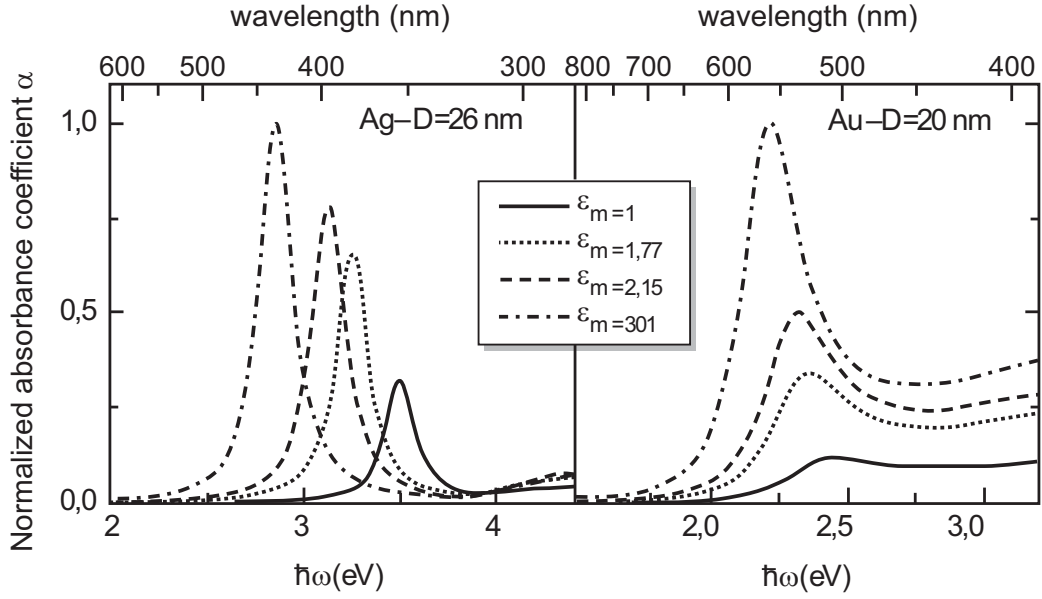


**Figure 2.8:** Calculated absorption spectra for silver and gold nanoparticles in quasi-static approximation. The diameter of the nanoparticles is denoted in upper right corner of the graphs. The dielectric constants of the nanoparticles' environment are given in the legend. Taken from Chapter 7 in the Ref. [41]

Therefore, the optical response of noble metal nanoparticles will highly depend on several crucial parameters of the system, making them accessible in experimental measurements. The absorbance measurements are most commonly used to investigate of the optical properties of the colloidal nanoparticles. Assuming that the volume of all nanoparticles is negligible compared to the volume of the colloid ( $p = \frac{N_{NP}V_{NP}}{V} \ll 1$ ), the absorbance coefficient can be written as following [41]:

$$\alpha(\omega) = \frac{\omega}{c\epsilon_{out}^{1/2}} p \left| \frac{3\epsilon_{out}}{\epsilon_p + 2\epsilon_{out}} \right|^2 \epsilon_2(\omega) \quad (2.25)$$

Therefore, in the optical part of the spectrum, the absorption of MNPs depends on the surface plasmon resonance and inter-band transitions. In the case of gold nanoparticles, the inter-band absorbance is closer to the SPR peak, which results in losing its quasi-Lorentzian shape.

The solution of the Laplace equation for electrostatic potential  $\tilde{\varphi}$  qualitatively explains the main characteristics of the behaviour of metal nanoparticles. However, by solving the Maxwell equations for a spherical metal object of nanometre size ( $< 100\text{nm}$ ) in a dielectric medium, it is possible to describe the absorption and

scattering properties of such material [41]. This has been done within the Mie theory, which will be shortly presented here by using the excellent approach taken from the reference [44].

First, we will start with the well-known fact that the plane electromagnetic field can be represented as an infinite series of spherical Bessel functions. For an electromagnetic wave to be physically realizable, it is necessary for its  $\mathbf{E}$  and  $\mathbf{H}$  vectors to satisfy the vector wave equations. They must also be divergence free and mutually dependent. It turns out that it is possible to find simple time-harmonic fields in a linear, isotropic, homogeneous medium, which will satisfy the field equations at the same time. Both  $\mathbf{E}$  and  $\mathbf{H}$  can be constructed with a single scalar function that satisfies the scalar wave equation, and an arbitrary vector. Due to the symmetry of the problem, the radial vector from coordinate origin can be chosen as an arbitrary vector. The solution of a scalar wave equation in spherical polar coordinates is separable into three functions. Each function is a solution to a separate wave equation for the corresponding coordinate,  $r$ ,  $\theta$  or  $\phi$ . Additional two separation constants ( $m$ ,  $n$ ) appear that are used to fulfill the subsidiary conditions that will allow  $\mathbf{E}$  and  $\mathbf{H}$  to be physically possible. The azimuthal function of the solution has to be single valued with a period of  $2\pi$ , leading toward either  $\cos\theta(m\phi)$  or  $\sin\theta(m\phi)$ . The polar angle function has to also satisfy an additional condition: to be finite valued functions in points  $\theta = 0$  and  $\theta = \pi$ . The solution to this equation is given by the orthogonal associated Legendre functions of the first kind  $P_n^m(\cos\theta)$  of degree  $n$  and order  $m$ , where  $n = m, m + 1, m + 2, \dots$ . In the case  $m = 0$ , these functions become Legendre polynomials, which were already mentioned in the text. The radial equation can be solved by substituting the coordinate  $r$  with the dimensionless variable  $\rho = kr$ , for which solutions are linearly independent Bessel functions of first and second kind  $J_{n+1/2}(\rho)$  and  $Y_{n+1/2}(\rho)$ . Therefore, for the initial radial wave equation the solutions are spherical Bessel functions given by  $j_n = \sqrt{\frac{\pi}{2\rho}} J_{n+1/2}(\rho)$  and  $y_n = \sqrt{\frac{\pi}{2\rho}} Y_{n+1/2}(\rho)$ . These two functions are independent solutions, so therefore any linearly independent combination of these two would also represent a solution to the radial equation. Such example are Hankel functions, or spherical Bessel functions of third kind, given by:

$$h_n^{(1)}(\rho) = \sqrt{\frac{\pi}{2\rho}} J_{n+1/2}(\rho) + i\sqrt{\frac{\pi}{2\rho}} Y_{n+1/2}(\rho) \quad (2.26)$$

$$h_n^{(2)}(\rho) = \sqrt{\frac{\pi}{2\rho}} J_{n+1/2}(\rho) - i\sqrt{\frac{\pi}{2\rho}} Y_{n+1/2}(\rho) \quad (2.27)$$

Although they are general solutions, the chosen Bessel function will behave well, both in the critical points of the differential equation and in the asymptotic region  $\rho \rightarrow \infty$ . For example,  $h_n^{(1)}$  behaves as an outgoing spherical wave, while  $h_n^{(2)}$  as an incoming. Finally, the full solution to the scalar function that satisfies the scalar wave equation is

$$\psi_{emn} = \cos(m\phi) P_n^m(\cos\theta) z_n(kr), \quad (2.28)$$

$$\psi_{omn} = \sin(m\phi) P_n^m(\cos\theta) z_n(kr). \quad (2.29)$$

where  $e$  and  $o$  stand for even and odd, and  $z_n$  represents one of the mentioned spherical Bessel functions, or their linearly independent combination. Due to the completeness of these functions one by one, any function that satisfies scalar wave equation can be expanded as an infinite series of the  $\psi_{emn}$  and  $\psi_{omn}$ . Finally, the vector spherical harmonics generated with these scalar functions are:

$$M_{e/omn} = \nabla \times (\mathbf{r}\psi_{e/omn}) \quad (2.30)$$

and

$$N_{e/omn} = \frac{\nabla \times M_{e/omn}}{k}. \quad (2.31)$$

As an example how the spherical harmonics can be used to represent a plane wave polarized in  $x$  plane, given in spherical coordinates

$$\mathbf{E} = E_0 e^{ikr \cos\theta} (\sin\theta \cos\phi \mathbf{e}_r + \cos\theta \cos\phi \mathbf{e}_\theta - \sin\phi \mathbf{e}_\phi). \quad (2.32)$$

The expansion in the vector spherical harmonics would look like:

$$\mathbf{E} = \sum_{m=0}^{\infty} \sum_{n=0}^{\infty} (B_{emn} \mathbf{M}_{emn} + B_{omn} \mathbf{M}_{omn} + A_{emn} \mathbf{N}_{emn} + A_{omn} \mathbf{N}_{omn}). \quad (2.33)$$

Due to the orthogonality of the vector functions  $\mathbf{M}$  and  $\mathbf{N}$  for the equal coefficients, as well as the fact that sine and cosine for the same  $m$  are orthogonal, the coefficients  $A$  and  $B$  are determined by the following (similarly for all combinations):

$$B_{emn} = \frac{\int_0^{2\pi} \int_0^{\pi} \mathbf{E} \cdot \mathbf{M}_{emn} \sin \theta d\theta d\phi}{\int_0^{2\pi} \int_0^{\pi} |\mathbf{M}_{emn}|^2 \sin \theta d\theta d\phi}. \quad (2.34)$$

Further analysis of orthogonal coefficients, integrals and relation for Legendre functions, the final expressions for nonzero coefficients  $A$  and  $B$  are

$$B_{o1n} = i^n E_0 \frac{2n+1}{n(n+1)} \quad (2.35)$$

and

$$A_{e1n} = -i E_0 i^n \frac{2n+1}{n(n+1)} \quad (2.36)$$

Finally, the plane wave polarized in  $x$  direction can be expressed like

$$\mathbf{E}_i = E_0 \sum_{n=1}^{\infty} i^n \frac{2n+1}{n(n+1)} (\mathbf{M}_{o1n} - i \mathbf{N}_{e1n}), \quad (2.37)$$

where the spherical Bessel function of first kind was used. The magnetic vector field can be calculated by applying curl operator on  $\mathbf{E}$ , e.g.

$$\mathbf{H}_i = \frac{-k}{\omega\mu} E_0 \sum_{n=1}^{\infty} i^n \frac{2n+1}{n(n+1)} (\mathbf{M}_{e1n} + i \mathbf{N}_{o1n}). \quad (2.38)$$

Obtained expressions for plane wave as a series of vector spherical harmonics can be used for analysis of the internal ( $\mathbf{E}_1, \mathbf{H}_1$ ) and scattered ( $\mathbf{E}_s, \mathbf{H}_s$ ) fields of a spherical particle in a medium exposed to external electromagnetic polarized radiation ( $\mathbf{E}_i, \mathbf{H}_i$ ). The boundary condition implies that:

$$(\mathbf{E}_i + \mathbf{E}_s - \mathbf{E}_1) \times \mathbf{e}_r = (\mathbf{H}_i + \mathbf{H}_s - \mathbf{H}_1) \times \mathbf{e}_r = 0 \quad (2.39)$$



The incoming radiation ( $\mathbf{E}_i, \mathbf{H}_i$ ) can be taken from already derived expression. As for the fields inside the sphere, they have to be finite, so the appropriate Bessel function is of first kind. So the initial expressions for the internal fields ( $\mathbf{E}_1, \mathbf{H}_1$ ) are

$$E_1 = \sum_{n=1}^{\infty} E_n (c_n M_{o1n}^{(1)} - i d_n N_{e1n}^{(1)}). \quad (2.40)$$

$$H_1 = \frac{-k_1}{\omega \mu_1} \sum_{n=1}^{\infty} E_n (d_n M_{e1n}^{(1)} + i c_n N_{e1n}^{(1)}), \quad (2.41)$$

where  $E_n = i^n E_0 \frac{2n+1}{n(n+1)}$ , and the superscripts are referring to the spherical Bessel function of the first kind. Permeability of the sphere and wavevector of the radiation inside the sphere are  $\mu_1$  and  $\mathbf{k}_1$ . As for the outside the sphere is concerned, both spherical Bessel functions of first and second kind are well behaved, so both should be taken into the equations. However, due to the asymptotic behaviour of the field, it is also possible to employ one of the Hankel functions, the one describing the outgoing spherical wave,  $h_n^{(1)}$ . Therefore, the initial expressions for the scattered field are

$$E_s = \sum_{n=1}^{\infty} E_n (i a_n N_{e1n}^{(3)} - b_n M_{o1n}^{(3)}), \quad (2.42)$$

$$H_s = \frac{k}{\omega \mu} \sum_{n=1}^{\infty} E_n (i b_n N_{o1n}^{(3)} + a_n M_{e1n}^{(3)}), \quad (2.43)$$

where the superscript (3) implies using Henkel function. The unknown four coefficients are defined by the boundary condition at the sphere surface. By using the orthogonality and properties of the vector harmonics, the coefficients are given by

$$a_n = \frac{\mu m^2 j_n(mx) [x j_n(x)]' - \mu_1 j_n(x) [m x j_n(mx)]'}{\mu m^2 j_n(mx) [x h_n^{(1)}(x)]' - \mu_1 h_n^{(1)}(x) [m x j_n(mx)]'}, \quad (2.44a)$$

$$b_n = \frac{\mu_1 j_n(mx) [x j_n(x)]' - \mu j_n(x) [m x j_n(mx)]'}{\mu_1 j_n(mx) [x h_n^{(1)}(x)]' - \mu h_n^{(1)}(x) [m x j_n(mx)]'}, \quad (2.44b)$$

$$c_n = \frac{\mu_1 j_n(x) [x h_n^{(1)}(x)]' - \mu_1 h_n^{(1)}(x) [x j_n(x)]'}{\mu_1 j_n(mx) [x h_n^{(1)}(x)]' - \mu h_n^{(1)}(x) [m x j_n(mx)]'}, \quad (2.44c)$$

$$d_n = \frac{\mu_1 m j_n(x) [x h_n^{(1)}(x)]' - \mu_1 m h_n^{(1)}(x) [x j_n(x)]'}{\mu m^2 j_n(mx) [x h_n^{(1)}(x)]' - \mu_1 h_n^{(1)}(x) [m x j_n(mx)]'}, \quad (2.44d)$$

where  $x$  is size parameter defined by  $x = k/R$ , where  $R$  is the radius of the sphere, and  $m$  is the ratio of the refractive indexes inside and outside the sphere, and the differentiation is with respect to the argument in parentheses. By introducing Riccati-Bessel functions by  $\psi_n(\rho) = \rho j_n(\rho)$  and  $\xi_n(\rho) = \rho h_n^{(1)}(\rho)$ , and assuming that the permeability of the sphere and the medium is the same, slightly simplified expressions are gained for the scattering coefficients:

$$a_n = \frac{m\psi_n(mx)\psi'_n(x) - \psi_n(x)\psi'_n(mx)}{m\psi_n(mx)\xi'_n(x) - \xi_n(x)\psi'_n(mx)}, \quad (2.45a)$$

$$b_n = \frac{\psi_n(mx)\psi'_n(x) - m\psi_n(x)\psi'_n(mx)}{\psi_n(mx)\xi'_n(x) - m\xi_n(x)\psi'_n(mx)}, \quad (2.45b)$$

$$c_n = \frac{m\psi_n(x)\xi'_n(x) - m\xi_n(x)\psi'_n(x)}{\psi_n(mx)\xi'_n(x) - m\xi_n(x)\psi'_n(mx)}, \quad (2.45c)$$

$$d_n = \frac{m\psi_n(x)\xi'_n(x) - m\xi_n(x)\psi'_n(x)}{m\psi_n(mx)\xi'_n(x) - \xi_n(x)\psi'_n(mx)}. \quad (2.45d)$$

Last part includes finding the expression for the scattering and absorption cross sections, for which it is necessary to introduce Poynting vector. Poynting vector is determined by the magnitude and direction of the rate of EM energy transfer through a surface in space. When the electromagnetic wave can have complex values, i.e. in the case of time harmonics, the Poynting vector is defined as a cross product of real parts of electric and magnetic fields  $S_t = \text{Re}[\mathbf{E}] \times \text{Re}[\mathbf{H}]$ , while a time-averaged Poynting vector is  $S = \frac{1}{2}\text{Re}[\mathbf{E} \times \mathbf{H}]$ . At any point of space, there are three quantities that contribute to time-averaged Poynting vector, the incident EM field ( $\mathbf{E}_i$ ), the scattered EM field ( $\mathbf{E}_s$ ), and additional one that might come from the interaction between the incident beam and scattered waves ( $\mathbf{E}_{ext}$ ). So the Poynting vector outside the sphere ( $\mathbf{S}$ ), which is defined by the cross product of  $\mathbf{E}_2$  and  $\mathbf{H}_2$ , is the sum of mentioned three Poynting vectors  $\mathbf{S}_i$ ,  $\mathbf{S}_s$  and  $\mathbf{S}_{ext}$ .

By using the Poynting vector, a net rate of the electromagnetic energy "crossing" a closed surface  $A$ , with a specified outward unit normal vector  $n$ , which enclose a volume  $V$ , is defined by

$$W = - \int_A \mathbf{S} \cdot \hat{n} dA. \quad (2.46)$$

If the net rate  $W$  has positive value, the EM energy is being absorbed by the nanoparticle volume. That implies that the net rate through the surface surrounding the sphere has to be positive (a negative value would mean that the sphere is radiating), and that  $W_i$ , for the incident field, is zero due to the non-absorbing nature of the chosen medium. If the  $A$  is centered around the sphere, the net rate outside the sphere  $W_a$  is then given by just two terms

$$W_a = -W_s + W_{ext} = - \int_A \mathbf{S}_s \mathbf{e}_r dA - \int_A \mathbf{S}_{ext} \mathbf{e}_r dA, \quad (2.47)$$

where the sign of  $W_s$  is chosen for convenience. Therefore, it can be written that  $W_s = W_a + W_{ext}$ . After substituting expressions for Poynting vectors, and taking into account the series of the EM fields with wave vector harmonics, the expression for scattered net rate becomes

$$W_s = \frac{\pi |E_0|^2}{k\omega\mu} \sum_{n=1}^{\infty} (2n+1) \text{Re}[g_n] (|a_n|^2 + |b_n|^2), \quad (2.48)$$

where  $g_n = -\xi_n \xi_n'$ . Finally, cross sections are defined as the ratio between the net rate of EM energy and the incidence irradiance, therefore the expressions for scattering cross section and analogously derived extinction cross section are

$$C_{sca} = \frac{W_{sca}}{I_i} = \frac{2\pi}{k^2} \sum_{n=1}^{\infty} (2n+1) (|a_n|^2 + |b_n|^2), \quad (2.49)$$

$$C_{ext} = \frac{W_{ext}}{I_i} = \frac{2\pi}{k^2} \sum_{n=1}^{\infty} (2n+1) \text{Re}[a_n + b_n]. \quad (2.50)$$

Cross section of the absorbing wave is calculated by subtracting extinction cross sections from cross section of scattered light. Once the cross sections are obtained, it is simple to calculate the efficiency factors for absorption ( $Q_a$ ), scattering ( $Q_s$ ) and extinction ( $Q_{ext}$ ), as a ratio of the corresponding cross sections and projected cross-sectional area of the object ( $G$ ). In case of the sphere, it would be  $G = \pi R^2$ .

In the case when the sphere is small in comparison with the wavelength of the incident radiation, the lowest order of the Bessel functions, e.g. with lowest values of  $n$ , influence the most cross sections. Very often it is enough to take first few

terms in the series to have very good reproduction of the experimental data. The optical properties of nanoparticles are dependent on their composition, shape, size, and external radiation, but also on the surrounding medium. The later property attracted attention due to its applicability. The sensitivity of the metal nanoparticles to the changes in surrounding medium was illustrated by Dondapati *et al.* [13]. The authors analysed gold nanostars with biotin molecules attached to their surfaces and were able to detect additional molecule streptavidin in the solution from 0.1 nM concentration. The attachment of streptavidin to biotin moieties changed the dielectric surrounding of the nanostars, which consequently red-shifted its surface plasmon resonance. The authors also showed that the higher order surface plasmon resonances are more sensitive to the medium changes. Also, McFarland *et al.* [12] were able to detect the adsorption of fewer than sixty thousand of 1-hexadecanethiol molecules on the single silver nanoparticle by a shift of 40 nm of the surface plasmon resonance. They argued that the detection limit for SPR sensing is well below one thousand for small molecules, and even lower for large molecules as for example antibodies and proteins.

## 2.2 Interaction of noble metal nanoparticles and fluorophores

As it was shown in the previous subsection, metal nanoparticles effectively change the distribution of the applied electromagnetic field in the surrounding medium, both locally and non-locally. These local changes in the field distribution can also influence properties of other objects, i.e. molecules, submerged in the same medium. The simplest case is when the metal nanoparticles and molecules are attached to one another, for example, in which different chemical and physical effects can occur. In such close interaction between molecules and nanoparticles, chemical effects might include charge transfer between the molecules and the surface of the NPs, orbital mixing of the constituents, creation of chemical bonds etc. As for differences in physical properties, the main interaction is mediated through the changes in the electromagnetic field, both by nanoparticles and molecules. Surface-enhanced prop-

erties of molecules in vicinity of MNPs can be observed in changes in molecules absorbance spectra, vibrational absorption, vibrational Raman scattering, second harmonic generation and sum frequency generation, two-photon absorption and chiro-optical properties [40].

Strongly pronounced effects are also observed when fluorescing molecules, called fluorophores, are in the vicinity of noble metal nanoparticles. By enhancing the EM field, MNPs increase the excitation rates of fluorophores, which are proportional to the local electric field intensities [45]. Nanoparticles also influence both radiative and nonradiative decaying rates of the fluorophores in their vicinity. Depending on the problem at question, the metal nanoparticles can be taken as a continuous body characterized by the frequency-dependent dielectric function, while the molecule can be treated either as a discrete dipole or atomistically. The description of the electromagnetic interactions in a MNP-molecule system can employ either classical or quantum electrodynamics. Classical electrodynamics is usually used for small nanoparticles of dimensions close to one tenth of the external radiation wavelength, in which case the quasi-static approximation can be assumed. Its applicability is proved by the fact that it can explain fair number of phenomena arising from the nanoobjects in the medium rich with fluorescent molecules. As long as the coupled system is of smaller dimension than the wavelength of the external radiation, the retardation effects can be neglected [40, 46, 47].

In the vicinity of metal nanoparticles, there are additional paths for deexcitation of fluorescent molecules, which are treated as radiating dipoles. The molecule emits EM radiation, which partially penetrates the metal nanoparticle and becomes dissipated in it. Additionally, the emitted radiation can couple to the plasmon modes of MNPs and, therefore, the emission in far-field regime can change. Gersten *et al.* [46] used both semiclassical steady-state approach and time-dependent approach to deduce the decay rates of a molecule, seen as a point dipole, in the close proximity of a metal nanospheroid. In the time-dependent approach, they quantized metal nanoparticle's plasmons, and constructed a Hamiltonian for calculation of approximate equations of motion of the molecule-plasmon system in the incident radiation field.

The Hamiltonian of the system was separated in five terms: a Hamiltonian describing the plasmon behaviour  $-H_s$ , the interaction of the nanoparticle and incident radiation  $-H_{sE}$ , the interaction of NP and the molecule  $-H_{sd}$ , a Hamiltonian of the molecule approximated as a dipole  $-H_d$ , and the interaction of the dipole with the incident radiation  $-H_{dE}$ . The quantization of the plasmons of the nanoparticle is done by considering the nanoparticle as an ideal particle whose plasmon resonances are associated with an independent harmonic plasmon mode  $b_{lm}$  (with its  $l$ -th mode resonance frequency  $\omega_l$  and damping rates of Drude type  $\gamma_l$ ). The Hamiltonian describing the plasmon behaviour was expressed as  $H_s = \sum_{l=0}^{\infty} \sum_{m=-l}^{m=l} \hbar\omega_l b_{lm} b_{lm}$ . The interaction of the nanoparticle with the incident radiation, which is taken to be homogeneous sphere, is given by  $H_s = -\mu_s \cdot E$ , assuming the dipole moment of the dielectric sphere  $\mu_s$ . The Hamiltonian describing the interaction of the NP and the dipole, located above the sphere at the  $z$  direction at a distance  $a$  is of similar form as the previous  $H_{sd} = -\mu \cdot E_s = \mu \cdot \nabla\phi_s$ . As for the Hamiltonian of the molecule, it is of standard form for an oscillating dipole  $H_d = \frac{m}{2}[\dot{\rho}] + V(\rho)$ , where the intramolecular coordinates are denoted with  $\rho$ . The last term of the Hamiltonian that describes the interaction of the dipole with external radiation again has the form  $H_{dE} = -\mu(\rho) \cdot E$ . The final equations for the coupled motion of the plasmons modes and the dipole are used to obtain the dipole polarizability of the sphere in Drude approximation for the sphere's dipolar plasmon, which is consistent with the steady state approach the authors used. The authors also derive an expression for "an apparent quantum yield" of the molecule in proximity of nanosphere. The apparent yield is the molecule's emission that is measured in experiments, as it is not divided by the absorbed energy of the system. If the frequency of the incident radiation is denoted by  $\omega_0$ , and the molecular absorbance and emission frequency by  $\omega_a$  and  $\omega_b$ , respectively, the dipole moment induced by the molecule positioned in the  $z$  direction above the sphere is

$$\mu = \frac{\alpha E_{loc}}{\omega_a^2 - \omega_0^2 - i\omega_0\Gamma}, \quad (2.51)$$

where  $E_{loc}$  is the amplitude of the  $z$  component of the local electric field. In approximation that the molecule's image field is negligible, the  $E_{loc}$  is given by

$$E_{loc} = \left[1 + 2 \frac{\epsilon(\omega_0) - 1}{\epsilon(\omega_0) + 2} \left(\frac{R}{a}\right)^3\right] E_{inc}. \quad (2.52)$$

Upon absorption of the EM radiation, the dipole reemits light of frequency  $\omega_b$ , and the total dipole moment of the molecule becomes:

$$\mu^{tot} = \left[1 + 2 \frac{\epsilon(\omega_b) - 1}{\epsilon(\omega_b) + 2} \left(\frac{R}{a}\right)^3\right] \mu. \quad (2.53)$$

The emission intensity, or the apparent quantum yield  $Y_{app}$ , is proportional to the total dipole moment:

$$\Upsilon_{app} = \left|1 + 2 \frac{\epsilon(\omega_b) - 1}{\epsilon(\omega_b) + 2} \left(\frac{R}{a}\right)^3\right|^2 \times \left|1 + 2 \frac{\epsilon(\omega_a) - 1}{\epsilon(\omega_a) + 2} \left(\frac{R}{a}\right)^3\right|^2 \times \frac{(\omega_a^2 - \omega_0^2)^2 + \omega_0^2 \Gamma^{(f)2}}{(\omega_a^2 - \omega_0^2)^2 + \omega_0^2 \Gamma^2}, \quad (2.54)$$

and in the case of monitoring at the emission wavelength,  $\omega_0$  should be changed with  $\omega_a$ , yielding

$$\Upsilon_{app} = \left|1 + 2 \frac{\epsilon(\omega_b) - 1}{\epsilon(\omega_b) + 2} \left(\frac{R}{a}\right)^3\right|^2 \times \left|1 + 2 \frac{\epsilon(\omega_a) - 1}{\epsilon(\omega_a) + 2} \left(\frac{R}{a}\right)^3\right|^2 \left(\frac{\Upsilon^{(f)}}{\Upsilon}\right)^2. \quad (2.55)$$

This expression is normalized to the quantum yield of the free molecule.

Figure 2.9(a) shows the apparent and real quantum yields (normalized on the QY of the free molecule, curves A and B respectively) calculated for different diameters of a nanosphere [46]. The molecule is on a fixed distance, 1.6 nm above a silver particle, and the quantum yield of the free molecule is taken to be 0.005. The authors noted that it is expected that this "small sphere" theory breaks down when the radius of the nanoparticle is more than 25 nm, since for such systems the theory overestimates the yields. It can be seen that for small particles, the yields can be less than 1. The dependence of the yield ratios on the distance of the molecule from the nanoparticle is shown in Figure 2.9(b). The radius of the silver sphere is 20 nm, and the calculated curves are for two values of the yield of the free molecule- ideal case when the yield is 1 (curves A (ratio of real yields) and B (ratios of apparent yields)), and when it is 0.005 (curves C and D). As it can be seen from the figure, the quantum yield of the free molecule also influences the effect of the nanoparticles to the fluorescence process.

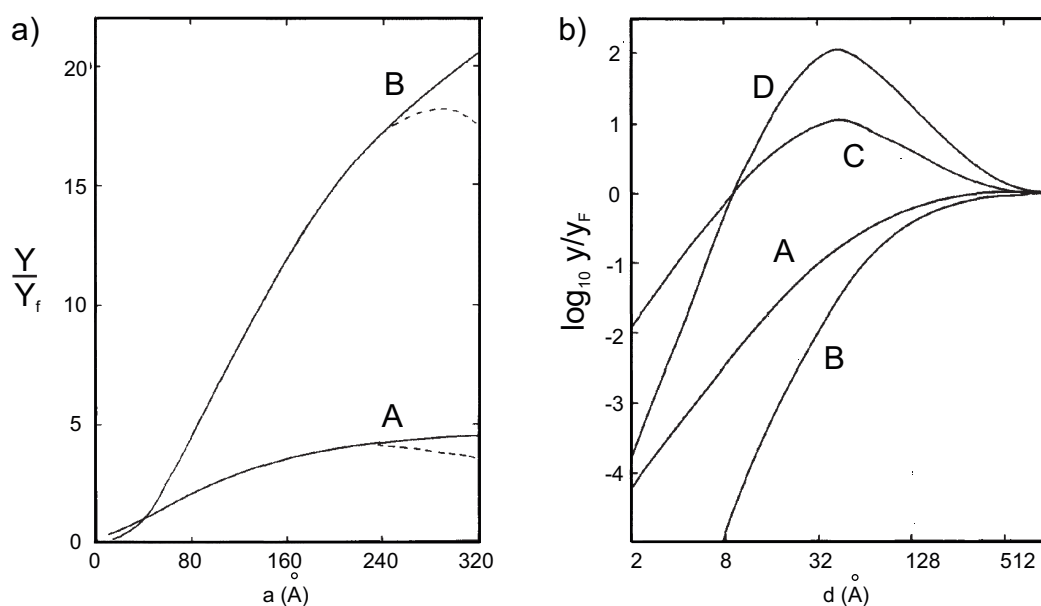


**Figure 2.9:** (a) The ratio of the real fluorescence yield to the free molecule yield (curve A) and the ratio of the apparent fluorescence yield and the free molecule yield (curve B) as a dependence on the nanoparticle's radius  $a$ . The molecule - nanoparticle distance is 1.6 nm. The dashed ending of the curve A is large sphere - approximation. Taken from Ref. [46]. (b) The ratios as in the plot (a) but plotted as a dependence on the molecule-nanoparticle distance for the nanoparticle radius of 20 nm. The curves A and B are for the quantum yield of the free molecule of the value 1, while the curves C and D are for low emitting fluorophores, i.e. for the quantum yield of the free molecule of 0.005. Taken from Ref. [46]



Another quantity that can be analysed is the rate of energy dissipation  $W$  of a fluorescing molecule in proximity of a metal nanoparticle. Ruppin used classical electromagnetic theory and by using Mie coefficients derived expressions for radiative and non-radiative rates of energy dissipation of the molecule [47], a quantities that are related to fluorescence lifetimes of a molecule, which was considered as an emitting dipole. Radiative decay rate was calculated by evaluating the Pointing vector at large distances, while the non-radiative rate was treated as Ohmic losses due to the sphere. The rates were calculated for orthogonal ( $\perp$ ) and parallel ( $\parallel$ ) orientations of the dipole, located at  $r'$ , with respect to the sphere's surface of radius  $R$ . The final expressions for radiative rates are

$$W_R^\perp = W_{R0} \frac{3}{2} \sum_{n=1}^{\infty} (2n+1)n(n+1) \frac{1}{(kr')^2} |j_n(kr') + b_n^m h_n(kr')|^2, \quad (2.56)$$

$$W_R^\parallel = W_{R0} \frac{3}{4} \sum_{n=1}^{\infty} (2n+1) \times \left[ \|j_n(kr') + a_n^m h_n(kr')\|^2 + \left| \frac{1}{kr'} [kr' j_n(kr')] + \frac{1}{kr'} [kr' h_n(kr')] b_n^m \right|^2 \right] \quad (2.57)$$

where  $W_R$  is the rate of radiative energy loss in the absence of the sphere,  $W_{R0} = \frac{\omega^4}{12\pi} \mu_0 \sqrt{\epsilon_0 \mu_0} |\mu|^2$ ,  $k = \mu \sqrt{\epsilon_0 \mu_0}$ , is the wavevector,  $\mu$  is the dipole moment of the molecule,  $j_n(x)$  and  $h_n(x)$  are spherical Bessel and Hankel functions, respectively, and  $a_n$  and  $b_n$  are Mie coefficients. As for the energy dissipation due to the presence of the sphere, the rates for non-radiative loss are given as:

$$W_A^\perp = W_{R0} \frac{3}{2} \sqrt{\frac{\mu_0}{\epsilon_0}} \sigma \sum_{n=1}^{\infty} \left[ n(n+1) \times \frac{|\beta_n h_n(kr')|^2}{r'^2} \times \int_0^R [(n+1)|j_{n-1}(k_1 r)|^2 + n|j_{n+1}(k_1 r)|^2] r^2 dr \right], \quad (2.58)$$

$$W_A^{\parallel} = W_{R0} \frac{3}{4} \sqrt{\frac{\mu_0}{\epsilon_0}} \sigma k^2 \sum_{n=1}^{\infty} (2n+1) \times \left[ |\alpha_n h_n(kr')|^2 \times \int_0^R |j_n(k_1 r)|^2 r^2 dr \right. \\ \left. + \left| \frac{\beta_n}{kr'} [kr' h_n(kr')] \right|^2 \frac{1}{2n+1} \times \int_0^R [(n+1)|j_{n-1}(k_1 r)|^2 + n|j_{n+1}(k_1 r)|^2] r^2 dr \right]. \quad (2.59)$$

The wavevector  $k_1$  is given by  $k_1 = \omega \sqrt{\epsilon(\omega) \epsilon_0 \mu_0}$  and represents the wavevector inside the sphere, while  $\sigma(\omega)$  stands for the sphere's conductivity and is equal to  $\sigma(\omega) = \omega \epsilon''(\omega) \epsilon_0$ . The coefficients  $\alpha$  and  $\beta$  are the coefficient determined by the boundary conditions at the NP surface for electromagnetic field and represent the EM field from the molecule's emission that penetrates the metal sphere.

Using these expressions for the energy rate it is possible to calculate the lifetime of the molecular states from the sum of the radiative and non-radiative rates, by inverting normalized total rate with the rate for the molecule in free space. The dependence of the lifetime of a molecule in the excited state in perpendicular and orthogonal orientation respectively on the distance  $\hat{d}$  (where  $\hat{d} = kd$ ) are shown in Figure 2.10(a) and (b), respectively [47]. The lifetime in proximity of a silver nanoparticle of radius 10 nm is compared to the lifetime obtained in the case when the molecule is above a metal surface, for the emission wavelength 612 nm. The deviation in the behaviour is not negligible. The author suggests that observed difference is due to the emission interference from the surface that is responsible for the oscillatory lifetime dependence, which does not occur in the case of a small nanoparticle. However, in both cases, the lifetime decreases as the molecule and the nanoparticle approach each other. This suggests that, at the given wavelength, the non-radiative loss becomes more pronounced as the distance decreases. In the case of metal semi-infinite surface, this non-radiative energy loss has a maximum that corresponds to the surface plasmon at the interface. Obviously, the emission couples to the surface plasmons of the metal. In the case of metal nanoparticle, there is an infinite number of plasmon modes in the  $R \rightarrow 0$ :

$$\text{Re}[\epsilon(\omega_l)] = - \left( \frac{1+1}{1} \right) \epsilon_m, \quad l = 1, 2, 3.. \quad (2.60)$$

Consequently, they all participate in the non-radiative deexcitation of the molecule.

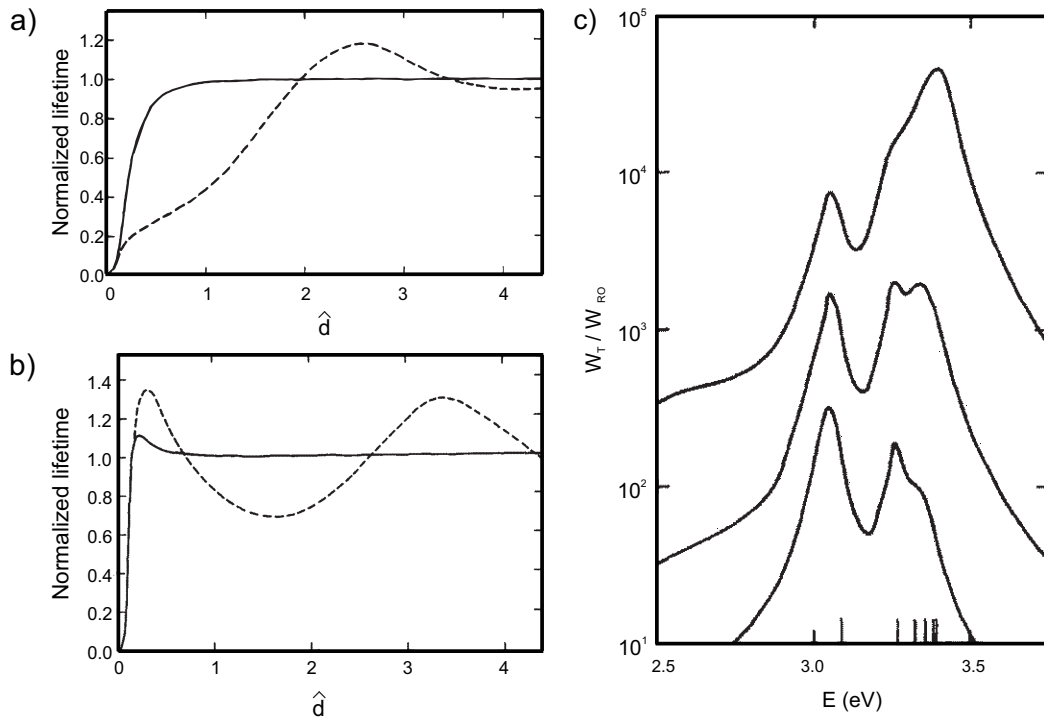


**Figure 2.10:** (a) Normalized lifetime as a dependence on distance  $\hat{d}$  from a silver nanosphere of radius 10 nm. The dipole polarization vector is perpendicular and the emission wavelength is 612 nm, showed in solid line. Normalized lifetime of the fluorophore as a dependence on the distance from silver surface is given in dashed line. (b) The same as in (a) but for parallel polarization of the molecule as compared to the surface of the nanoparticle. (c) Normalized rate of energy dissipation as a dependence on the frequency of the emitting dipole, for distances of 2 nm (upper curve), 5 nm (middle curve) and 10 nm (lowest curve) from the silver sphere of radius 10 nm. The vertical lines indicate silver surface plasmon frequencies position. Taken from Ref. [47].

Figure 2.10(c) shows the non-radiative decay rate of the molecule as a function of the energy of the emission emitted radiation for three selected distances of a molecule from the silver nanoparticle of 10 nm radius. The surface plasmon modes of the nanoparticle are shown in the bottom as vertical lines. The maxima positioned at 3 eV are due to the emission coupling to the dipole surface plasmon ( $l = 1$ ). It appears that as the molecule is closer to the nanoparticle higher plasmon resonance modes become more pronounced, whereas at larger distances the dipole plasmon mode is most dominant.

Overall, this is a reasonable approximation for the particle distances which are smaller than the nanoparticle dimension, i.e. when the non-radiative energy loss

of the molecule near a metal sphere is very similar to the one of the molecule near a metal surface. However, the radiative rates are highly dependable on the actual geometry of the system [48]. As mentioned, absorption properties depend on the environment of the molecules and they change if the molecule is in the vicinity of the metal nanoparticle surface. Changes in absorbance and radiative and non-radiative rates in the presence MNPs will contribute to the enhancement of the molecular fluorescence. The process occurs through the absorption of the energy by the molecule, which is followed by a population transfer and an emission process [49]. The absorbance cross-section is dependent on the square of the intensity of the EM field at the molecule position [48, 49], and therefore any enhancement of the local field contributed from the metal nanoparticle will as well be squared ( $A^2(\omega)$ ). The population transfer is the transfer from vibrational higher state of the excited ground level (described by the full width of the state ( $\gamma_1$ )) to the excited ground level, due to thermal decay ( $T_{01}$ ). Its transfer rate is given by the ratio of the thermal decay over the sum of all population decay rates from that vibrational higher sublevel of the excited state. The radiative rates will be enhanced by a squared factor from the same source, but at the molecules emission frequency ( $A^2(\omega')$ ). Finally, the non-radiative rate from the excited ground level may change due to the influences of several factors, distance-dependence being the most important one. The final enhancement factor of the influence of MNPs to the molecular fluorescence can be expressed as following

$$R_{fluo} = |A(\omega)|^2 |A(\omega')|^2 \frac{\gamma_1}{\gamma_1 + \Gamma_1^{(s)}} \frac{\Gamma_1 + T_{01}}{\Gamma_1 + T_{01} + \Gamma_1^{(s)}} \frac{\Gamma_0}{\Gamma_0 + \Gamma_0^{(s)}}, \quad (2.61)$$

where the superscript (s) is for additional rates that are induced by the nanoparticles [49].

Both enhancing and quenching of fluorophores fluorescence by the MNPs are being used in current research and applications in nanooptics, molecular biology, solar cells development, construction of novel biosensors and highly selective and sensitive detectors, etc [50]. For example, Tam *et al.* experimentally analysed the fluorescence intensity of indocyanine green dye molecule in the vicinity of gold nanospheres

and gold-silica nanoshells, by varying the dimensions of the nanoparticles as well as the distance between the dye and the nanoparticle [51]. Pure gold nanospheres slightly quenched the fluorescence, while gold-silica nanoshells enhanced the intensity of the fluorescence. The degree of enhancement depended on the radius of the nanoshells. The strongest enhancement (50x) was achieved for the nanoshells of diameter 123 nm, where surface plasmon resonance of the particle was overlapped with the emission of the dye. They found that the scattering efficiencies of bigger nanoshells affect the fluorescence, and modify the decay rates of the dye. It was concluded that the multipole surface plasmon resonances of the particles (with dipole and quadrupole being most pronounced in an experimental setting) should appear in a specific spectral range in order to enhance the fluorescence of a dye molecule with given excitation/emission characteristics. Zhou *et al.* were able to detect 1nM of mercuric ions in a solution by using 36 nm, 89 nm and 199 nm silver nanoparticles [52]. They employed hairpin DNA as spacers between a silver nanoparticle and 6-carboxyfluorescein molecule (FAM). By adjusting the length of the hairpin DNA, they succeeded in enhancing the fluorescence of FAM, which fluorescence signal was used as a detector for  $\text{Hg}^{2+}$ . The addition of mercuric ions caused the formation of duplex DNA, which in turn moved away FAM from the silver nanoparticle. Therefore, by following the decrement of FAM fluorescence intensity, the authors were able to detect as low as 1 nM concentration of mercuric ions in the solution. Same group of authors used the Ag NPs-hairpin DNA-FAM sensor in combination with magnetic nanoparticles attached to a target DNA [53]. After mixing the two solutions, due to DNA hybridisation, the two systems attach to each other. They were able to magnetically separate and detect the target DNA at sub-femtomolar concentration.

In a more realistic case, there is not just one molecule on the surface of the nanoparticle, but it can easily happen that there is the whole layer adsorbed on the surface. This complicates the analysis of the system, as it can absorb fair amount of the external radiation and damp the surface plasmon of the nanoparticle. It in return lowers the metal influence of the nanoparticle on the optical properties of the molecules [49].

## 2.3 Functionalization of noble metal nanoparticles

In the previous section, it was shown how noble metal nanoparticles can induce changes in radiative behaviour of fluorophores. Other properties of the molecules, for example the ionization energy, can also be affected when they are positioned in the vicinity of the metal nanoparticles surfaces. In the same time, molecules also influence the optical properties of MNPs, by affecting the positions of the surface plasmons. Therefore, by adsorbing molecules on the surface of MNPs, it is possible to obtain the synergetic effect and create the system that may exhibit the properties that cannot be found in its parts taken alone. This process of constructing new nanosystems by attaching molecules to the surface of nanoparticles is called nanoparticle functionalization or conjugation. It enables to tailor the properties of the nanoparticles toward desired properties. This even enables production of nanoplatforms that have several modes of application. In nanomedicine, for example, these multimodal nanosystems are called theranostics, and are very popular in area of developing agents for photothermal and photodynamic therapies, combined with imaging techniques.

Usually, inorganic nanoparticles are used for their optical or magnetic properties or simply as nanocarriers. The adsorbed molecules/molecular system have a role as differentiating agents, or are used for further construction of even more complex nanosystems. In turn, the adsorbed molecules are providing stability for nanoparticles, by physically preventing coalescence of MNPs, and/or by increasing nanosystems compatibility with the target material. There are different approaches for tailoring nanosystems, either by surface encapsulation of MNPs, *in situ* synthesis, or by self-assembly [54]. Very wide spectrum of materials can be used for functionalization of MNPs.

### 2.3.1 Functionalization of gold nanoparticles

#### Chemistry of gold nanoparticles surface

Due to high ratio number of surface to volume atoms in a nanoparticle and their lower coordination of surface atoms, nanoparticles have high surface energy. Consequently, nanoparticles generally benefit by adsorbing molecules. The variety of possibilities for functionalization of gold nanoparticles stems from rich chemistry of gold atoms, which is due to the pronounced relativistic effects [8]. Schoder *et al.* compared bonding strengths between  $\text{Au}^+$  and several ligands in gas phase [55]. The authors found out that the ligands bond to  $\text{Au}^+$  with the following order of the strengths of bonds for the reaction  $\text{Au}^+ + \text{L} \rightarrow \text{AuL}^+$  is for  $\text{L} = \text{Xe}$  (weakest)  $< \text{C}_6\text{F}_6 < \text{H}_2\text{O} < \text{CO} < \text{H}_2\text{S} < \text{CH}_3\text{CN} \approx \text{C}_2\text{H}_4 \approx \text{NH}_3 \approx \text{CH}_3\text{NC} < \text{CH}_3\text{SCH}_3 < \text{PH}_3$  (strongest). On the other hand, gold surfaces are considered as somewhat inert since the strength of the adsorption of the molecules on them is weak at room temperature [56]. However, there is some overlap in behaviour of thin gold surfaces and nanoparticles. For example, Weisbecker *et al.* reported on alkanethiolate ( $\text{HS}(\text{CH}_2)_n\text{R}$ ) monolayers assembled on gold nanoparticles of 20 nm diameter [57]. The authors followed the stability of the functionalized colloids over several neutral and acidic functional groups by changing pH of the solution and the number of methylene groups of the molecule. They concluded that the properties of the layers on Au NPs are similar to the layers formed on gold surfaces. Beside thiols, which have higher affinity to bound to gold nanoparticles than others [58], phosphanes and halides are also known to bind to gold [8].

Some of the bonding properties differ due to the size effects, as is the case that adsorptions of  $\text{H}_2$  and  $\text{O}_2$  adsorption occurs on gold clusters (29 atoms of Au), but not on the gold bulk surfaces ([59, 60], a vast review on the topic is given in Ref. [10]). The chemistry of gold nanoparticles became very popular research area when it was discovered that Au NPs of diameter up to 5 - 6 nm had unexpectedly efficient catalytic activity at lower temperatures than traditional catalysts. There are several possible sources that contribute to such behaviour: the large number of active sites of low-coordinated atoms on the surface of NP, metal-insulator transition changes

in electronic structure, or charge transfer from/to Au NPs are just some of them [61]. For example, Jenssens *et al.* confirmed the importance of coordination of Au atoms in gold clusters to adsorption of CO and oxygen molecule: the lower the coordination is, the stronger is the bond between Au atom and the molecule [61]. This was explained by higher energy position of lying d orbitals of low coordination number in these Au atoms, with respect to that with high coordination number [61, 62, 63].

### **Linking gold nanoparticles to complex macromolecules**

Beside the linking end-group of the functionalizing molecules that interacts with the surface of a nanoparticle, the rest of the molecule can influence physicochemical properties of the hybrid nanostructure. Molecules that have carboxyl groups and thiols can stabilize nanoparticles negative charge, and additionally be used to attach another target molecule. The latter enables virtually all molecules to be attached to the surface of Au NPs by using specific linkers for the connection between the NP and the target molecule. With that aim, Brennan *et al.* demonstrated usefulness of click chemistry [64]. In their proof-of-concept study, the authors used a linker molecule that had thiol and azide as its functional end-groups. Thiol groups ensured functionalization of gold colloid. On the other hand, azides react with terminal acetylenes of biomolecules in the presence of copper(I), forming 1,2,3-triazole. The authors used this process to successfully attach acetylene-lipase onto gold nanoparticles of 14 nm in diameter. They estimated that there were eight lipase molecules per nanoparticle, with fully retained activity.

Another example is Newkome-type dendron-stabilized gold nanoparticles, in work of Cho *et al.* [65]. The authors successfully attached several types of dendrons with disulphide cores onto citrate-capped gold nanoparticles, as the disulphide groups cleaved and thiol groups were produced. The functionalized nanosystem showed improved stability in physiological conditions, especially for pH values from mildly acidic to basic. Functionalization molecules can also be present during the formation of the nanoparticles. In that case, the molecules act also as capping agents that controls the growth of nanoparticles. One example is work done by Gar-



cia *et al.* [66], where 2-3 nm in diameter gold colloids were prepared in presence of poly-(amidoamine) dendrimers. The authors demonstrated successful conjugation of the particles by the primary amine terminal groups of dendrimers. It was shown that the shape and size of dendrimers influenced the size of novel hybrid nanostructure. By using flat and smaller in size dendrimers, the formed gold nanoparticles were less monodisperse with mean diameter bigger than in the case of using 4.5 nm in diameter spheroidal dendrimer. Similar approach was used for the preparation of stable gold nanoparticles functionalized by various cationic polyelectrolytes that contain primary ammonium groups [67], quaternary ammonium side groups as well as side groups with a partially positive nitrogen atom [68, 69].

### **Ligand exchange mechanism of NP functionalization**

As already mentioned, noble metal nanoparticles can enhance Raman scattering signal for several orders of magnitude, and this effect/method is called surface enhanced Raman scattering (SERS). By analysing influence of gold and silver nanoparticles on SERS signal multiplications, Freeman *et al.* found that the choice of functional group they used yield more or less successful increase of SERS intensity [70]. The authors reported that strength of gold nanoparticles interaction with thiol (SH) and amine (NH<sub>2</sub>) was comparable, but still stronger than with cyanide (CN). On the other hand, Stavens *et al.* demonstrated successful encapsulation of gold nanoparticles of 3-20 nm in diameter by three different resorcinarenes [71]. Resorcinarenes are cyclic oligomers made from benzene-1,3-diol and aldehyde. The conjugation with resorcinarenes improves functionalization efficiency with respect to dodecanethiol at same concentration by several times. The colloids obtained by conjugation by resorcinarenes of Au NPs bigger than 10 nm have higher temporal stability than gold particles functionalized with alkanethiols in hydrocarbon solutions. SERS measurement strongly suggested that the resorcinarenes were attached to the surface of gold *via* eight oxygen atoms located on the headgroup of the macromolecules. However, by exposing resorcinarene - functionalized Au NPs to alkanethiols, sulfur substituted oxygen interaction with gold surface which led to agglomeration of the nanostructures. Therefore, by carefully choosing the order of exposure of Au NPs

to different active molecular groups, it is possible to functionalize gold nanoparticles by using chemistry of ligand exchange, nicely reviewed in [72]. In that sense, it is also important to take into account the surface chemistry of the gold nanoparticles. For example, it is reported that Au NPs produced by using tetrahydroborate ions exhibit slower binding to amine- and mercaptosilanes, as compared to for example citrate capped Au NPs [73].

### **Application of gold nanoparticles in nanotechnology**

Gold nanoparticles have several modalities that can be exploited in construction of various sensors with supreme level of tunability: their optical sensitivity, the ability to influence the radiative and non-radiative behaviour of fluorescent species dependent on mutual distance, catalytic properties, electrochemical influence on the surrounding material, etc. Sensing nanoplatforms for toxic chemicals, heavy metal ions, organic molecules, and different types of vapors are just a few examples [3]. For example, nanoparticles can be used as building block in order to make superstructures with high degree of tuning of size, shape and functions. Shipway *et al.* reported on fabrication of the electrodes by deposition of gold nanoparticles formed on amine-functionalized indium-doped tin oxide (ITO) support [74]. Gold NPs were citrate-functionalized, which made them negatively surface-charged. By additional functionalization of ITO support with amine, electrostatic interaction between the layer of amine and citrate-capped gold nanoparticles enabled formation of Au NPs layer on top. This process can be repeated with addition of new crosslinkers on the top of Au layer, so another Au layer can be deposited on the structure. By controlling the number of Au NPs assembled onto ITO support, it was possible to tune the electrode sensitivity. By using electrochemical analysis, the authors concluded that such superstructures are both conductive and porous. Furthermore, by choosing appropriate crosslinkers, it is possible to tailor resistive characteristics of such assemblies. Similar idea was used to build quasi one-dimensional current path with gold nanoparticles between two metal electrodes by Sato *et al.* [75]. The 30 nm distant metal electrodes were printed onto silica using electron-beam lithography and covered by aminosilane. The sample was exposed to citrate - functionalized 10

nm gold colloid and consequently a submonolayer formed, having gold nanoparticles bound to free amine end groups on the surface. Introducing dithiol solution (SH-(CH<sub>2</sub>)<sub>6</sub>-SH) afterwards, one sulfur atom per molecule covalently attached to a gold nanoparticle, while the other thiol was oriented away from the surface. By repeating the sample exposure to gold colloid and dithiol solution several times, the gold nanoparticle chain was formed between the electrodes. Interestingly, an additional deposition of gold nanoparticles showed tendency of Au NPs to attach to the other already immobilized nanoparticles on the substrate, instead of directly to the substrate. In the following article, Sato *et al.* concluded that the Coulomb staircase current of observed three - nanoparticle chain could be explained by sequential single electron tunneling [76].

### **2.3.2 Functionalization of gold nanoparticles with biomolecules**

Functionalization or conjugation of nanoparticles with biomolecules is called bioconjugation. Biomolecules can be peptides, nucleic acids, proteins, antibodies, etc. They are usually chosen for providing biocompatibility of nanoparticles in biological samples and environments, or to promote participation of the nanosystems in biological processes [54]. Biocompatible molecules on the surface of MNPs can improve targeted drug delivery or to control the level of cytotoxicity of the nanosystems [77, 78]. Also, biofunctionalized nanoparticles are gaining more attention as contrasting agents for fluorescence and photoacoustic imaging as they can provide better noise to signal ratio than commercial dyes/agents [79].

One of the building blocks of biologically relevant macromolecules is the group of amino acids. Considering known chemistry of gold nanoparticles, it is obvious that the amino acids containing sulphur atoms will likely interact with gold nanoparticles [80]. Such case is for adsorption of cysteine and cystine amino acids. They are usually located on the proteins surface, which enables the interaction of sulphur and gold. This leads to the stable link with Au NPs, with cysteine being the strongest link [80, 81]. In the case of gold trimmer nanocluster, Pakiari *et al.* studied bonding

of cysteine and glycine to nanoclusters of gold and silver [81]. They recognized the bonding types in which the nanoclusters were electron or proton acceptors. In the first case, the bonding through selected parts of amino acids - amine, carboxylic and sulphur groups was analysed. In the second case, the nonconventional hydrogen bonds from amine ( $\text{N-H} \cdots \text{Au}$ ) and hydroxyl ( $\text{O-H} \cdots \text{Au}$ ) groups were of important contribution to the interaction. Comparing the energetics of the bonding of both amino acids, the authors concluded that the bonding *via* amine and carboxylic end-groups were very similar. The importance of sulphur atoms in the interaction of cysteine and gold surface was also emphasized in the study of Di Felice *et al.* [80]. In their analysis of cysteine (cys) adsorption on Au(111) surface, the bonding occurred *via* both thiol and amino functional end-groups. Their conclusion was that the chemisorption of cysteine is the most probable regime of adsorbance of both pure cysteine layer and of proteins containing cysteine layer. As for the amino acids lacking sulphur atoms, the main active sites for interaction with gold nanoparticles become carboxyl, amino and parts containing nitrogen.

In the case of tryptophan, Joshi *et al.* employed first-principles calculations based on density functional theory in order to elucidate the nature of interaction between tryptophan and gold nanocluster containing 32 gold atoms in a cage-like structure [82]. Their calculations showed that tryptophan interacts with the nanocluster *via* carboxyl and indole groups. By analysing projected density of states of the functionalized cluster, they confirmed the formation of hybrid orbitals between tryptophans highest occupied molecular orbital (HOMO) and gold *d*-level. These hybrid orbitals are delocalized at the interface and are a probable reason for experimentally observed fluorescence quenching of tryptophan by gold nanoparticles. On the other hand, the adsorption may differ depending on the mode of the preparation of gold nanoparticles. For example, tryptophan may adsorb differently to gold nanoparticles prepared by using citrate ions and to those prepared by using borohydride. This was shown by Hussain *et al.* [83], by following SERS spectra of tryptophan indole groups in the two cases. For the citrate-reduced Au NPs, tryptophan and related molecules are mainly perpendicularly oriented to the gold surface, with the amino groups interacting with gold atoms. In the case of borohydride-reduced Au NPs,

the flat orientation is achieved with indole stacking parallel to the surface.

Spontaneous adsorption of proteins to nanoparticles that lead to the formation of the protein layer is commonly called a protein corona of a nanoparticle. Depending on the strength of adsorption and stability of the proteins on the NPs surface, it can be either soft or hard corona. Characterization of both hard and soft coronas of nanoparticles is of utmost importance when speaking about potential nanoparticle-oriented biological applications [84, 85]. Exchange dynamics and/or stability of the surface molecules are one of the crucial aspects when assessing the effectiveness or activity of hybrid nanomaterial inside the living organism. Interaction of functionalized nanoparticles with live cells is rather complex. By introducing a functionalized nanostructure into a biologically active system, the nanostructure will be exposed to several chemically different surroundings on its way toward the target. It is observed that only several biomolecules can be found in hard coronas that are usually part of a standard biological surrounding. Consequently, it is important to foresee possible pathways of the nanostructure modification that can happen along. The nanoparticles' hard corona represents the initial "biological identity" of the hybrid nanostructure, which mainly influences its possible application. A careful choice of the interaction type of the nanomaterial with biologically relevant biomacromolecules might be a step forward in predicting the properties of the novel nanostructured objects, maximising the benefits and minimising the drawbacks.

### **2.3.3    Electronic structure of surface-modified gold nanoparticles**

An influence of noble metal nanoparticle on the fluorescent properties of fluorophores in their vicinity was discussed in Section 2.1. However, the molecules adsorbed on the surface of the nanoparticle may change its electronic cloud, and vice versa, the nanoparticle can influence molecular orbitals of adsorbed biomolecule. For example, Zhai *et al.* analysed CO adsorption on small gold clusters (up to 5 atoms) using photoelectron spectroscopy [86]. As the number of adsorbed molecules increased, the adiabatic and vertical detachment energies of the clusters were decreasing.

An increase in the interest in metal-organic interfaces arose with discovering of the electroluminescence of oligomers and conjugated polymers, which led to construction of polymer and organic light-emitting diodes [87, 88]. Since then, the research was focused on electronic properties of anode, cathode and polymer/macromolecule materials and their mutual influence, with the aim to maximize electroluminescence of organic material between two metal electrodes [89, 90, 91]. Typically, the electrode material is chosen in such way that the work function of the cathode (electrode for the injection of holes) is as high as possible, and vice versa for the electron injection, i.e. anode, materials [91, 92]. It was noticed that the work function of the electrode changes with the thickness of adsorbed biomolecule onto it, up to a certain value [93]. The effect was ascribed to a build-up of electron density at the interface. So, it was obvious that the interface layer did not behave as the biomolecule solely, nor was completely understood the ambivalent behaviour of the substrate. Oehzelt *et al.* constructed relatively simple yet detailed electrostatic model to describe the behaviour of interfacial regimes [92]. They concluded that the major influence to efficiencies of organic optoelectronic devices is in the density of states of the organic material deposited on the metal surface.

Ishii and co-workers noticed terminology inconsistencies in the literature and gave a clear review of energy level alignment for an organic layer and a metal macroscopic crystal surface [94]. They noted the existence of Fermi level ( $E_F$ ) of a molecule as a legit concept, since the molecular electrons are following Fermi statistics as well. The molecule ionization energy (IE) and electron affinity (EA), defined as the energy from the highest occupied molecular orbital (HOMO) and lowest unoccupied molecular orbital (LUMO) to vacuum level respectively, change when the molecule is near another object compared to when it is in the isolated state. The difference is caused by the change of potential field around the molecule. Due to the polarisation, IE might decrease, while EA might increase.

On the other hand, the work function ( $W_f$ ) of a metal crystal depends on the surface plane orientation. The reason for this effect is the fact that when electron is being ejected from a metal, the measured energy is the difference between Fermi energy and the energy of the electron being just outside the crystal. This influence can

change  $W_f$  for even 0.75 eV. So, considering that the Fermi level is the same for all electrons, the terminology for this observed change in  $W_f$  is said to be due to change of vacuum level near the surface ( $VL_s$ ) as compared to electron energy in infinity ( $VL(\infty)$ ). This change is explained as a consequence of the creation of a surface dipole layer in the crystal as the electron is being ejected, leaving positive charge in the crystal and making outside (vacuum) negative. The following analysis, although very helpful for the photoemission studies of metal-molecule interfaces, is actually artificial, since it relies on well-known disadvantage of conventional photoemission instruments of measuring PES relative to the Fermi level. In fact, our results on the gas-phase photoemission of functionalized gold nanoparticles, described in Section 4, show an absolute alignment of gold and molecule valence levels relative to the vacuum. Figure 2.11(a) depicts the metal crystal (left) and molecule (right) energy diagrams when they are far apart. When a thin layer of the analysed molecule is in contact with the metal surface, the vacuum level from the solid and the molecule is equalized, as represented at Figure 2.11(b). The most common representation of the same situation is the Figure 2.11(c), but without differentiating vacuum level far at the infinite distance. By adsorbing a molecular layer, the electronic clouds of both constituents might change. Also, depending on the actual electronic properties, charge transfer can happen, as well as the electronic rearrangement due to some chemical reactions at the interface. All this can cause formation a dipolar layer at the interface that can lower the vacuum level of the molecule ( $\Delta$ ), as depicted in Figure 2.11(d).

In the case when Fermi level of the molecular layer and the metal are not the same, some redistribution of the charge might happen, depending on the availability of electrons of both sides. If the organic layer is rather thick, small diffusion layer will be formed on the interface. This diffusion area can be considered as an area where band bending occurs in order to equalise the Fermi levels. The thickness of the diffusion layer depends on the dielectric function of the organic layer, the energy difference at the ends of the diffusion layer and the spatial distribution of electronic orbitals. The band bending is not usually expected to happen when the thickness of the molecular layer is of order of few nanometres.

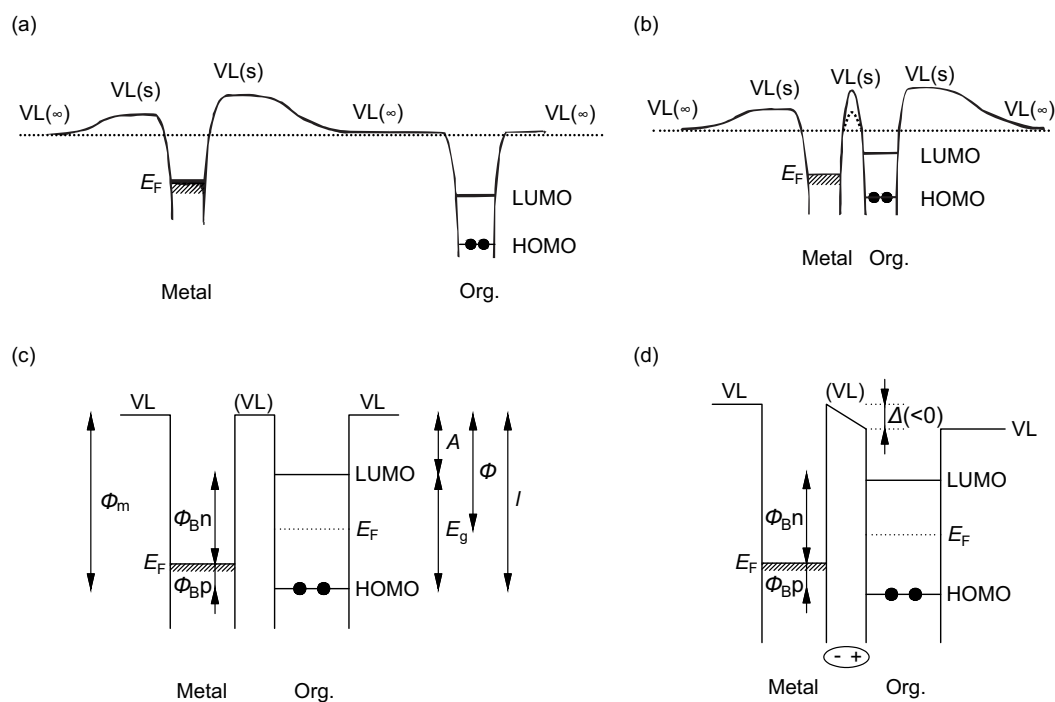


**Figure 2.11:** (a) Energy diagram of a metal crystal (left) and an organic solid (right) at infinite distance. (b) Energy diagram of the metal crystal (left) and the thin organic layer (right) when they are in contact. When the two come into the contact, the actual potential may change as shown by the dashed line between them. (c) Schematic of the plot in (a), assuming the common vacuum levels at the interface. (d) Interfacial energy diagram with a shift of vacuum level ( $\Delta$ ) due to the formation of the dipole layer at the interface. Taken from Ref. [94].



Demonstrative and straightforward method for analysis of the interface between an organic layer and a metal surface and their mutual influence is photoelectron spectroscopy. An exposure of the sample to monochromatic radiation causes ejection of an electron from the sample, which is called photoelectron. Kinetic energy of a photoelectron is equal to the absorbed photon energy transferred to an electron reduced by the binding energy of the electron in its initial state. Therefore, the distribution of the photoelectrons kinetic energy resembles the electronic structure of the sample. The core states can be probed by using X-ray radiation, while the use of vacuum-ultraviolet light enables examination of valence electronic shells. In this way, it is possible to probe and follow the differences of the surface electronic states when the organic layer is being deposited onto the metal surface. In Figure 2.12 is given exemplary photoelectron spectra of clean metal (Figure 2.12 (a)) and a metal with an organic layer deposited on its surface (Figure 2.12 (b)) obtained after exposure to vacuum-ultraviolet radiation. In the case of the metal spectrum, the photoelectron with highest kinetic energy is the one that was at the Fermi level prior to excitation (Figure 2.12 (a)). Considering that the measurements are done in non-ideal conditions, the fastest photoelectron gives the information of the work function of the analysed metal. In the case of the organic, the fastest photoelectrons will come from HOMO of the organic layer (Figure 2.12 (b)). Again, the difference between the radiation energy and the kinetic energy of the fastest photoelectrons will be the ionization energy of the organic molecule. On the other hand, the shift of the vacuum level due to the deposition of organic onto metal can be noticed as the shift in energy of the slowest photoelectrons in the both spectra. Furthermore, by comparing the energies of the fastest photoelectrons of the spectra, it is possible to extract the difference between Fermi level of the metal and HOMO of the organic layer. Both these quantities are presented in Figure 2.12 (c).

In general, the vacuum level can become higher or lower after the deposition of the organic material, but most frequently it is lower. However, neglecting the shift does not usually induce significant error in most of the cases [94]. The sources of the shift can be multiple. One possibility is the electron transfer between the organic layer and the metal separates the positive and negative charge on different sides of

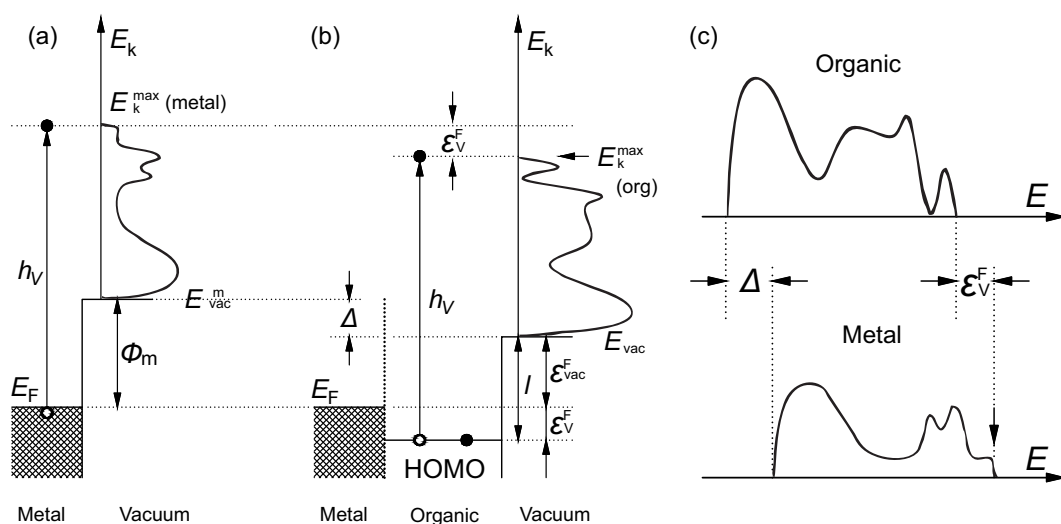


**Figure 2.12:** Schema of principle of the PES study of a metal surface (a) and the organic layer deposited on the metal surface (b). (c) Presentation of their spectra on the same energy abscissa. Taken from Ref. [94]

the formed interface. If the transfer route is from the organic toward the metal, the vacuum level is of lower value, and vice versa. Also, the charge image of a molecule formed in the metal can polarise the electronic cloud of the molecule, and change the energy levels in it. Similar but not the same effect of redistribution of electron cloud due to the presence of a metal might also be a reason for lower vacuum level of organic/metal sample. In the case of existence of chemical interaction between the organic and the metal substrate, the adjusting or/and formation of new bonds can also be a cause of VL shift. If the interfacial state is formed, the vacuum level shift can be changed by changing the metal and its work function non-linearly. This implies the existence of some intermediate state that is lowering the charge exchange and inclination of Fermi level aligning between the metal and the organic molecules. One example of the origin can be metal-induced gap states, due to metal wavefunction penetration into the adsorbed layer. Additionally, polarity of the molecules also influences energy diagram of the sample.

## 2.4 Application of biomolecule-functionalized gold nanoparticles in bionanotechnology

The nanomaterials show great potential for the applications in biology and medicine due to their versatility and tuneable properties. Moreover, their nanometric scale makes them size-compatible with wide spectrum of biologically active molecules [95, 96, 97, 98]. Targeted drug delivery, hyperthermia, photoablation therapy, bioimaging, biosensors, photodynamic and photothermal therapies are just some of rather active research areas where multiple benefits of using nanostructures were being reported. Also, the possibility of fabrication of multifunctional system attracts a lot of attention, cutting on the time consumptions of preparation procedures and enabling synchronous observations.

### 2.4.1 Biosensors based on gold nanoparticles

The sensitivity of the surface plasmon resonance of metal nanoparticles to the interaction with biomolecules was widely used in fabrication of commercial biosensors. These colloid-biosensors provided fast response, while at the same time, they could have been prepared with relatively simple experimental protocols using very small quantities of reactants. Reported SPR biosensor platforms include virus research, protein interactions, DNA interactions, research involving bilayers and vesicles, biomolecules binding affinities and many others [99, 100, 101].

High sensitivity of metal nanoparticles to changes in their surrounding mentioned above made them very eligible platforms for constructing nanoparticle-based sensors. Such sensors are consisted of two functional parts - one that would provide interaction/binding with the target, while the second part is responsible for signalling of such event. Gold nanoparticles draw attention in this area due to several benefits that can be achieved with application of this nanostructured material [3]. Their versatility in surface binding to a variety of biomolecules, together with the development of new procedures that promote biomolecule-metal nanoparticle binding, makes them an universal platform for wide area of applications. Also, a high chemical stability of gold nanoparticles makes these nanoplatforms physicochemi-

cally stable for prolonged time. In addition, core properties such as surface plasmon resonance of the nanoparticles stayed preserved, although modified to a certain extent. This provides stable detection and a robust way of tracking the change in sensing properties of these materials. Lastly, the possibility of tailoring physical properties of nanoparticle by changing their shape and size enables development of more facile and/or efficient nanoplatforms.

Two most basic modes of utilisation of gold NPs properties are their surface plasmon resonance (SPR) and quenching/enhancement of fluorescence of adsorbed fluorophores [3]. Gold nanoparticle sensors for detection of ionic species, metal ions, small organic molecules, oligonucleotides and proteins are based on changing of the SPR changing signals and they are usually called colorimetric sensors. On the other hand, fluorescence-based sensors are relying on gold influence on radiative and non-radiative behaviour of a fluorescent species. Quenching, or frequently called energy transfer, can be employed for detecting metal ions or small organic molecules. Furthermore, it is possible to make two-component nanosensors by combining quantum dots (semiconductor nanoparticles) with gold nanoparticles and follow their mutual optical response as a detection signal. Finally, nanoplatforms containing fluorescent polymer-functionalized Au NPs are able to differentiate and discriminate between types of proteins, bacteria, cancerous or healthy human cells. Another type of sensing platforms, based on electrical, electro-chemical and catalytic properties of nanostructured gold, are constructed for vapour sensing, toxic chemicals, drugs efficiencies, enzymatic activities, tumorous biomarkers, etc.

For example, Elghanian *et al.* reported on making highly selective biosensor platform for detection of polynucleotide chains [102]. Their system was constituted of three parts - two different oligomers with thiol groups on one end and 13 nm gold nanoparticles. The nanoparticles were functionalized with these two oligomers, and the solution had characteristic pink colour, due to the surface plasmon resonance of Au NPs. After mixing the solution of hybrid probes with target polynucleotide, both probe oligomers would align contiguously on the target polynucleotide. Due to the hybridization, gold nanoparticles would decrease their interparticle distance, and consequently the surface plasmon resonance would blue-shift. The authors reported

that the colorimetric platform detected 10 femtomoles of the target in unoptimized conditions. This two-state platform also showed high temperature sensitivity - it was possible to detect transition from blue to pink by increasing the temperature of the solution by 1°C. That allowed the discrimination between the cases when the target polynucleotide was a perfect complement and with mismatch targets with just one substitute.

Another example of a highly sensitive biosensor was demonstrated by Lyon *et al.* [103]. The authors used antibody functionalized gold thin surface and antigen functionalized gold nanoparticles of 11 nm in diameter. By following surface plasmon resonance shift of the system, they were able to detect picomolar concentration of human immunoglobulin G. Dykman *et al.* developed a similar protein assay based on trypsin functionalized gold nanoparticles of 15 nm in diameter [104]. On the other hand, gold nanoparticles can be used as a tool to gain information about some functionalities or properties of biomolecules, or to improve their functions. Brown *et al.* used SnO<sub>2</sub> electrodes modified with 12 nm Au nanoparticles to follow reversible electrochemistry of redox protein horse heart cytochrome c [105]. Also, pepsin-conjugated gold colloid showed same biocatalytic activity as pepsin alone, but with improved stability compared to the free enzyme in solution [106].

On the other hand, biomolecules can be used in lego-like construction of nanostructured hybrid material. The most obvious biomolecule for such purpose is DNA. For example, Mirkin *et al.* functionalized gold nanoparticles with two non-complementary DNA oligonucleotides by adding thiol endgroups [107]. By introducing complementary duplex DNA chains with pairs for both types of oligonucleotides, gold nanoparticles self-assembled into macrostructure. The authors showed de- and rehybridization by changing temperature of the solution from 0°C to 80°C.

Another powerful nanoplatform is based on gold nanoparticles functionalized by fluorescent poly(p-phenyleneethynylene) (PPE) derivative by using so-called chemical nose/tongue approach, developed by Rotello and his group [3, 108, 109, 110]. It uses a possibility of detecting differential highly selective interactions between the hybrid nanostructure and targets. For example, You *et al.* reported on successful identification of 52 unknown protein samples that had seven different proteins [109].

The main principle was that the fluorescence of PPE was initially quenched by gold nanoparticles (2 nm in diameter). Addition of protein samples caused competitive binding to the polymers, which in turn activated polymers fluorescent signal (Figure 2.13(a)). By using linear discriminant analysis, the successfulness rate of Au NPs-PPE sensor array in blind tests was 96.4%. Another application of analogous nanosystem was demonstrated by Phillips *et al.* [110]. By using another similar PPE polymer-functionalized gold nanoparticles (1.6 nm in diameter), the authors succeeded in detecting and classifying 12 bacteria strains (Figure 2.13 (b)), both gram-positive and -negative. For bacterial strain discrimination ability, the authors constructed three hydrophobic ammonium-functionalized nanoparticles, all having additionally adsorbed specific fluorescent PPE polymer. By scanning all combinations of nanosystems with the strains, the authors constructed parameter space in which it was possible to separate different bacteria types.

Versatility of this type of platform is proven in another study of the same group. Bajaj *et al.* studied interaction between same hybrid nanoplatform and mammalian cells [111]. They utilized competitive differential binding between PPE-CO<sub>2</sub> and Au NPs system and cell types during the incubation of the strains in a buffer containing the nanoparticles. Due to their cationic nature, the nanoparticles were expected to interact with phospholipids, membrane proteins and carbohydrates, causing detachment of PPE. Consequently, fluorescent signal was appearing due to free PPE in the solution. The discrimination was possible due to different affinities of Au NPs relating the compositions of the cells surfaces (Figure 2.13(c)). By employing their linear discriminant analysis, the authors were able to distinguish between different cell types, healthy and cancerous cells, as well as isogenic normal, cancerous and metastatic murine epithelial cell lines.

## 2.4.2 Microscopy techniques involving gold nanolabelling - bioimaging

Another very important application of biomolecule functionalized nanosized gold is in microscopy. It was introduced in 1971 by Faulk *et al.* for transmission electron

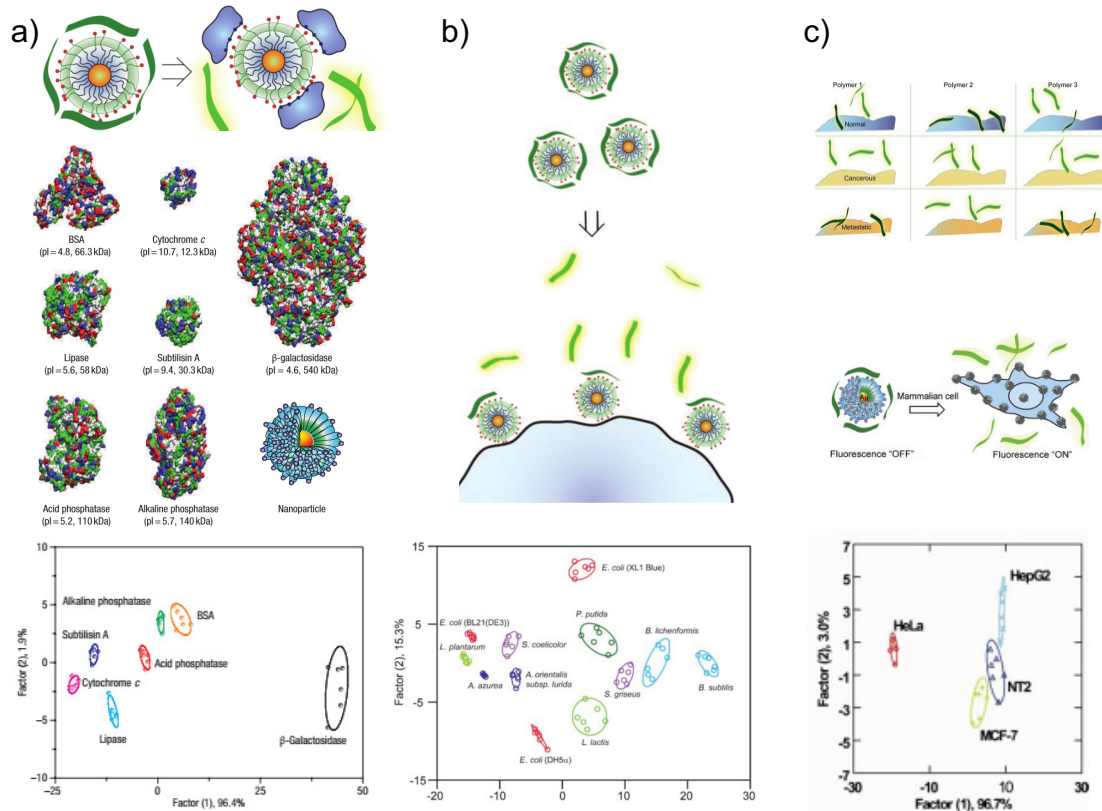


**Figure 2.13:** Schematic representation principle of the fluorescent sensor based on gold nanoparticles capped with fluorescent polymer, and a set of seven proteins that were tested for assessing sensing performances of the hybrid nanomaterial. The graph: canonical score plot for the fluorescence response patterns obtained with the constructed sensor against 5 M proteins. Taken from Ref. [109]. (b) Schematic representation of the displacement of the fluorescent polymers from the nanoparticles by the bacterial surfaces. The canonical score plot for the response patterns differing 12 bacterial strains. Taken from Ref. [110]. (c) Schematic presentation of the human cell detection assay and the interaction between the nanostructure and cell types. Canonical score plot for the response patterns differing four human cancer cell lines. Taken from Ref. [3, 111].

microscopy [112]. Due to gold high electron density and ability to bind antibodies, Faulk and Taylor recognized the potential of gold compared to at that time reported protocols that used mercury and uranium. After functionalization with rabbit anti-salmonellae serum, gold colloid, called immunocolloid by the authors, was exposed to salmonellae. They concluded that the antibodies activity was still intact and successfully employed immunocolloid as localization labels for electron microscopy. Furthermore, it was shown that it is possible to differentiate two types of antibody-functionalized gold nanoparticle labels that were different in size and/or shape. In later years, immunocolloid labels shown applicability in scanning electron [113, 114, 115] and atomic force microscopy [116]. By 1983, it was already known that colloidal gold can be functionalized with variety of biomolecules (metabolites, enzymes, plasma proteins, endotoxins) and used as a versatile probe for cellular processes, e.g. receptor-ligand binding, enzyme-substrate reactions and transcellular pathways [117]. This technique is now called immunogold labelling method and it is a widely applied well-standardized protocol [118, 119].

Nowadays, nanomaterials can be used in microscopy in order to either generally increase signal of the sample without any specific affinity, or to use it as means for "targeted imaging". Both these approaches consider nanoparticles as a passive labels [15]. General staining procedure is comprised of internalization of nanomaterial by the biological species. Afterwards, either the core materials' properties or functionalization molecules define the type of a microscopic technique that would be used. On the other hand, targeted imaging implies the use of specific precursors attached to the nanomaterial with the aim of vectoring them toward specific domains, as in already mentioned immunogold labelling. Another modality of nanomaterial application in microscopy employs nanoparticles' intrinsic sensitive properties to external conditions to be used as additional differential labels. Their labelling signals appear due to the existence of different conditions in some sample's domains, due to occurrence of some specific process. Application of such sensing labels, usually called probes, are in imaging of pH values, oxygen distribution, glucose production, temperature screening, etc. [15].

The benefits of using inorganic nanoparticles as labels in fluorescence microscopy



are due to their distinctive photostability rate and easily obtained inertness. They are also attractive as microscopic labels due to a wide spectrum of molecules that can be loaded onto nanomaterials. Additionally, several techniques can be used on very same samples in order to gain more insights and confirm information about the system, e.g. light microscopy combined with electron microscopy. Molecules used for functionalization of nanoparticles can in turn increase biocompatibility, cell permeation and stability of the nanomaterial. By appropriately choosing pairs of molecule-nanoparticle material, multiple benefits can be obtained, as for example imaging contrast can be enhanced and toxicity can be significantly reduced.

Examples of gold nanosystems used in biological imaging range from nanoclusters to the nanoparticles several hundreds of nanometre in size. Gold nanoclusters can exhibit fluorescent properties due to their reduced dimensions. Electronic states of such small object are bridging between atom-like and crystal-like behaviour, having separated electronic levels and therefore enabling electronic excitations. Their emission energy is scalable with the number of atoms in clusters as  $E_{\text{Fermi}}/N^{1/3}$ , where  $E_{\text{Fermi}}$  is Fermi energy of gold (5.53 eV) [120]. Even though gold nanoclusters usually lose their ability to fluoresce at size of few nanometres, there is an increasing number of reported syntheses of fluorescent Au NPs in different size ranges and shapes [120, 121, 122, 123]. The novelty of the experimental procedures renders their recent research popularity in tumour labelling, imaging, cancer therapy, molecule and nucleus labelling, etc., due to the benefits that can be obtained by using such non-toxic, stable and bright probes [79].

On the other hand, more widely spread use of gold nanoparticles in bioimaging is as nanocarriers of fluorescent labels. In this case, default non-fluorescent gold nanoparticles are employed as the base for building a structure containing frequently several functional molecules, while perserving their properties. An example of such hybrid structure is Ruthenium(II) polypyridyl gold nanoparticles in role of cellular imaging agents fabricated by Elmes *et al.* [124]. By following fluorescence of Ru(II) by using confocal fluorescence microscopy, the authors localized the nanostructures in cytoplasm and nucleus of HeLa cells, implying that Ru(II)-complexes kept their DNA targeting activity. They additionally confirmed the findings and stability of

gold nanoparticles by TEM localization.

When it comes to stability of hybrid structure *in vivo*, it is very important to be aware of the possibility that gold nanoparticles' corona, i.e. the functionalization material, is not strongly bonded. Therefore, an exchange of (macro)molecules from the Au surface can happen when exposed in biologically active medium, due to not equal affinity of biomolecules toward gold nanosurface. For example, Jana *et al.* overcame such threat by synthesizing cysteine-functionalized polyaspartic acid based polymer that was strongly attached to gold and silver nanoparticles [21]. They demonstrated the benefits of the polymer-capped Au NPs in a superior stability under the exposure to biological conditions, as well as the possibility for additional conjugation with variety of antibodies. The functionalized nanocomplex was successfully employed as cell-labels of mouse breast cancer cells studied by fluorescence and confocal microscopy.

Another interesting example is rhodamine 6G - functionalized gold NPs in the study of Jaworska *et al.* [125]. Rhodamine 6G (R6G) is a commercial fluorescent dye that being attached to gold nanoparticles, SERS enhancers, offered multimodality of its detection. It enabled use of both fluorescence and Raman-scattering microscopy. The study was conducted with the aim of elucidating intracellular composition of endothelial cells, rather important part of the regulator body of e.g. blood fluidity, thrombosis, immune response and inflammation. By following the fluorescent signal, intracellular localization of the nanosystem was obtained, while following SERS signals, it was possible to deduce dynamics of R6G detachment and attachment of intracellular molecules onto Au NPs, and their identification. The study showed promising success in obtaining information on the cells' biocomponents. Another example of functionalized gold nanoparticles is tryptophan-capped Au NPs by Kim *et al.* [126]. The green synthesis of gold NPs was carried out under several tryptophan (Trp) concentrations in different temperature conditions. The authors showed successful reduction of gold salt that led to formation of the functionalized gold colloid solution. Afterwards, the hybrid nanostructure was tested negative for toxicity in human neuronal cells, which proved green approach of the study. Trp-Au nanosystem was used as a labelling agent in fluorescence microscopy. The authors

reported on distinguishing signals coming from the colloid from autofluorescence of the neuronal cells in neutral and alkaline conditions, which had imposed a safer and sustainable alternative to commercially available labelling dyes.

### 2.4.3 Other applications of gold nanoparticles in bionanotechnology

The diversity and complexity of materials eligible for functionalization of gold nanoparticles, as well as the fact that gold is intrinsically nontoxic, biocompatible and inert, renders gold nanoparticles as a good candidate for drug delivery systems [77, 95, 96, 127, 128]. It is generally accepted that the efficacy of the drug can be increased by locally increasing its concentration through loading onto the nanoparticles. Josh *et al.* reported on the effects of blood glucose levels in diabetic rats when insulin was introduced standardly and while adsorbed on the surface of gold nanoparticles [97]. They used two types of adsorption of insulin: by thiol and amine covalent bonds onto bare gold nanosurface and by presumably hydrogen bonding and electrostatic interaction of insulin onto aspartic acid-functionalized gold nanoparticles. In the latter case, easier release of insulin in the blood stream was demonstrated. The authors observed maximal decrease in glucose levels within 3 h after transmucosal administration (55%) that is comparable with current trends of insulin use, but emphasising the importance of insulin - gold nanocarriers as an alternative to painful standard subcutaneous delivery.

On the other hand, the main aim of targeted nanosystems in cancer therapies is an efficient nanostructure that causes cancer cell death that would preserve healthy cells from damage. Gold nanoparticles represent stable platform for this purpose, due to the possibility of loading even more than one type of molecules. Variety of strategies for covalent or non-covalent adsorption of drugs, and gold controlled characteristics is of a great advantage. For example, Brown *et al.* [129] studied efficiency platinum-based anticancer drugs for chemotherapy when loaded onto PEG-capped gold nanoparticles. They demonstrated equal or significantly better impact of the drugs when being introduced in lung epithelial cancer cell line and several lines of

colon cancer. It is also possible to optimize the hybrid nanosystem so it can easily penetrate cellular membranes and release critical amount of drug, either by internal or external triggering [98]. Internal triggering is usually adsorbed molecule-related, relying on the abrupt increase in concentration of some specific (macro)molecule in intracellular space. Such example is glutathione, with higher affinity toward gold surface than the adsorbed drug (reviewed in [127]). Consequently, it binds to the nanoparticles, releasing the drug into the cytoplasm. The other, external, trigger is based on tailored nanoparticle's specific property, which is usually implemented by having photoresponsive nanocages that are containing drug molecules.

Gold nanoparticles can be also employed as nanocarriers providing not only targeted drug delivery, but also enabling cell penetration for the macromolecules that would not otherwise enter the cytoplasmic space. Ghosh *et al.* [77] reported on successful internalization of membrane-impermeable enzyme into variety of cell lines by using peptide-capped gold nanoparticles (2.5 nm in diameter). Peptide chains had three different end-groups and their roles were protein surface recognition and plasma membrane association. Afterwards, the hybrid nanostructure was functionalized by the enzyme,  $\beta$ -galactosidase, already tagged with a fluorescent dye. By employing confocal laser scanning microscopy, the authors concluded that the nanostructure enabled cell internalization of the enzyme, and, moreover, that the enzyme was localized in cells cytoplasmic space, proving versatility of gold nanoparticles as nanocarriers. Similarly, Li *et al.* [130] demonstrated efficient uptake of daunorubicin, a cancer drug, by the drug-resistant leukemia K562 cells in presence of 3-mercaptopropionic acid-caped Au NPs, which was separately introduced into the leukemia cell solution, while making negligible difference in healthy cell solutions. Furthermore, Tao *et al.* [78] demonstrated beneficial effect of incorporating Au nanoclusters in already recognised nanocarrier for gene therapy polyethyleneimine (PEI). PEI demonstrated as a good candidate for gene delivery due to its high DNA binding affinity. The major downside of PEI was cytotoxicity, which was the reason why the authors tested the behaviour of a structure based on PEI and gold nanoclusters. The analysed system had lowered cytotoxicity, while transfection efficiency of PEI increased. Additionally, fluorescence of gold nanoclusters was used for

imaging of the samples, proving the hybrid nanostructure had multiple application benefits. In 2010, nanoplateform consisting of 27 nm gold nanoparticles, capped with thiolated polyethylene glycol and human tumour necrosis factor alpha (rhTNF) went phase I dose escalation clinical trials in advanced stage cancer patients [131]. The results of electron microscopy showed that localization of gold nanoparticles after 24 h after treatment in patient biopsies of tumour and healthy cells, preferentially in tumorous cells, by using electron microscopy. The authors concluded that this novel nanomedicine treatment increased non-toxicity level of the rhTNF compared to rhTNF alone, and that the future clinical trials would be including this nanoplateform as an addition to approved chemotherapies.

Another important area of gold nanoparticle application is photothermal therapy (PTT) of cancers, a minimally invasive alternative to surgical removal of malignant tissues. The idea of PPT is that the exposure to specific electromagnetic radiation of the certain area of a cancer cells causes the necrosis of the cells by locally increasing temperature of the tissue. The major downside of such approach is high damage rate of surrounding healthy cells. Advancement in PTT was achieved by introducing agents with targeting functionality that would increase specificity of the area under radiation influence. By exposing gold nanoparticles to electromagnetic radiation at the SPR wavelength, absorbed light can be converted to heat by electron-phonon and phonon-phonon processes in a picosecond time domain [132]. Therefore, gold nanoparticles, as being able to be nanocarriers as well as having convenient thermal properties, became a very potent candidate in a role as photothermal agents.

#### **2.4.4 Fluorophore-bifunctionalized gold nanoparticles and nanogold influence on fluorescent properties of the fluorophore-pair**

As seen in the previous section, nanoplateforms produced for targeted drug delivery include usually two molecules with different functionalities, attached to a nanocarrier. One type serves as guidance toward the target, e.g. cancerous cells, with the aim of improving efficiency of the drug by avoiding healthy cells. The other is the

drug that is released when the nanoplateform penetrates the target, that is triggered or not by the design of the platform. Attaching more than two molecules on the nanoparticles might be possible, for example as a fluorescent label, but it is not so often the case, as it can increase complexity of procedural steps in the platform synthesis. On the other hand, nanogold might have an additional role besides being a nanocarrier - it can be used for imaging, e.g. absorbance or dark-field microscopy. Most of hybrid nanostructures do possess multimodality. They enable utilisation of (often several) imaging technique(s) for localization and in the same time might include therapeutic functionality.

All these examples make use of the properties of separate constituents of the hybrid nanostructure that persists in the process of building. On the other hand, the collective properties can differ from the simple sum of the nanosystem components. As seen in Section 2.1.3, metal nanoparticle in a vicinity of a fluorophore changes its radiative behaviour. Therefore, the process that relies on electromagnetic characteristics and interactions of a system can be and will be modified when noble metal nanoparticles are introduced in the system. Such example represents resonance energy transfer (RET) between two fluorophores possessing certain and related electromagnetic properties.

### **Resonance energy transfer between two fluorophores**

Resonance energy transfer is one of the most known intermolecular photophysical effect in fluorescent systems. It can be described as long distance electromagnetic interaction of two fluorescent molecular species. It represents energy migration from excited molecule (donor, D) to a molecule in ground state (acceptor, A), that have mutually appropriate spectral characteristics [133, 134, 135, 136]. The resonant in RET stands for a necessary condition for RET to happen - the emission spectrum of donor overlaps to some extent with absorbance/excitation spectrum of the acceptor molecule. If this condition is satisfied, a real or virtual photon can be exchanged between D and A. In the first case, the donor molecules fluoresce and that photons are being absorbed by acceptor molecules, separated on average distances comparable to the wavelength of emitted photon. The donor fluoresce decay rates are not

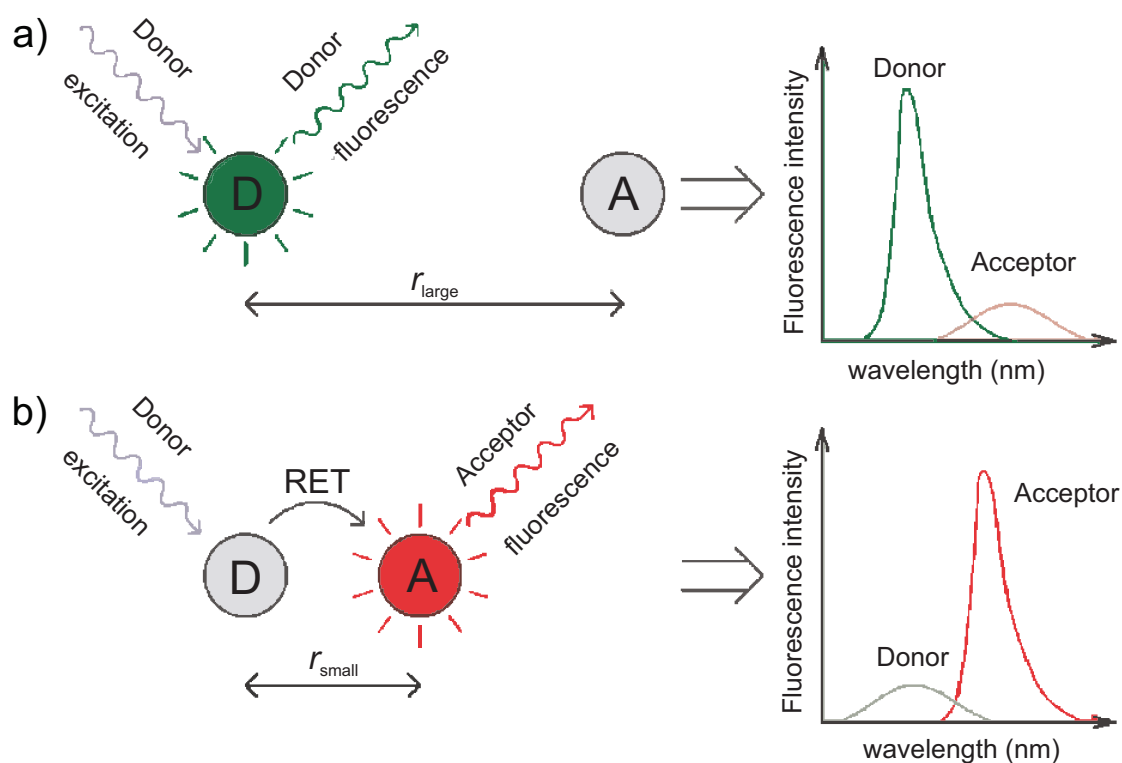


**Figure 2.14:** Schematic representation of resonance energy transfer between donor (D, green) and acceptor (A, red) fluorophores. A decrease of the distance between the donor and acceptor, the relative fluorescence intensities from D and A would change in favour of the A fluorescent signal. Taken from Ref. [134]

changed by this event [133]. On the other hand, if the mean distance between the molecules in solution is of order of 10 nm or less, it is a virtual photon that is exchanged. In literature, this process is referred to as Förster or fluorescence resonance energy transfer (commonly used as acronym FRET), or non-radiative energy transfer. In this case, the donor fluorescence decay rate is shortened, due to opening an additional non-radiative channel for donor's deexcitation. Consequently, donor's fluorescence decreases while the acceptor's, by being additionally excited, increases. This is schematically represented in Figure 2.14. It is usually classically described as long range Coulombic dipole-dipole interaction between the excited donor and an acceptor in ground state, viewed as a point dipoles [134, 135].

The full description of RET employing molecular quantum electrodynamics can be found in the beautifully written book by Akbar Salam [137]. It is based on the work of D. L. Andrews, which will be shortly presented here [138]. He was the first

to recognize that the exchange of a real and a virtual photon in resonance energy transfer processes are due to the same underlying mechanism, but on just different distance scales. For small distances, nonradiative transfer depends on pair-distance as  $R^{-6}$ , while radiative transfer depends as  $R^{-2}$  due to the retardation effects.

The Hamiltonian of the system consisting of a single donor molecule (D) and a single acceptor molecule (A), coupled to the radiation by dipolar coupling, has the form:

$$H = H_{mol}^D + H_{mol}^A + H_{int}^D + H_{int}^A + H_{rad}, \quad (2.62)$$

where the  $H^D$  and  $H^A$  represent unperturbed Hamiltonians of the molecules.  $H_{int}^D$  and  $H_{int}^A$  are the dipolar interaction operators given by:

$$H_{int}^D = -\boldsymbol{\mu}_D \times \mathbf{d}^\perp(R_D)/\epsilon_0, \quad (2.63)$$

$$H_{int}^A = -\boldsymbol{\mu}_A \times \mathbf{d}^\perp(R_A)/\epsilon_0, \quad (2.64)$$

and the radiation Hamiltonian is

$$H_{rad} = \frac{1}{2} \int (\epsilon_0^{-1} \mathbf{d}^{\perp 2} + (\epsilon_0 c^2 \mathbf{b}^2)) d^3 \mathbf{r}. \quad (2.65)$$

Here,  $\boldsymbol{\mu}_D$  and  $\boldsymbol{\mu}_A$  are dipole moment operators for the molecules D and A located at  $\mathbf{R}_D$  and  $\mathbf{R}_A$ , while  $\mathbf{b}$  and  $\mathbf{d}_\perp$  represent the radiation field's magnetic and transverse electric displacement operators. The latter can be showed as an expansion as:

$$\mathbf{d}_\perp = \sum_{\mathbf{k}, \lambda} \left( \left( \frac{\hbar c k \epsilon_0}{2V} \right)^{1/2} \times i(\mathbf{e}^\lambda(\mathbf{k}) \mathbf{a}^\lambda(\mathbf{k}) \exp(i\mathbf{k}\mathbf{r}) - \bar{\mathbf{e}}^\lambda(\mathbf{k}) \mathbf{a}^{+\lambda}(\mathbf{k}) \exp(-i\mathbf{k}\mathbf{r})) \right) \quad (2.66)$$

where  $a$  and  $a^+$  are an annihilation and creation operators for a radiation mode with wave vector  $\mathbf{k}$ , while  $\mathbf{e}$  is polarisation vector, and  $V$  is the quantisation volume. Time-dependent perturbation gives the probability amplitudes for emission and absorption processes between the initial state  $|i\rangle$  and the final state  $|f\rangle$ :



$$M_{fi} = \langle f | H_{int} | i \rangle + \sum_r \frac{\langle f | H_{int} | r \rangle \langle r | H_{int} | i \rangle}{E_i - E_r} + \dots \quad (2.67)$$

The first term in the perturbation series defines the exchange of a real photon, while the second term is for a virtual photon. For the nonradiative transfer, both time ordering have to be included into calculations. This means that the virtual photon can propagate from D to A, but also in reverse order, from A to D, viewed from the point where time goes backwards. After summation over  $\lambda$  and  $\mathbf{k}$  (the wave vector of a virtual photon), the total probability amplitude for an exchange of a virtual photon is given by:

$$M_{t\uparrow+t\downarrow} = \mu_i^{0m(A)} \mu_j^{m0(D)} V_{ij}(\mathbf{k}, \mathbf{R}), \quad (2.68)$$

where  $\mu^{m0}$  is the transition dipole moment for the transition  $|m\rangle \leftarrow |0\rangle$ ,  $\mathbf{R}$  the molecules' mutual distance, and  $V_{ij}$  is a tensor representing retarded resonance electric dipole-electric dipole coupling, given by:

$$V_{ij}(\mathbf{k}, \mathbf{R}) = \sigma_{ij} + i * \tau_{ij}. \quad (2.69)$$

The functions  $\sigma$  and  $\tau$  are defined by:

$$\begin{aligned} \sigma_{ij} = (4\pi\epsilon_0 R^3)^{-1} \times ((\delta_{ij} - 3R_i R_j)(\cos(\kappa R) + \kappa R \sin(\kappa R)) - \\ - (\delta_{ij} - R_i R_j) \kappa^2 R^2 \cos(\kappa R)), \end{aligned} \quad (2.70)$$

and:

$$\begin{aligned} \tau_{ij} = (4\pi\epsilon_0 R^3)^{-1} \times ((\delta_{ij} - 3R_i R_j)(\kappa R \cos(\kappa R) - \sin(\kappa R)) - \\ - (\delta_{ij} - R_i R_j) \kappa^2 R^2 \sin(\kappa R)). \end{aligned} \quad (2.71)$$

Finally, the rate equations can be derived by using Fermi golden rule as:

$$\Gamma = \frac{2\pi}{\hbar} |M|^2 \rho_f, \quad (2.72)$$

where  $\rho_f$  is the density of final states of the acceptor. After averaging on the rotations of the dipoles, the rate has following form:

$$\Gamma^{nonradiative} = \frac{2\pi|\mu^{0m(D)}|^2|\mu^{m0(A)}|^2\rho_f}{9\hbar}A(k, \mathbf{R}), \quad (2.73)$$

where  $A$ , the excitation transfer function representing a relativistic formulation of the dipolar coupling, is given by:

$$A(k, \mathbf{R}) = V_{ij}(k, \mathbf{R})\bar{V}_{ij}(k, \mathbf{R}) = 2(4\pi\epsilon_0R^3)^{-2}(3 + k^2\mathbf{R}^2 + k^4\mathbf{R}^4). \quad (2.74)$$

In the near zone regime, where  $kR \ll 1$ , the distance dependence of the rate has a familiar Förster  $R^{-6}$  dependence, while in the opposite case, far-field regime  $kR \gg 1$ , the rate has the same form as for the radiative exchange of energy between the molecules. So this theory is valid for all distances starting from the separation of the molecules where their orbital clouds are not overlapping. The latter is called Dexter energy transfer, and it is not considered by this theory.

Resonant energy transfer opens a new deexcitation path for the donor molecules. Consequently, the donor's radiative lifetime decreases in the presence of acceptor molecules. This in turns increases the photobleaching rates of the donor fluorophores, due to depopulation of the donor's excited state [139, 140, 141, 142]. By measuring time-lapse fluorescence intensity of the donor in the absence and presence of the acceptor molecules, it is possible to gain insight into the efficiencies of RET. Such approach was used by Young *et al.* [139]. By multiexponential fitting of the kinetic fluorescence signals as shown in Figure 2.15, the authors succeeded in quantifying the RET efficiencies between proteins inside cell lines. Another technique that makes use of the causality of the RET pairs' fluorescence by using photobleaching of the fluorophores is acceptor bleaching (donor recovery) RET [143, 144]. In situations where the donor and acceptor emissions are too close, their RET dynamics is hardly detectable by standard fluorescence channel collection. The proposed technique benefits from photobleaching of acceptor to gain insight into donors fluorescence and was successfully used in RET microscopy for two commercial dyes - green and yellow fluorescent proteins [143].

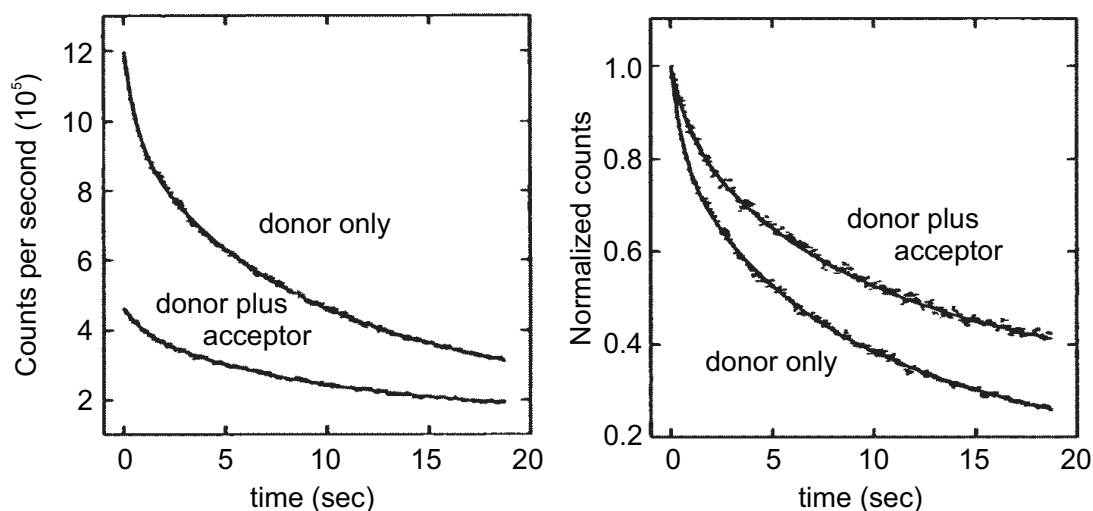


**Figure 2.15:** A typical experimental data from of a donor molecule alone, and donor in the presence of acceptor in the RET study of Young *et al.* Left graph represents raw data points and fitted curves, while their normalization to the initial intensities are plotted in the right graph. Taken from Ref. [139].

### Metal nanoparticle influence on resonance energy transfer processes

As seen in the previous section, the presence of metal nanoparticles influences radiative and nonradiative rates of fluorophores. When there is a metal nanoparticle in the vicinity of a pair of the molecules manifesting resonance energy transfer, there are several processes competing. Beside changing radiative and nonradiative rates of each fluorophore, the metal nanoparticles can actively assist the transfer and therefore increase the transfer efficiency [48, 145]. Hua *et al.* developed a theoretical approach for the calculation of the RET amplification between a pair of fluorescent molecules due to the presence of the solid state nanoparticles [145]. The authors treated RET as a manifestation of a dipole-dipole interaction of the RET pair in the electrostatic approximation. They included the presence of the nanoparticle *via* a modification of the potential which the RET pair was in. The RET enhancement depended on the mutual distances, the shape of the solid nanoparticle and on the frequencies on which the resonance transfer was happening with the respect to the plasmon resonance of the particle. The authors explained the cause of the amplification as a induction of a multipole moments in the nanoparticle due to the existence of the donor dipole in the vicinity. Consequently, the dipole of the nanoparticle

would interact with and additionally couple to the acceptor dipole, leading to the enhancement of the RET process. The authors concluded that the distance between the donor and the nanoparticle had a main influence on the energy transfer, in contrast to the main influence of the distance between the RET molecules in the absence of a dielectric nanoparticle. Gersten and Nitzan derived the expression for the interaction energy amplification factor ( $A(\omega)$ ) of the RET in a simplified geometry, when the nanoparticle (described by  $\epsilon(\omega)$ ) is between the RET pair, having the dipoles oriented along the symmetry axis [48]. In order to estimate the order of magnitude of the enhancement, the authors used the electrostatic approximation for a spherical nanoparticle of a diameter  $a$ , and the expression obtained was

$$A(\omega) = 1 + \frac{1}{2} \left( \frac{r_d + r_a}{a} \right)^3 \sum_{n=1}^{\infty} (-)^n (n+1)^2 \left( \frac{a^2}{r_d r_a} \right)^{n+2} \frac{\epsilon - 1}{\epsilon + (n+1)/n}, \quad (2.75)$$

where  $r_d$  and  $r_a$  are the distances between the donor and acceptor from the center of the nanoparticle.

Experimentally, the influence of metal nanoparticles on the manifestation of RET is often analysed in a sandwich set up. For example, Ozel *et al.* [146] deposited gold nanoparticles of 15 nm in diameter onto a glass substrate, followed by a deposition of a dielectric layer. In this way, the donor and acceptor layers with a dielectric layer between them was assembled. The authors analysed two cases when the lower layer was consisted of the donor quantum dots, and in the other case, of the acceptors. They found out that in both cases, the efficiency of RET was higher than in the control sample without the nanoparticle layer. Furthermore, in the situation when the acceptor layer was closer to the Au NPs, it exhibited stronger acceptor photoluminescence signal than in the case when donor was closer to the Au NPs. This implies that careful architecture of nanosystems can provide desired characteristics of a nanoplatform based on RET. Another example of "sandwich" experimental set up was done by Lunz *et al.* [147, 148], but with gold nanoparticle layer in between the layers of quantum dot pair suitable for RET. They reported that the RET rate increased 80 times in the presence of gold nanoparticle intermediate layer. The authors also analyzed concentration effects of the gold nanoparticles of 5.5

---

nm in diameter on RET between the donor and acceptor layers, with the separation distances of 3 nm and 12 nm, respectively. By following fluorescence signals from the pair while exciting donors, the authors found that although Au nanoparticles induce enhancement of the RET rates, the luminescence signal from acceptor was not as high. They assigned this effect to the quenching of the acceptor signal, even though the SPR peak of Au NPs is at 532 nm and the acceptor emission peak was at 623 nm. An another, very detailed, both theoretical and experimental study of a "sandwich" structured donor-gold NPs-acceptor system was done by Marocico [149]. Their results suggest that donor-Au NPs coupling is resulting in stronger dipole system that consequently leads toward increase of RET rate between the RET pairs.

Zhang *et al.* reported on the influence of silver nanoparticles on the RET between a fluorophore-pair [150, 151]. Their system consisted of oligonucleotides bounded with the dyes that are attached at two distances onto silver nanoparticles of three different diameters. The observed efficiency of RET due to the proximity of the silver nanoparticles increased with the increase of the nanoparticle diameter (15 nm, 40 nm, 80 nm). Also, in the case of a linker of 2 nm between the dyes-oligonucleotides system and the 15 nm nanoparticle, the RET efficiency was lower compared to the same system with the 10 nm linker. Another type of RET experiment is done by Reil *et al.* [152]. By means of lithography, the authors deposited gold islands (disks) on glass substrate in quadratic net organization, with 100 nm separation. The RET pair of fluorophores was introduced on the top of the nanostructured substrate. By varying the gold disks sizes, the SPR maxima were positioned between 560 nm to 680 nm. Fluorophores emission peaks were on the lower (donor) and higher (acceptor) end of the SPR interval. The authors concluded that the higher enhancement of RET was in the case when the SPR peak was positioned around the acceptor emission maximum, while the matching of the SPR peak with the donors emission would cause increase of donors radiative rate, effectively decreasing the available energy for RET process. Similar results were reported by Zhao *et al.* [153], in the case of the system with gold nanorods surrounded by a polymer layer with incorporated RET pair of fluorophores.

---

# Chapter 3

## Sample preparation, experimental techniques and methods

In this chapter, the materials and experimental procedures used in this thesis are presented and explained in detail. The first Section 3.1 describes the synthesis of bare gold nanoparticles and the procedures for their functionalization by amino acid tryptophan and vitamin B2 riboflavin. In the second part the experimental methods used for investigating morphology, optical properties and the electronic structure of the functionalized nanoparticles are presented. The preparation of the biological samples containing functionalized nanoparticles, along with the deep-ultraviolet (DUV) fluorescence microscopy used for their imaging, is given in the Section 3.3.

### 3.1 Sample preparation

#### 3.1.1 Synthesis of functionalized gold nanoparticles

##### Synthesis of bare-surface gold nanoparticles

Gold nanoparticles (Au NPs) were prepared by chemical synthesis procedure, which consisted of reduction of chloroaurate ions by a strong reducing agent. In a typical procedure, 25 mg of sodium borohydride ( $\text{NaBH}_4$ ) was added rapidly to 100 ml of 0.2 mM aqueous solution of gold (III) chloride trihydrate ( $\text{HAuCl}_4 \times 3\text{H}_2\text{O}$ ), under constant and vigorous stirring at room temperature. Formation of nanoparticles is

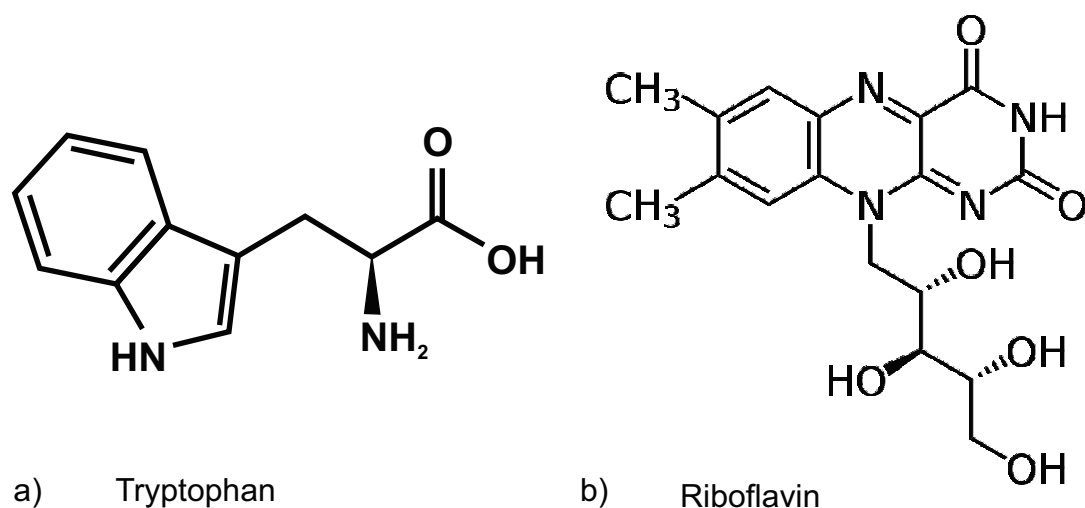


**Figure 3.1:** (a) Chemical structure of amino acid tryptophan (Trp); (b) chemical structure of vitamin B2 riboflavin (Rb)

manifested by a change in colour of the solution from initial yellow to dark red. The colloid was stirred for an additional hour upon reaction and subsequently aged for 24 hours at 4°C prior to use. If kept in the dark at 4°C, the Au NPs prepared in this way were chemically stable for months after the preparation.

Two biomolecules were used for functionalization of gold nanoparticles- amino acid tryptophan (Trp, Figure 3.1(a)) and vitamin B2 riboflavin (Rb, Figure 3.1(b)). Both molecules were purchased from Sigma Aldrich and used as received. For the functionalization procedure, batch aqueous solutions of the biomolecules were prepared of concentrations 10 mM for Trp and 0.25 mM in the case of Rb, using 4D ultrapure water.

### Functionalization of gold nanoparticles with one fluorophore

Functionalization of gold nanoparticles is done by slowly adding certain volume of the given solution to the gold hydrocolloid under constant stirring at room temperature. The list of samples used is presented in Table 3.1.

### Bifunctionalization of gold nanoparticles

For the preparation of bifunctionalized gold nanoparticles, mixtures of Trp and Rb solutions in appropriate ratios were added to the gold colloid. Additionally, to

**Table 3.1:** The list of single-functionalized Au NPs samples and their notation.

Sample notation	Volume (ml) AuNPs [0.2 mM]	Volume (ml) Trp [10 mM]	Volume (ml) Rb [0.25 mM]	Molar ratio
AuNPs	20	0	0	/
AuTrp1	20	0.4	0	1:1
AuTrp2	20	0.8	0	1:2
Au2Rb1	20	0	8	2:1

**Table 3.2:** The list of samples of bifunctionalized gold nanoparticles. Gold concentration was 0.2 mM.

Sample notation	Au (ml)	Trp (ml)	Rb (ml)	H <sub>2</sub> O (ml)
ATR025	5	0.2	1	3
ATR05	5	0.2	2	2
ATR075	5	0.2	3	1
ATR1	5	0.2	4	0
AT	5	0.2	0	4
AR1	5	0	4	0.2
A	5	0	0	4.2
TR025	0	0.2	1	8
TR05	0	0.2	2	7
TR075	0	0.2	3	6
TR1	0	0.2	4	5
T	0	0.2	0	9
R1	0	0	4	5.2
Ctr	0	0	0	9.2

ensure equal concentrations of all components, a certain volume of ultrapure water was added where necessary after the functionalization process. As in the case of single-functionalized Au NPs, the concentrations of batch solution of tryptophan and riboflavin were 10 mM and 0.25 mM, respectively. The gold to tryptophan molar ratios were kept at 1:2, whereas the gold to riboflavin ratio varied from 0.25 to 1 with steps of 0.25, as showed in Table 3.2. The notation of the samples was shortened for the sake of clarity.

### Purification of functionalized gold colloids

For the photoemission experiments and the bioimaging of human hepatocellular carcinoma-derived cell line incubated with bifunctionalized gold nanoparticles, the



colloidal samples underwent an additional centrifugation process. This was done in order to increase their concentration and to remove potentially unbound molecules from the colloids. The samples were centrifuged at 40 000 rpm ( $111\,000 \times g$ ) for 20 minutes at 4°C under low vacuum. Supernatants consisting of 80% of initial volume were disposed. The obtained pellets were afterwards submerged in ultrasound bath for 15 s prior to collection.

## **3.2 Characterization of functionalized gold nanoparticles**

### **3.2.1 Size and morphology of functionalized gold nanoparticles**

The size and morphology of functionalized gold nanoparticles was investigated by transmission electron microscopy (TEM) using a TECNAI F30 G2 Twin transmission electron microscope operating at 300 kV. The obtained resolution was 0.205 nm. The samples were deposited on carbon coated copper grids and dried at room temperature. The size distribution of the nanoparticles was determined by measuring diameters of circular areas of approximately 140 nanoparticles per sample.

### **3.2.2 Electronic structure characterization of functionalized gold nanoparticles**

#### **Raman spectroscopy**

Influence of gold nanoparticles on the vibrations of electron bonds of the molecules localized on the nanoparticles was investigated by Raman spectroscopy. Raman spectrometer equipped with RamanRxn1 Microprobe (Keiser optical systems inc.) uses Invictus laser of 785 nm as an excitation source with end power of 22.2 mW. The data was collected by using x10 objective in spectral coverage of 100-3425  $\text{cm}^{-1}$ . Sample preparation consisted of a deposition of certain amount of the colloids onto a flat aluminium foil and drying in ambient conditions. The acquisition was done

by measuring dark signal from the system and subsequently the signal coming from the sample. For every sample, ten acquisitions of 60 s were done and averaged automatically.

### **Photoelectron spectroscopy**

Influence of biomolecules attached to gold nanoparticles on valence electronic structure of both the molecules and gold were investigated by means of angle resolved photoelectron spectroscopy in the vacuum-ultraviolet domain of the photon energies. These measurements were done on an aerosol setup coupled to the electron/ion imaging coincidence spectrometer Delicious III located at the DESIRS beamline of the Synchrotron Soleil (France) (Figure 3.2) [154, 155, 156, 157]. The setup uses synchrotron radiation as a single photon ionization source. The radiation is tunable in energy interval 5-40 eV, monochromated by a 6.65 m normal monochromator and several gas filters (Xe, Ar or He). The analysed colloids were atomised by an atomiser (TSI, model 3076) connected to two silica-gel columns for drying by diffusion (TSI model 3062). Afterwards the aerosol is brought to an aerodynamic lens system, a part of the SAPHIRS molecular beam chamber. The formed aerosols passed through a 200  $\mu$ m limiting orifice that ensured 6 mbar of pressure in the ALS, which was used to focus the particles into a 420  $\mu$ m aerosol beam. The ALS was also used to transfer the particles into the ionization chamber, where it was crossed with a 100  $\mu$ m wide beam of synchrotron radiation. The atomized and dried colloids formed aerosol particles approximately 130 nm in size that, assuming fractal dimension of 1.7, contained 40 primary nanoparticles. In average, each second of the experiment there were 1.5 particles in the 420x100x100  $\mu$ m interaction region. Photo-created electrons and ions are collected by velocity map imaging (VMI) device located above the interaction area (detection of photoelectrons), coupled to the ion imaging time of flight mass spectrometer located below the interaction area (detection of photoions).

The functionalized gold colloids used for these analyses were all prepared and centrifuged as described in the previous section. Pellets of AuTrp, AuRb and ATR1 were used in non-diluted concentration, whereas Au NPs, Trp, Rb and TR solutions were used without the centrifugation step. Excitation energy of circularly polarized

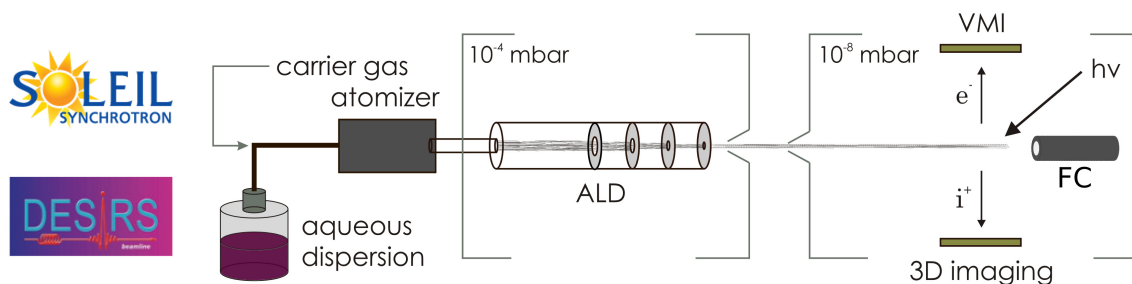


**Figure 3.2:** Experimental setup at the DESIRS beamline, synchrotron Soleil (France). The colloidal samples are atomized and carried via the aerodynamic lens (ALD) to the interaction region. Afterwards it enters the ionization chamber where it is exposed to photon beam. The photoelectrons and the corresponding ions are being collected by the velocity map imaging method (VMI).

synchrotron radiation was varied between 8-13.9 eV. Photoelectrons were detected by the velocity map imaging technique. The photoelectron images were inverted by using pBASEX algorithm [158]. In this way, dependence of the number of photoelectrons on their kinetic energy is obtained. The photoelectron spectra were afterwards corrected for the secondary electron contribution.

### 3.2.3 Optical properties of functionalized gold nanoparticles

#### UV-vis absorption spectroscopy

In order to confirm functionalization of the gold nanoparticles, as well as to access the optical properties of the hybrid nanostructures formed, the absorbance spectra of all samples were taken on a Thermo Evolution 600 spectrophotometer. Colloids were placed into quartz cuvette and absorbance spectra were taken in the range between 200 nm and 800 nm.

#### Photoluminescence spectroscopy

The photoluminescence spectra of the pure solutions of the biomolecules and the functionalized colloids were obtained by using PerkinElmer LS45 fluorescence spectrophotometer. The excitation and emission spectra were recorded for excitation range 270-290 nm, while the emission spectra were collected in range 300-500 nm (for excitation of 270 nm) or 320-600 nm (for excitation of 290 nm), unless otherwise stated.

### 3.3 Deep-UV fluorescence microscopy of biological samples incubated with functionalized gold nanoparticles

#### 3.3.1 Preparation of biological samples for deep UV imaging

Biological samples used for this research are Gram-negative bacteria *Escherichia coli*, fungus *Candida albicans*, as well as human hepatocellular carcinoma-derived Huh7.5.1 cells. All three strains were incubated with different colloids. Namely, the bacterial strain was incubated with tryptophan-functionalized gold nanoparticles; the fungus cell line was incubated with riboflavin-functionalized gold nanoparticles; and hepatocellular carcinoma cells were incubated with bifunctionalized gold nanoparticles.

##### **Bacterial strain *Escherichia coli* incubated with tryptophan-functionalized gold nanoparticles**

The microbial culture of *Escherichia coli* (ATCC25922) was purified by standard centrifugation procedure. Volume of 100  $\mu\text{l}$  of bacterial dispersion was incubated with 400  $\mu\text{l}$  of colloid samples AuTrp1 and AuTrp2 (Table 3.1), with the two control samples of bare gold nanoparticles and saline solution. The incubation time was 2 hours at 37°C. After the incubation, the dispersions were again centrifuged. Thus pelleted cells were deposited on quartz coverslips and left to dry on room temperature.

##### **Fungus strain *Candida albicans* incubated with riboflavin-functionalized gold nanoparticles**

Procedure for preparation of *Candida albicans* strain incubated with colloid Au2Rb (Table 3.1) was similar to previously described for *E. coli*. Volume of 100  $\mu\text{l}$  of the fungus dispersion was incubated with 400  $\mu\text{l}$  of Au2Rb of two concentrations. Sample noted as Au2Rb C<sub>1</sub> was firstly diluted with saline to its half concentration, whereas the second sample noted as Au2Rb C<sub>2</sub> was the colloid of the initial concentration. As

in the case of *E.coli*, the incubation was for 2 hours at 37°C. Upon the depositions of the biological dispersions on the coverslips, the fungi were fixated by adding 20  $\mu$ l of glytaraldehyde on the top of the dispersion and then left to dry in ambient conditions. Prior to imaging, the coverslips were promptly rinsed with high purity water and left to dry.

### **Human hepatocellular carcinoma-derived Huh7.5.1 incubated with bifunctionalized gold nanoparticles**

Human hepatocellular carcinoma-derived Huh7.5.1 cells were routinely cultured as monolayer and were grown in Dulbeccos modified Eagles medium (DMEM) supplemented with 10% fetal calf serum, penicillin and streptomycin. The cells were maintained in the calf fetal serum at 37°C in a humidified atmosphere and of 5% CO<sub>2</sub>. For deep-UV fluorescence imaging studies, the Huh7.5.1 cells were plated in plastic Petri dishes containing 25 mm round quartz coverslip and incubated for 24 hours, leading to deposition of 240 000 cells in each well with quartz slide. Cell attachment was monitored by visible inspection using an optical microscope. Thereafter, the cells were incubated with purified bifunctionalized colloid samples of 10  $\mu$ M final concentration, as the volume 55  $\mu$ l of the samples were added into 3 ml of the medium. In order to obtain the same concentration as compared to the previous samples, 150  $\mu$ l of the bare gold nanoparticle colloid AuNPs were added to 3 ml of medium. The cells were afterwards incubated with colloid samples for 6 h. Subsequently they were washed 2 times with PBS and then fixed for 1 h with 4% PFA at 4°C. After fixation, the cells were washed 2 times with distilled water and dried in air.

### **3.3.2 Deep-UV fluorescence microscopy**

Biological samples incubated with the nanostructures were carried out on a Zeiss Axiobserver Z-1 microscope Telemos at the DISCO beamline of the synchrotron Soleil (France) [159, 160, 161]. Telemos is in epifluorescence mode, equipped with Zeiss Ultrafluar objective x40 and x100 with a 1.2 numerical aperture that requires glycerine immersion (Figure 3.3). The microscope uses monochromatic synchrotron

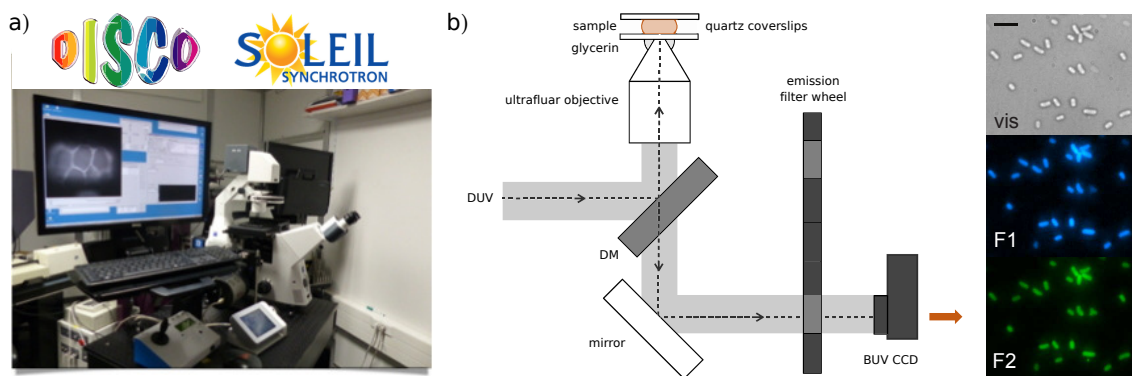


**Figure 3.3:** a) Fluorescence microscope Telemos at DISCO beamline, synchrotron Soleil (France). b) Schematic representation of Telemos microscope at beamline DISCO, synchrotron Soleil. Monochromatic synchrotron radiation in deep-ultraviolet domain (DUV) is being reflected from dichroic mirror (DM) after which is directed toward the glycerine ultrafluor objective. The fluorescence signal coming from the irradiated sample goes back through the objective and the dichroic mirror. After the reflection of a mirror at bottom, it passes through a preselected filter positioned in the filter wheel and is collected onto back-illuminated charge-coupled device (BUV CCD). On the right part, a typical visible image of a bacterial sample is shown, along with fluorescence images taken through two different filters. Adapted from [163].

radiation as an excitation source in the deep-ultraviolet range of 250-350 nm. Fluorescence signals from the samples deposited on quartz coverslips were collected through set of appropriate filters by PIXIS 1024 BUV camera (Princeton, USA). The whole setup is controlled under  $\mu$ Manager [162]. Depending on the objective used, final resolution of acquired microscopic images were 277 nm (for x40 objective) and 154 nm (for x100 objective).

Acquisition conditions were optimized for a given system under investigation, and they are listed in Table 3.3. Two types of measurements were taken: 1) steady state measurements were comprised of preselecting several locations across the coverslip, and launching acquisition of fluorescence images prior to taking a visible image of the location and 2) the time-lapse experiments, which were done on one representative area of the coverslip, that comprised acquiring fifteen consecutive fluorescence image pairs. Overall acquisition time in the time-lapse experiments was 15 min with a constant exposure of the sample to the excitation beam. The images were analysed using FIJI [164] or Matlab software.

**Table 3.3:** The list of experimental conditions used in DUV fluorescence microscopy

Biological Sample	Nanostructures	Excitation wavelength	Filter 1 (nm)	Filter 2 (nm)	Acquisition time per image (min)	Objective	Steady state	Timelapse
<i>E. coli</i>	Au-Trp	280	327-353	452-486	6	X100	yes	no
<i>C. albicans</i>	Au-Rb	290	535-607	/	1	X100	yes	no
<i>C. albicans</i>	Au-Rb	350	535-607	/	1	X100	yes	no
Huh7.5.1	ATR	290	355-405	510-560	0.5	X40	yes	yes

---

## Chapter 4

# Physical characterization of functionalized gold nanoparticles

This chapter concerns the analyses of three systems of functionalized gold nanoparticles: tryptophan-functionalized Au NPs, riboflavin-functionalized Au NPs and tryptophan/riboflavin-bifunctionalized Au NPs. First, we will discuss the morphology of the samples studied by transmission electron microscopy. After that, we will focus on the results of Raman spectroscopy in order to elucidate the nature of the interaction of tryptophan and/or riboflavin with gold nanoparticles. The effects of their mutual interaction on the valence electronic structure will be analysed by means of vacuum-ultraviolet photoelectron spectroscopy. The last chapter deals with the optical properties of the functionalized nanostructures. Functionalization process will be studied by absorbance spectroscopy *via* changes in the positions of surface plasmon resonance of the Au NPs. In addition, the stability of the fabricated nanostructures will be confirmed by the same method. The last part is devoted to the investigation of the fluorescent properties of the biomolecules attached to the gold nanoparticles. Special emphasis will be put on the analysis of non-radiative resonant energy transfer between the biomolecules mixed in a solution and when they are both attached to the Au NPs.



## 4.1 Size and morphology of functionalized gold nanoparticles

By introducing new entities, the metal colloids might become unstable and a coalescence process might be triggered. We tested the stability of newly formed functionalized colloids by means of transmission electron microscopy. The bare gold NPs synthesis procedure, commonly used in our group, results in nearly spherical gold nanoparticles of diameter  $7.9 \pm 1.6$  nm [165]. TEM images of gold nanoparticles functionalized with tryptophan (AuTrp), riboflavin (AuRb) and with both tryptophan and riboflavin (ATR1) are shown in Figure 4.1. The calculated mean nanoparticle diameters were  $8.0 \pm 1.4$  nm,  $7.7 \pm 1.0$  nm and  $7.5 \pm 1.1$  nm for AuTrp, AuRb and ATR samples, respectively. The size distribution follows the log-normal dependence and the fit parameters obtained for the each distribution are specified in the right upper corner of the figures. The TEM analyses indicate that functionalization process does not significantly affect the size and morphology of gold nanoparticles.

## 4.2 Characterization of the electronic structure of functionalized gold nanoparticles

In this section, we report on the nature of the interaction of the biomolecules with gold nanoparticles. Changes in the vibrational spectra of the fluorophores in the presence of metal surface are probed by means of Raman spectroscopy. It is well known that metal can amplify the vibrational signal coming from natural vibrational modes of the molecules, which is the basis of surface-enhanced Raman spectroscopy (SERS) [40]. The SERS is the result of the enhanced radiation field intensity in the vicinity of metal nanoparticles that takes place when the incident radiation has the wavelength that corresponds to the resonant frequency of the surface plasmon oscillations of the metal. This produces a stronger excitation of the vibrational modes of the adsorbed molecules. However, the excitation wavelength used in this particular study is far from the position of surface plasmon resonance of the investigated

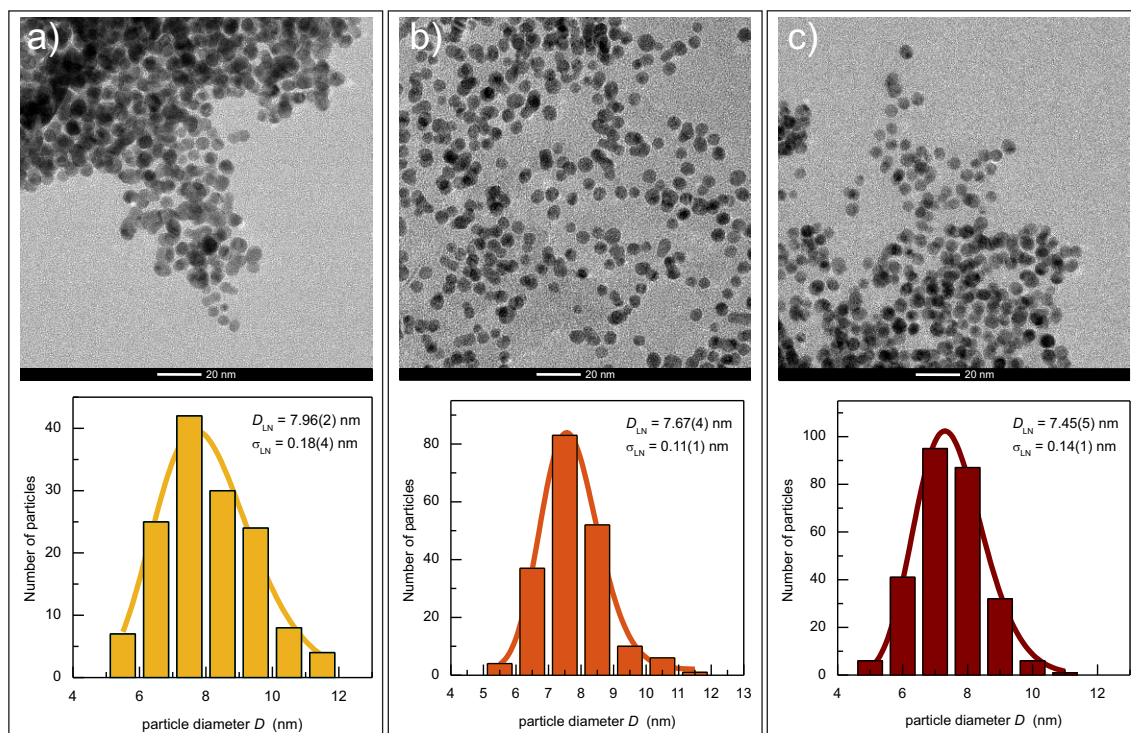


**Figure 4.1:** TEM micrographs of (a) AuTrp, (b) AuRb and (c) ATR1, and their size distributions fitted to log-normal distribution with parameters  $D_{LN}$  (mode) and  $\sigma_{LN}$  (standard deviation).

Au NPs (780 nm vs 520 nm). Therefore, the difference in the Raman spectra of the biomolecular samples and the functionalized gold nanoparticle samples is the consequence of the influence of the metal surface onto vibrations of particular functional groups of the biomolecules. By following the changes in the Raman spectra, the geometry of the constituents of the analysed nanosystems can be elucidated.

On the other hand, photoelectron spectroscopy gives insight into changes of valence electron levels of the metal, as well as into changes in highest-occupied and lowest-unoccupied energy levels of the adsorbed molecules. A particular significance of this study lies in fact that these experiments were done in gas phase, meaning the nanosystems were free from influence of the otherwise-necessary supporting substrates.

### 4.2.1 Raman spectroscopy

Vibrational normal modes of biomolecules were analysed by Raman spectroscopy detailed in Chapter 3. Raman spectra of the three nanosystems - AuTrp, AuRb and

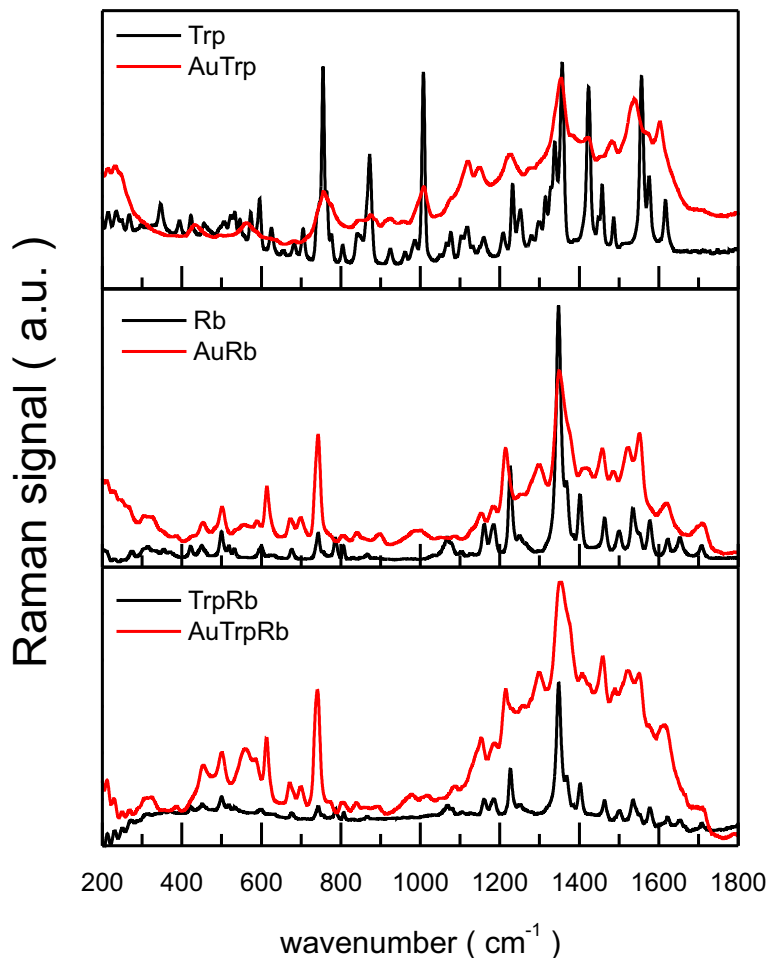


**Figure 4.2:** Raman spectra of gold nanoparticles functionalized by tryptophan (the upper graph), by riboflavin (the middle graph), and by both tryptophan and riboflavin (the lower graph), with the spectra of the corresponding biomolecules. The samples were dried prior to the spectroscopic measurement.

AuTrpRb - are shown in Figure 4.2, as well as the spectra of solutions of tryptophan, riboflavin and their mixture.

The Raman spectra reveal that the presence of gold nanoparticles influences the signal of pure molecules. The vibrational modes of all three samples are given in Tables 4.1, 4.2 and 4.3. The observed modes are compared with the spectra reported in the literature [83, 166, 167, 168, 169, 170]. The vibrational peaks are assigned to particular modes, which is stated in the last column in each of the tables.

### **Tryptophan-functionalized gold nanoparticles**

The comparison of the Raman spectra of AuTrp sample and the spectra of the pure tryptophan sample shows that the functionalization induces a broadening of the peaks which results in the less resolved structure. This might be due to slightly higher intensity of Trp Raman peaks when the molecule is attached to Au NPs (approximately 82000, background included) than when it is recorded in the free state (60000, background included). However, the spectrum is consistent with the study of Hussain *et al.* where the authors used a similar procedure for synthesis of tryptophan modified gold nanoparticles [83].

Several peaks are particularly remarkable in the AuTrp spectrum. The peak at  $1604\text{ cm}^{-1}$ , which originates from the stretching of the benzene ring, is shifted by  $13\text{ cm}^{-1}$  to lower wavenumbers compared to the position of the corresponding Trp peak. The Raman line at  $1540\text{ cm}^{-1}$  peak, assigned to stretching of indole group (benzene + pyrrole rings), is shifted by  $15\text{ cm}^{-1}$  to lower wavenumbers compared to the position of the same line in the Trp spectrum. The intensities of the peaks at  $1354\text{ cm}^{-1}$  and at  $1227\text{ cm}^{-1}$  are not significantly affected by functionalization but they are also shifted to lower wavenumbers due to the bending of hydrogen atoms on indole [166]. Also, two neighbouring peaks at  $1148$  and  $1112\text{ cm}^{-1}$  are stronger in the spectrum of the AuTrp sample than in the spectrum of the pure Trp sample. They originate from the in-plane deformations of the benzene ring and the bending of C-H bonds, respectively. On the low-wavenumber part of the spectrum, the structure is less resolved. It can be seen that the peak located at  $755\text{ cm}^{-1}$  in the spectrum of the pure tryptophan, assigned to out-of-plane bending of indole, is very weak in the case of the spectrum of AuTrp sample. This Raman study supports the findings of Hussain *et al.* [83], where it was suggested that the indole group is parallel to the surface of the gold nanoparticle. This orientation is also consistent with our previous FTIR study of the AuTrp system [165].

### **Riboflavin-functionalized gold nanoparticles**

Analyses of the Raman spectra of the AuRb and Rb samples revealed that gold NPs affect also the peaks of the Rb biomolecule attached to its surface. This effect is,

**Table 4.1:** Observed values of Raman modes of pure tryptophan sample and tryptophan-functionalized gold nanoparticles and their most probable assignment<sup>(a)</sup>.

Trp	AuTrp	Ref. [83]	Ref. [169]	Ref. [166]	Assignment
1617 m	1604 m	1627	1622		$\nu$ CO <sub>2</sub> , $\nu$ CC(R), $\beta$ (NH <sub>3</sub> <sup>+</sup> )
1575 m	1566 sh	1582	1581	1591s	$\beta$ (NH <sub>3</sub> <sup>+</sup> )
1556 s	1540 s	1555	1561	1537 sh	$\nu$ (R, r)
1486 w	1482 m	1477	1492	1487 w	ip- $\nu$ (R, r)
1457 m	1458 vw	1464	1455	1458 s	$\beta$ CH <sub>2</sub> , $\beta$ (NH <sub>3</sub> <sup>+</sup> )
1423 s	1420 w	1410	1429	1415 s	$\beta$ (NH <sub>3</sub> <sup>+</sup> ), in-def(r, R)
1357 s	1354 s	1359		1357 s	$\beta$ CH <sub>2</sub> , $\beta$ CH
1338 m		1344	1333	1337 sh	$\beta$ CH, $\beta$ CH <sub>2</sub>
1315 w			1320	1316 m	$\beta$ H(C), $\beta$ CH <sub>2</sub>
1299 vw			1289	1294 vw	def (R, r)
1252 w	1278 vw	1249	1254	1251 w	def H(R, r)
1232 m	1227 m		1238	1231 m	$\beta$ CH, $\beta$ H(R, r)
1208 w		1206	1213	1207 m	$\nu$ C-COO <sup>-</sup> , ip-def(r)
1159 w	1148 m	1159	1154	1158 m	ip-def (R), $\beta$ CH + CH <sub>2</sub>
1118 w	1120 m	1123	1121	1116 vw	$\beta$ CH, $\beta$ NH <sub>3</sub> <sup>+</sup> , ip-def(R)
1076 w	1076 sh	1084	1078	1077 m	ip- $\beta$ CH + NH(r)
1008 s	1009 m	1000	1010	1008 m	$\beta$ (R)
987 w			990	988 m	$\beta$ CH, $\nu$ CN
961 vw	956 vw		965	964 vw	$\beta$ H(R)
924 w	923 vw	924	930	926 m	$\beta$ CH <sub>2</sub> , $\beta$ NH <sub>3</sub> <sup>+</sup>
872 s	876 w	870	875	865 s	ip-def (R,r)
841 w			840		$\beta$ NH <sub>3</sub> <sup>+</sup> , $\beta$ H(r)
804 w			803	803 m	$\beta$ CH <sub>2</sub> , $\nu$ C-COO <sup>-</sup>
776 w			779	778 vw	$\nu$ C-CH <sub>3</sub> , $\nu$ CC(r)
764 sh			766	764 sh	def(R, r), $\beta$ CO <sub>2</sub> <sup>-</sup>
755 s	757 m	749	755	760 s	$\nu$ (R, r), op-def(R,r)
705 w			706	707 vw	op-def (R, r)
684 vw	683 vw		684	683 m	$\nu$ (R, r)
625 w			627	627	def r
596 m		583	596	596 sh	$\beta$ NH(r), def (R, r)
573 w	562 w	572	574	581 m	op-def(R. r)
547 vw		545	548	549 m	ip-def (R, r)
533 vw			529	528 s	ip-def(R, r)
455 vw		443	456	456 m	ip-def (R, r), $\beta$ CN
423 w	432 w	424	426	426 s	op-def(R. r)

<sup>(a)</sup> abbreviations: s strong, m medium, w weak, vw very weak, sh shoulder;  $\nu$  stretching,  $\beta$  bending; R benzene ring, r pyrrole ring, ip-def in-plane deformation, op-def out-of-plane deformation;

however, less pronounced than in the case of AuTrp interaction. Raman spectrum of the AuRb sample has more resolved structure than that of the AuTrp sample. In order to describe the AuRb interaction, a schematic of Rb molecule with labelled characteristic groups is presented in Figure 4.3. In the AuRb spectrum, the strongest peaks emerge at  $1551\text{ cm}^{-1}$ , corresponding to the stretching of the C2=O groups and the in-plane bending of R3 ring of Rb. The  $1521\text{ cm}^{-1}$  band, which is shifted to low-wavenumber part of the spectrum by  $14\text{ cm}^{-1}$  with respect to its position in the spectrum of the Rb sample, is assigned to the double bonds between nitrogen and carbon atoms in R2 and R3 rings. The Raman peak in the AuRb spectrum at  $1458\text{ cm}^{-1}$ , assigned to the stretching of carbon atoms in R1 ring, corresponds to the peak in the spectrum of pure riboflavin located at  $1464\text{ cm}^{-1}$ . The peak at  $1350\text{ cm}^{-1}$ , which also originates from the stretching of carbon atoms bonds, is located at the almost same position in both AuRb and Rb spectra. All previously mentioned peaks are more pronounced in the spectrum of AuRb sample than in the spectrum of the Rb sample. Further analysis shows that there is a slight difference for the peak at  $1299\text{ cm}^{-1}$ , which is more prominent in the spectrum of the AuRb sample than in the spectrum of the Rb sample, and is coming from double bond between oxygen and carbon atoms in R3 ring. Next to this peak in the spectrum of the AuRb sample, there is a peak at  $1215\text{ cm}^{-1}$ , which is shifted toward lower wavenumbers by  $11\text{ cm}^{-1}$  compared to the spectrum of the Rb sample. This peak is assigned to the bending of the all three rings, noted as Flav in the Table 4.2. The lower part of the Raman spectrum of the AuRb sample shows little dissimilarity from the spectrum of pure riboflavin solution. The peak located at  $897\text{ cm}^{-1}$  is visible in the spectrum of the AuRb sample, but it cannot be resolved in the Rb spectrum. Also, the peak at  $840\text{ cm}^{-1}$  is by  $26\text{ cm}^{-1}$  lowered in the spectrum of the AuRb sample as compared to the spectrum of the Rb sample. Both of them are assigned to R1 ring, as the first peak comes from vibrations of single bonds between carbon atoms in benzene ring, and the second one specifically comes from C8-H and C11-H, both in R1 ring. Furthermore, the peak at  $743\text{ cm}^{-1}$  is strong in the AuRb spectrum and weak in the Rb spectrum. This vibrational mode is assigned to the in-plane bending of bond of nitrogen atom N3 with hydrogen atom (Figure 4.3). In the spectrum of the AuRb

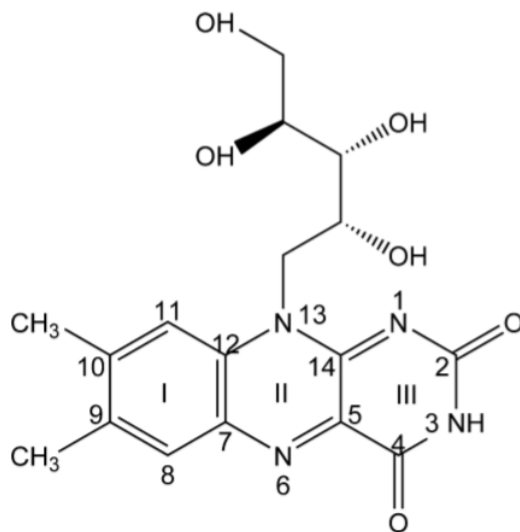


**Figure 4.3:** Riboflavin structure with atom numbering corresponding to the Table 4.2 in assignments of Raman modes.

sample, there is another distinctive peak located at  $614\text{ cm}^{-1}$ , which possibly comes from the bending of 3-single-carbon bonds. Also, there is a skught change in the peak around  $699\text{ cm}^{-1}$  in the AuRb spectrum, originating from in-plane bending of Flav part of the molecule, with respect to the peak in the Rb spectrum. Additionally, the peak around  $420\text{ cm}^{-1}$  coming from out-of-the-plane deformations of Flav part of Rb molecule, appears in the Rb Raman spectrum and not in the spectrum of the AuRb sample. The obtained results are in fair agreement with the study by Dendisova-Vyskovska *et al.* [167], where it was found that riboflavin molecules are interacting with gold surfaces *via* R1 part of the molecule.

### Bifunctionalized gold nanoparticles

Raman spectrum of tryptophan/riboflavin-bifunctionalized gold nanoparticles resembles the spectrum of the AuRb sample rather than that of the AuTrp sample. Below  $1000\text{ cm}^{-1}$ , the spectrum of the ATR sample has almost identical features as the spectrum of the AuRb sample. The difference concerns the bands located at  $584$  and  $560\text{ cm}^{-1}$ , which are assigned to tryptophan out-of-the-plane deformations (even though they were less pronounced in the AuTrp Raman spectrum). The peak located at  $453\text{ cm}^{-1}$  in the spectrum of the ATR sample is stronger than the same peak in the TR spectrum, probably due to the metallic influence on the out-of-

**Table 4.2:** Observed values of Raman modes of riboflavin solution and riboflavin-functionalized gold nanoparticles and their most probable assignment<sup>(a)</sup>. Raman modes from [167] are in format: [ in situ / ex situ ].

Rb	AuRb	Ref. [166]	Ref. [167]	Ref. [168]	Assignment
1707 w	1710 w				
1653 w		1650 s			$\beta$ R3
1622 w	1620 w	1622 m	1612/1618	1620 w	$\nu$ (R1), $\nu$ C2=O, ip $\beta$ R3
1577 m		1582 s		1576 m	$\nu$ (R2)
1551 sh	1551 m	1549 s	1564		$\nu$ C2=O, ip $\beta$ R3
1535 m	1521 m		1356/1537	1534 m	$\nu$ C=N(R2,R3)
1500 w	1484 vw	1505 m	1499/1505	1496 w	$\beta$ CH <sub>3</sub> , ip $\beta$ R3 N3-H,
1464 w	1458 m	1458 m	1456/1460		$\nu$ (C8-C9, C10-C11, C11-C12), $\beta$ (as) CH <sub>3</sub>
	1415 vw				$\beta$ (s) CH <sub>3</sub>
1402 m		1399 m	1400/1406	1398 m	$\beta$ (N1-C2, C7-C8,C10-C11, C7-C12)
1368 sh		1369 w	1356		$\beta$ Rib
1348 s	1350 s	1347 m	1346/1348	1344 s	$\beta$ (C10-C9, C12-C7), $\nu$ (C14-N13, C7-C12), $\beta$ R2, $\beta$ R3
1298 vw	1299 w	1306 w	1302	1287 vw	$\beta$ C=O (R3)
1249 w	1254 vw	1239 m	1263		$\beta$ C-H-O-H (Rib)
1226 m	1215 m	1211 sh	1228/1227	1222 s	$\beta$ Flav
1185 m	1184 vw	1180 m		1178 s	$\nu$ (C4-N3, CO-CH <sub>3</sub> ), $\beta$ C-H, $\beta$ O-H
1161 m	1154 vw	1155 w	1155/1157	1153 m	$\nu$ R3, ip $\beta$ R2, R3
1077 sh		1079 s	1086/1081	1094 vw	$\nu$ (C2-N3, C5-C4, C5-C14)
1067 w		1061 sh		1058 w	$\beta$ Flav, $\nu$ R3
	897 vw	896 sh			$\beta$ CCC
866 wv	840 vw	850 m		842 vw	$\beta$ (C8-H, C11-H)
807 w	805 vw	808 m	804	804 vw	ip-def C-N-C (Flav)
786 w		784 sh		784 m	
743 w	743 s	747 w	742/740	740 s	Ring breathing, $\beta$ N - Flav
	699 vw		705		ip $\beta$ Flav
676 vw	673 vw	674 sh		672 m	$\beta$ R2
620 vw	614 w	611 sh			$\beta$ C-C-C, $\beta$ CO
600 w		596 m		595 m	ip-def C-N-C (Flav)
500 w	501 w	501 m		500 w	op-def Flav
450 w	452 vw	450 s		443 vw	op-def Flav
422 vw		425 w			op-def Flav

<sup>(a)</sup> abbreviations: s strong, m medium, w weak, vw very weak, sh shoulder;  $\nu$  stretching,  $\beta$  bending; R benzene ring, r pyrrole ring, ip-def in-plane deformation, op-def out-of-plane deformation; Numbering of atoms [168]: R1 stands for ring I, R2 for ring II, and R3 for ring III, as shown on Figure 4.3; Rib - ribose chain in Rb, Flav - flavin part in Rb;



the-plane deformations of pyrrole, R2 and R3 rings. At higher wavenumbers, it is noticeable that a rather strong peak at  $1108\text{ cm}^{-1}$  in the Raman spectra of both pure Trp and AuTrp samples is absent in the spectrum of the AuTrpRb sample. The peak is assigned to the stretching of the benzene ring of tryptophan. The fact we did not observe the Raman normal modes, which correspond to zwitterionic Trp molecule ( $1487, 1666, 1591, 1415\text{ cm}^{-1}$  [166]), suggests that the tryptophan in bi-functionalized nanoparticles is in its acidic and/or basic state. The presented results reveal that Trp and Rb are not significantly changed when they were attached to the gold nanoparticles. They do not produce new adducts [166], and both of them obviously interact with Au NPs.

### **4.2.2 Photoelectron spectroscopy of free-standing functionalized gold nanoparticles**

Photoelectron spectroscopy that employs vacuum-ultraviolet photoexcitation is an important method for studying the valence electronic structure of solid materials. Being a surface technique, the photoelectron spectroscopy is very sensitive to the presence of molecules adsorbed on the materials surface, as well as on their conformation. In this subsection, we will present our results on the vacuum-ultraviolet photoelectron spectroscopy (VUV PES) investigation of functionalized gold nanoparticles. As intermediates between molecules and macroscopic matter, nanometer-sized objects exhibit specific and size-dependent properties. The photoemission characteristics of noble metal nanoparticles are characterized by a size-dependent photoelectron yield and work function [171, 172, 173]. In addition, due to a large surface-to-volume ratio, there is the pronounced contribution of the electrons from the surface atoms to the photoemission spectra of the nanoparticles. On the other hand, due to their reduced size, it is very difficult to manipulate a nanostructured object. Therefore, the VUV PES results on nanostructures obtained by conventional experimental setups depend on the nature of the substrates they are deposited on. For that reason, we tried to perform our experiments on the isolated nanosystems, by transferring the nanoparticles directly from the colloids to the interaction chamber using an aero-

**Table 4.3:** Observed values of Raman modes of bifunctionalized gold nanoparticles and solution of TrpRb and their most probable assignment. The abbreviation is the same as in Table 4.2.

TrpRb	AuTrpRb	TrpRb Ref. [166]	Trp Ref. [169]	Rb Ref. [168]	Assignment
1709 w	1710 vw	1711 s			$\nu$ CO, $\beta$ R3
1654 w		1650			$\beta$ R3, $\nu$ C2-O
1622 w	1610 w	1623 vw	1622		$\nu$ R, $\nu$ CC (R1)
1577 m	1573 w	1582	1581	1576 m	$\nu$ R2, $\nu$ CC, $\nu$ CN
1553 sh	1550 m	1549	1561		$\nu$ C2=O, ip $\beta$ R3, $\nu$ CC, $\nu$ CN
1535 m	1524 m			1534 m	$\nu$ C=N(R1,R2)
1500 w	1489 w	1505	1492	1496 w	$\beta$ CH <sub>3</sub> (Rb), ip $\beta$ R3 N3-H
1464 m	1459 m	1458	1463	1461 m	$\nu$ (C8-C9, C10-C11, C11-C12), $\beta$ (as) CH <sub>3</sub> (Rb), $\beta$ CH <sub>2</sub> (Trp), $\nu$ CC (R, R1)
1402 m	1407 w	1392		1398 m	$\nu$ CN(R3)
1368 sh		1360	1364		$\nu$ CC, $\nu$ CN
1348 s	1354 s	1339	1344	1344 s	$\beta$ CH <sub>2</sub>
	1298 m			1287 vw	$\nu$ CC(R)
1250 vw	1260 vw	1278	1254		$\nu$ CC(R3), $\nu$ CC(r), $\nu$ CN
1227 m		1244		1222 s	$\nu$ CC(r), $\nu$ CN, $\beta$ Flav
	1215 m	1218	1213		$\nu$ CC(R3), $\nu$ CC(r), $\nu$ CN
1185 m	1185 w	1199 s		1178 s	$\nu$ (C4-N3, CO-CH <sub>3</sub> ) (Rb), $\beta$ C- H, $\beta$ O-H (Rb)
1160 m	1154 m	1143	1164	1153 m	$\nu$ R3, ip $\beta$ R2, R3, ip-def(R), $\beta$ CH + CH <sub>2</sub> (Trp)
1079 w		1082 m	1078	1094 vw	ip- $\beta$ CH + NH(r), $\nu$ (C2-N3, C5- C4, C5-C14)(Rb)
1068 w		1054 m	1069	1058 w	$\nu$ CC(R3), $\beta$ R
	1018 vw		1010		$\nu$ (R)
	978 vw	967	965		$\beta$ CCC(R3,R,r)
866 vw			866		$\beta$ CCC(R,r)
	840 vw		840	842 vw	$\beta$ C8-H, C11-H (Rb)
807 w	805 vw	820 m	803	804 vw	
786 w	772 vw	782 s	779	784 m	op-def CH(r)
744 w	741 s		744	740 s	$\nu$ CC(R)
	700 w	697 m	706		ip $\beta$ Flav
676 w	671 w		684	672 m	$\beta$ R2
600 vw	613 m	599 m	596	595 m	$\beta$ (r), $\beta$ NCC(Flav)
	584 w		581		op-def(R, r)
	560 m	551 m			op-def R, $\beta$ CCN <sub>trp</sub>
533 vw			529		ip-def(R, r)
518 vw				519 m	$\beta$ C-C=O (Rb)
500 w	500 m	503 m	509	500 w	op-def r,R3, R2
451w	453 m		456	443 vw	op-def r,R3, R2
423 w		425 w	426	406 vw	
371 vw	385 vw	387 s			op-def NH, def Trp

dynamic lens system. To our best knowledge, these are pioneering measurements on free-standing functionalized nanoparticles with controlled surface chemistry. The chemical procedure for preparation of bare and functionalized gold nanoparticles are described in detail in Section 3.1, while a thorough description of the experimental setup is given in Section 3.2. Briefly, synthesized and purified hydrocolloids of Au, AuTrp, AuRb and ATR1 nanoparticles were introduced into a constant output atomizer connected to a diffusion dryer. Afterwards the aerosol is brought to an aerodynamic lens system that led the nanoparticles to the ionization chamber. The photoelectrons, created due to the exposure of the aerosol to the synchrotron radiation, were collected by velocity map imaging (VMI) spectrometer located above the interaction volume.

The photoemission of electrons from macroscopic solid materials can be the most intuitively explained using a three-step model by Berglund and Spicer [174]. More specifically, an optically excited electron goes into a state of higher energy (photoexcitation, step I), after which it traverses a path toward the surface of the solid in which it may scatter elastically or inelastically (transport, step II). Finally, the photoelectron escapes into vacuum if conditions of momentum conservation are satisfied (escape, step III). These processes are mainly determined by the type material, i.e. the density of valence states and the electron mean free path. However, the geometry of the material also plays an important role in the cases when the diameter of the solid particle is comparable to the mean free path or the photon absorption length. The size and the curvature of the metal nanoparticles can significantly influence the kinetic energy distribution of the photoelectrons. In our experimental conditions, all mentioned characteristic dimensions are comparable and below 50 nm over the investigated energy range, thus the size effects on the photoemission spectra are non-negligible. However, since the size-effects mostly influence the transport process (step II), we will avoid a detailed analysis of the influence of nanoparticle size and focus on the valence band structure of the functionalized nanoparticles. On the other hand, it is shown that Fermi level of metal nanoparticles depends on their size, surrounding and the passivant [38]. Tanaka *et al.* found that as the diameter of the nanoparticles decreases, the Fermi level increases. Also, due to their low coordina-

tion number, the surface atoms in gold nanoparticles induce a shift of  $5d$  orbitals toward lower binding energies [61, 62, 63]. Adsorbance of organic molecules on metal nanoparticles can influence the metals highest electron levels. Conversely, the existence of metal nanoparticles affects the highest-occupied and lowest-unoccupied energy levels of the adsorbed molecules.

Initial assessment of the electron band structure of isolated gold nanoparticles by VUV photoemission spectroscopy was performed by running a photon energy scan between 6 and 12 eV, while recording the kinetic energy distribution of the photoelectrons by the VMI detector. The photoelectron spectra of bare gold nanoparticles for photon energies 7.5, 8.0, 8.5 and 9.0 eV are presented in the Figure 4.4(a), while the number of threshold photoelectrons as a function of the photon energy of the synchrotron radiation is presented in Figure 4.4(b). The photoemission spectra of isolated gold nanoparticles obtained for photon energies 7.5 - 9 eV start at  $5.56 \pm 0.08$  eV binding energy (BE). Since, in our case, the BE is measured from to the vacuum level, the onset represents the work function ( $W_f$ ) of the nanosystem. The  $W_f$  values for thin films of polycrystalline gold are typically in the 4.4 - 4.7 eV range for the films exposed to ambient atmosphere, about 5.0 - 5.1 eV when atomically clean and ordered under ultra-high vacuum conditions, and up to 5.3 - 5.4 eV when sputter-cleaned by argon-ion bombardment [175]. The higher  $W_f$  obtained here is very close to the value obtained by free electron model and it can be attributed to the non-negligible charging effect on the  $W_f$  in the case of nanometer sized metallic particles [171, 173]. Note that in our experiments, the binding energy is measured with respect to the vacuum. We calibrated the energy scale by using the BE of Ar  $3p_{3/2}$  level at 15.76 eV instead of Fermi level of the metal, which is commonly used as a reference in the photoemission studies of solid surfaces. Nevertheless, for comparison with the available data, we assigned the midpoint value of the photoemission edge at  $6.32 \pm 0.08$  eV as the Fermi level ( $E_F$ ).

The threshold photoemission spectrum (TPES) of isolated gold nanoparticles recorded by changing the photon energies between 6 and 12 eV and integrating the count of photoelectrons with the kinetic energies in the 0 - 150 meV range is given in Figure 4.4(b). The spectrum shows photoemission shoulder at lower energies, as

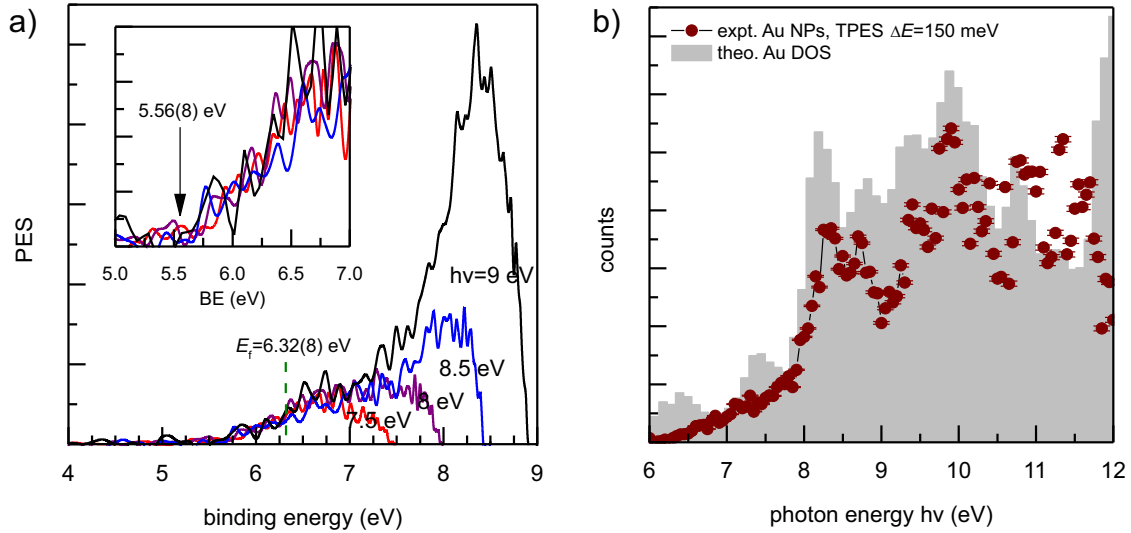


**Figure 4.4:** (a) Photoemission spectra of isolated gold nanoparticles obtained for photon energies 7.5 - 9 eV. (b) TPES of isolated gold nanoparticles (circles) and theoretical density of states histogram from Ref. [30].

well as peaks at 8.30 eV, 8.70 eV, 9.40 eV, 9.90 eV and 10.75 eV that correspond to *d*-bands of gold [36]. The TPES is also presented in the energy scale referenced to  $E_F = 6.32$  eV, along with the theoretical density of states (DOS) calculated using relativistic augmented plan wave method by Ramchandani [30]. The theoretically calculated DOS are presented with respect to the value reported in the cited study  $E_F = 6.92$  eV. A notably good agreement between the two results confirms that the photoelectrons indeed originate from the isolated gold nanoparticles.

The photoelectron velocity map images (VMIs) obtained at  $h\nu = 10$  eV photon energy for Au NPs, AuTrp, AuRb and ATR particles are shown in Figure 4.5. The VMIs represent a distribution of detected photoelectrons on their momentum. The radial component in the VMI represents the intensity of the velocity vector and it is related to the kinetic energy of the photoelectrons. The direction of the photoemitted electrons with the respect to the direction of the incident light (the arrow on the figure) is described as the angular distribution of the VMIs. As it can be seen in the figure, there is an asymmetry in the angular distribution, since lower parts of the VMIs are of higher intensity. The lower parts of the VMIs correspond to the electrons emitted backward with the respect to the excitation propagation. This asymmetry is a consequence of the distribution of electromagnetic field inside

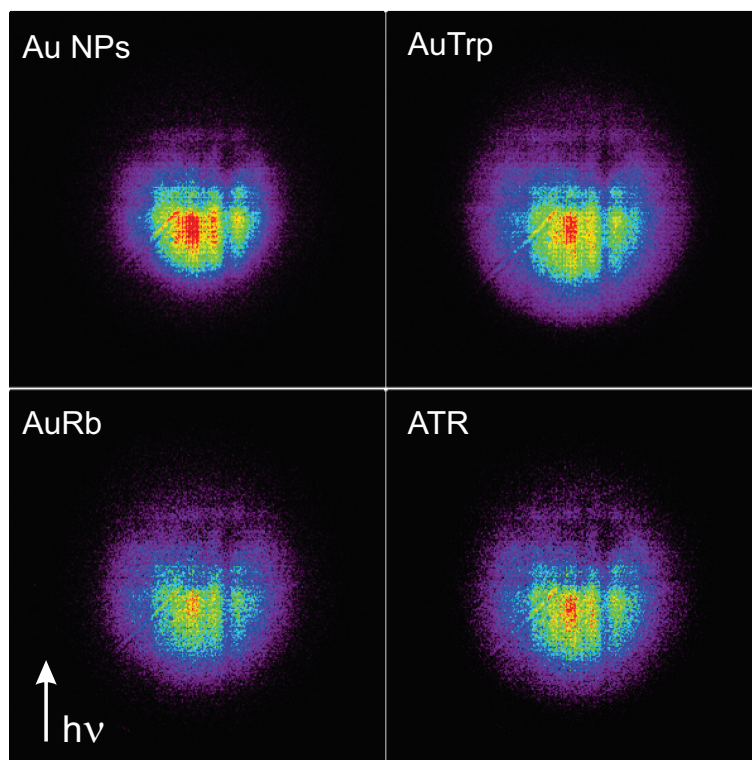


**Figure 4.5:** Velocity map images (VMI) of bare gold nanoparticles (Au NPs), tryptophan-functionalized gold nanoparticles (AuTrp), riboflavin-functionalized gold nanoparticles (AuRb) and bifunctionalized gold nanoparticles using tryptophan and riboflavin (ATR), obtained by using 10 eV synchrotron radiation. The arrow in the bottom left corner indicates the direction of the incident radiation. The images are background-corrected.

the particles. The observed asymmetry provides information on the optical properties of the NPs in the VUV range and on the nature of the electron scattering processes within the particles prior to their escape into the vacuum. It can be seen that the asymmetry is the most pronounced in the velocity map image of the bare gold nanoparticles. In the case of functionalized gold nanoparticles, the adsorbed molecules affect the signal distribution in the VMIs by reducing the asymmetry due to their own contribution to the photoemission. Additionally, photoelectrons created in the gold nanoparticles might get scattered on the biomolecules, which also decreases the level of the observed asymmetry as compared to the VMI of bare gold nanoparticles.

The photoemission spectra of the bare and the functionalized gold nanoparticles, obtained from the VMIs in Figure 4.5 by using pBasex inversion method [158],

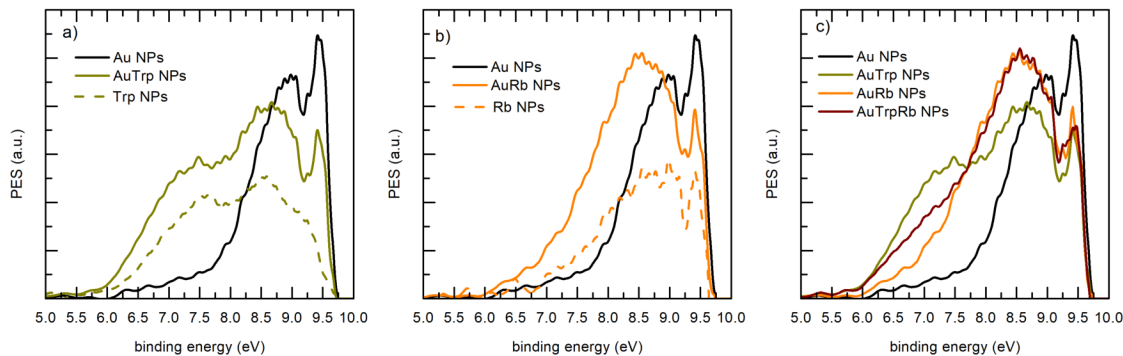


**Figure 4.6:** Normalized vacuum-ultraviolet photoemission spectra (PES) of bare and functionalized gold nanoparticles, as well as of tryptophan and riboflavin aerosol particles obtained at 10 eV photon energy.

are presented in Figure 4.6. The spectra of particles formed by atomization of tryptophan and riboflavin molecular solutions are also shown for comparison. The abscissa represents the binding energy of the electrons with respect to the vacuum level. Note that due to the spread of the values of kinetic energy of the photoelectrons at fixed photon energy, the resolution of the spectra is lower than the resolution of the TPES of gold nanoparticles shown in Figure 4.4(b). Nevertheless, the main features of the structure of the valence bands of gold are visible.

The photoelectron spectrum of the bare gold nanoparticles shows the photoelectrons that originate from the  $6s$  and  $5d$  levels [30, 31, 32, 33, 34, 35, 36, 176]. The onset in the spectrum is followed by a weak peak located around 6.2 eV of binding energy, leaning onto the rest of the spectrum, that can be attributed to  $6s$  electrons of Au NPs [36, 177]. The first prominent peak in the spectrum of the Au NPs sample appears at 8 eV, with the maximum located at 8.9 eV of binding energy. This band is assigned to  $5d$  gold band [32]. Eastman *et al.* found that  $5d$  band of gold exhibits 5 peaks, of which two were main: 2.5 eV and 3.7 eV below the Fermi level. Also, Visikovskiy *et al.* found that  $5d_{5/2}$  level is located  $\approx 3.5$  eV below the Fermi level [36].

In the case of gold-tryptophan particles, the photoemission spectrum shows additional band peaking at  $\approx 7.40$  eV in comparison to the spectrum of bare Au NPs. As it can be seen from the PES of tryptophan particles (dashed line in Figure 4.6(a)), this band originates from the valence band of the amino acid located at 7.60 eV,

but it is slightly shifted toward lower binding energies. This effect is related to the "vacuum level" decrease in the work of Ishii *et al.*, and it is attributed to an influence of the metal surface on the energy bands of the deposited organic layers [94]. In addition, there is a broad band at 8.60 eV in the spectrum of the AuTrp sample, and it represents an overlap between the tryptophan band ( $\approx 8.55$  eV) and the 5*d* band of gold ( $\approx 8.90$  eV). The shift of the Au 5*d* band towards lower binding energies is a consequence of the interaction of the metal with the adsorbed tryptophan molecules that results in the redistribution of the valence gold electrons. Furthermore, it can be noticed that the photoemission onset in the spectra of both Trp and AuTrp particles is far lower than 7.40 eV, which is the ionization energy of free tryptophan molecules [155]. In the case of riboflavin-functionalized gold nanoparticles (Figure 4.6(b)), it can be seen that there are no additional bands in the spectrum in the investigated energy range. However, low ionization potential of riboflavin at around 6.7 eV results in the shift of the 5*d* band of gold towards lower binding energies. Finally, the PES of the ATR sample exhibits mixed features of the photoelectron spectra of all three constituents. The band positioned around 8.5 eV in the ATR spectrum represents band overlap of both biomolecules and Au 5*d* gold band. The intensity of this band is similar to the intensity of the corresponding band observed in the AuRb spectrum. Also, the band of tryptophan located at 7.5 eV is present in the spectrum of bifunctionalized gold nanoparticles, but the band is not fully resolved. This might be due to the photoelectron shielding in Rb molecule due to its larger size comparing to a Trp molecule.

### 4.3 Optical properties of functionalized gold nanoparticles

As mentioned in Chapter 2, the interesting optical properties of a nanosystem are one of the main reasons why nanomaterials became very popular in the first place. On one hand, absorbance characteristics give insight about nanoparticles themselves and their surroundings. On the other hand, luminescent properties of fluorophore-conjugated nanoparticles carry on information about the possible configuration of



the molecules in the nanosystem. This section concerns the absorbance and fluorescence properties of functionalized gold nanoparticles are presented and discussed, ending with an analysis of gold nanoparticles with a particular emphasis on the analysis of the influence of gold NPs on non-radiative resonant energy transfer between tryptophan and riboflavin.

### 4.3.1 Ultraviolet-visible absorbance spectroscopy

Spherical gold nanoparticles, as explained in Chapter 2, have a distinctive absorbance spectrum. The main feature of the spectrum is a surface plasmon resonance peak (SPR), which reflects the symmetry of the nanoparticles. Also, a change in their surrounding results in a shift in SPR peak toward higher wavelengths, which enables a facile tracking of the functionalization process. Typical absorbance spectra of tryptophan- and riboflavin-functionalized gold nanoparticles, as well as of pure solutions of the fluorophores, are given in Figure 4.7. In Figure 4.7(a), the absorbance spectrum of unmodified gold nanoparticles shows the SPR peak located around 520 nm. It is a typical spectrum of spherical, bare, gold nanoparticles of diameter around 8 nm in water surrounding. The spectrum of tryptophan solution has a typical absorbance band located around 270 nm. The band is assigned to the two excited states of tryptophan, namely  $^1L_a$  and  $^1L_b$  states, of indole part of the molecule [178], with  $^1L_b$  being an energetically higher state. Absorbance spectrum of tryptophan functionalized gold colloid differs to the previous two spectra of the Au NPs and Trp samples. SPR peak of gold NPs is shifted toward higher wavelength in the AuTrp spectrum, suggesting a formation of thin layer of tryptophan molecules around gold nanoparticles. This is additionally suggested by a slight broadening of the observed SPR peak. Concerning tryptophan absorbance bands, they are not affected by functionalization, except for an increase in absorbance at the position of the peak, due to the contribution of gold nanoparticles in that part of the EM spectrum.

Figure 4.7(b) shows the absorbance spectra of gold colloid, riboflavin-gold colloid and riboflavin solution of same concentration as the functionalized colloid. It can be seen that the SPR peak of Au NPs underwent the same shift toward higher

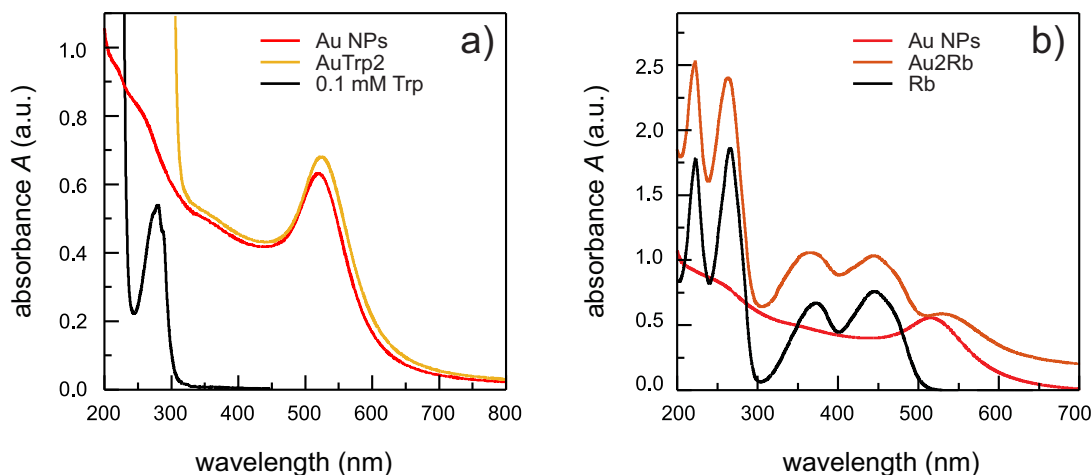


**Figure 4.7:** (a) Absorbance spectra of bare gold nanoparticles (Au NPs, red line), tryptophan solution of 0.1 mM concentration (Trp, black line), and tryptophan-functionalized gold nanoparticles (AuTrp2, yellow line). (b) Absorbance spectra of gold colloid (red line), riboflavin-functionalized gold nanoparticles (Au2Rb, orange line), and riboflavin solution of same concentration (black line) as in the functionalized colloid.

wavelengths, confirming successful functionalization. The spectrum of the riboflavin solution exhibits 4 typical bands: located at 223, 266, 373 and 446 nm. The highest peak, located at 446 nm, can be assigned almost solely to  $S_0 \rightarrow S_1$  electron transition in the riboflavin molecule [179]. The following peak at 373 nm represents transitions from the ground level to the next three excited states. The peak located at 266 nm can be assigned to the  $S_0 \rightarrow S_8$  electron transition, while the lowest peak is probably due to the transition to 10th singlet excited state in the riboflavin molecule [180]. The analysis of the absorbance spectra suggests that there is a minor difference in relative intensities between the Rb absorbance peaks when riboflavin is attached to Au NPs and when it is free in solution. The intensities of the peaks located at 223 and 373 nm are slightly lowered as compared to the intensities of the other two peaks at 266 and 446 nm. The observed effect might be due to the contribution from Au NPs in the collective absorbance spectrum or due to the influence of gold NPs on the higher excited Rb states probabilities. However, the absorbance spectral features of the fluorophores are conserved during the functionalization process, implying also a preservation of their fluorescence properties, as it will be seen in the next subsection.

Bifunctionalized gold nanoparticles are also analysed by means of UV-vis spec-

troscopy. Typical absorbance spectra of gold nanoparticles functionalized by both tryptophan and riboflavin with different amount of riboflavin are shown in Figure 4.8(a). The spectra of the corresponding solutions of Trp and Rb are shown in Figure 4.8(b) (but instead of Au NPs, high-purity water was added in same volume). A typical absorbance peak coming from surface plasmon resonance of the gold nanoparticles is present in the spectrum, with a slight shift toward higher wavelength as the Rb ratio increases, indicating increasing presence of riboflavin molecules on the Au NPs surface. A spectrum for ATR-x (x denotes the amount of riboflavin) samples has the same structure as for the riboflavin-gold colloid shown in Figure 4.7(b). The same stands for TR-x samples, as compared to pure riboflavin solution (Figure 4.7(b)). Tryptophan peaks are located at positions of two Rb peaks of lower wavelengths. Therefore, Trp contribution to the absorbance spectra of the TR samples cannot be distinguished from the Rb contribution. However, the absence of newly formed absorbance features and persistence of original peaks in the bimolecular solutions implies the preservation of the original structures of tryptophan and riboflavin molecules. It is known that in some cases the irradiation of riboflavin in the presence of tryptophan induces a formation of photo-adducts [181]. This process is followed by distortion of Trp-Rb absorbance spectrum, which is not observed here. Therefore, it can be assumed that tryptophan and riboflavin do not mutually interact and form new products, so they are available for the interaction with gold nanoparticles.

### 4.3.2 Photoluminescence spectroscopy

Gold nanoparticles synthesized in the present study do not exhibit fluorescence properties in ultraviolet and visible part of the spectrum of the electromagnetic radiation. However, by conjugating them with fluorophores, these nanostructures can generally inherit their fluorescent characteristics. In turn, the fluorescence properties of the biomolecules are influenced by the presence of metal nanoparticles (Chapter 2.). By analysing the change in their spectral fingerprint, it is possible to gain information about mutual influence and interaction between the adsorbed fluorophore and metal nanoparticles.

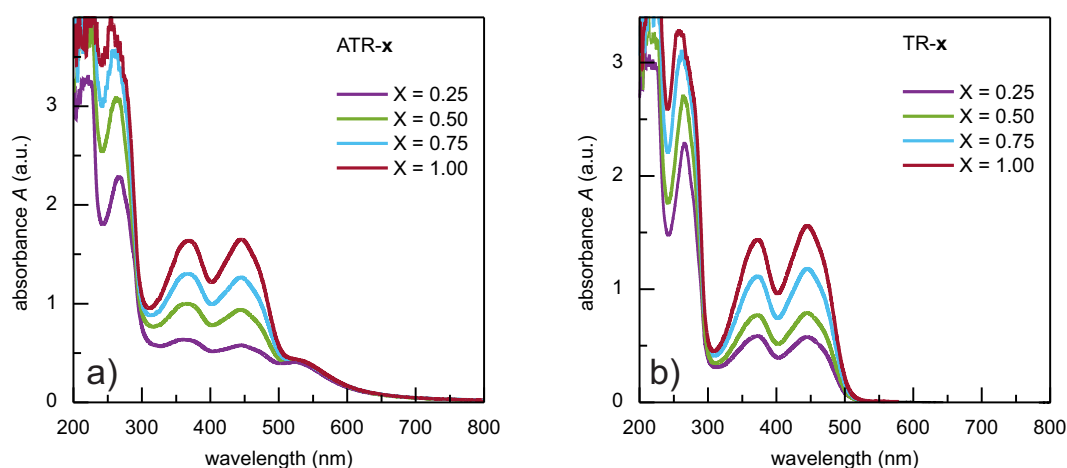


**Figure 4.8:** (a) Absorbance spectra of gold nanoparticles functionalized by tryptophan and riboflavin with increasing riboflavin concentration (noted as ATR $x$ , where  $x$  represents the molar ratio of riboflavin molecules compared to gold nanoparticles, from 0.25 to 1 with steps of 0.25) (b) Aqueous mixtures of tryptophan and riboflavin in same ratios as for the samples ATR $x$ , with added distilled water instead of Au colloid.

The typical photoluminescence (PL) spectra of single-functionalized gold nanoparticles and the corresponding molecular solutions are shown in Figure 4.9. The excitation wavelength was 280 nm, which corresponds to the excitation peak of Trp. The spectra show a fluorescence peak located around 350 nm. This peak is typical for tryptophan in a polar medium and corresponds to the  $^1L_a$  state [182]. Even though concentrations of Trp in the Au-T1 sample and in the pure Trp solution are approximately the same (0.1 mM), the peak intensity in the spectrum of the Au-T1 sample is almost two times lower than the intensity of the corresponding peak in the spectrum of the Trp sample. The observed quenching is due to the newly open non-radiative deexcitation path of a fluorophore introduced by metal nanoparticles in their vicinity [46] (Chapter 2). Comparing to the spectrum of the Au-T1 sample, the Au-T2 sample shows a slight increase in fluorescence intensity, which is expected due to increase in the Trp concentration. The shape of the tryptophan fluorescence peak in the Au-T1 and Au-T2 spectra is similar to that of the pure amino acid, while its position is slightly shifted toward higher wavelengths after the functionalization.

In the case of AuRb sample, the photoluminescence spectrum of riboflavin is affected by the presence of the nanoparticles in a similar way. Normalized PL spectra

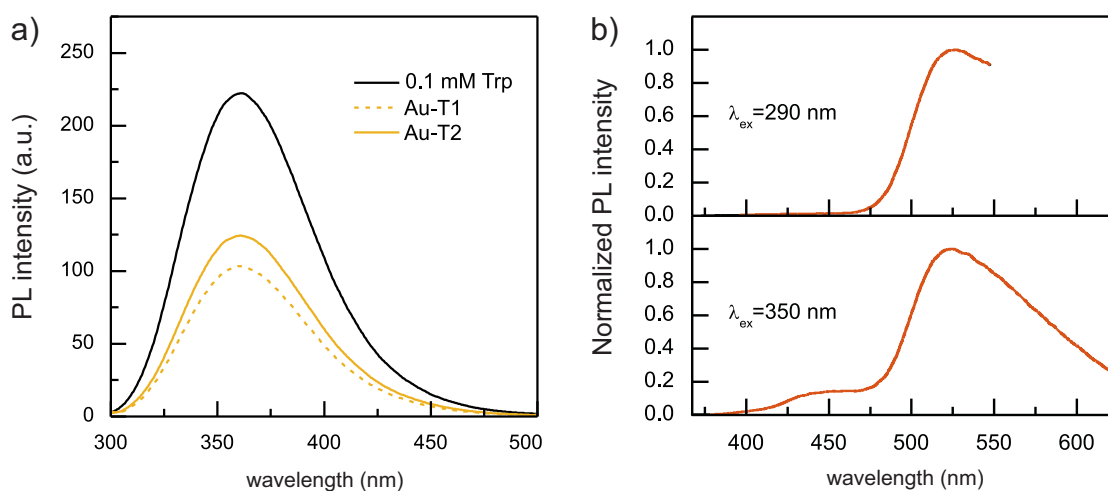


**Figure 4.9:** (a) Photoluminescence spectra of pure tryptophan solution of 0.1 mM concentration (black line), tryptophan functionalized gold nanoparticles in molar ratio 1:1 (Au-T1, dashed yellow line), and tryptophan functionalized gold nanoparticles in molar ratio 1:2 (Au-T2, solid yellow line). The excitation wavelength was 280 nm. (b) Normalized photoluminescence spectra of riboflavin functionalized gold nanoparticles in ratio 2:1, excited by 290 nm (upper graph) and 350 nm (lower graph)

of the Au2-Rb sample obtained at 290 nm and 350 nm excitations are shown in Figure 4.9(b). The shapes of the emission spectra are the same for the both excitation wavelengths, which confirms the unperturbed fluorescence characteristics of riboflavin when attached to gold nanoparticles. It should be noted that nanostructures that exhibit fluorescence upon excitation with photons from the UV part of the electromagnetic spectrum (below 300 nm) are eligible as microscopy probes for deep-ultraviolet fluorescence imaging studies. This will be elaborated and discussed in Chapter 5. On the other hand, the excitation at 350 nm of riboflavin coincides with the position of the emission peak of tryptophan molecules, as it can be seen in Figure 4.10.

The spectral overlap makes tryptophan and riboflavin a pair suitable for resonance energy transfer (RET) (described in Chapter 2). In this case, tryptophan acts as an energy donor, while riboflavin has an acceptor role. We wanted to investigate how the presence of gold nanoparticles influences the RET efficiency between the adsorbed fluorophores. This effect was analysed by means of steady state fluorescence spectroscopy, and typical PL spectra are shown in Figure 4.11. The excitation wave-

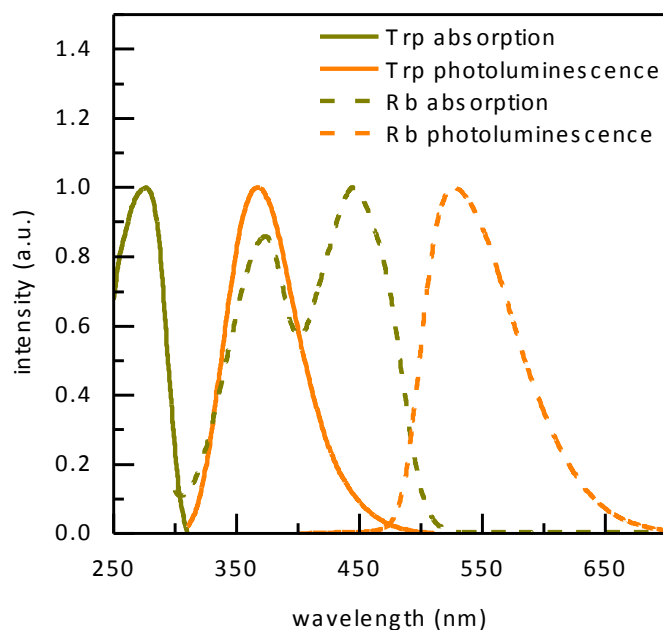


**Figure 4.10:** Normalized photoluminescence excitation and emission spectra (with the excitation wavelength 280 nm) of pure tryptophan solution, and normalized excitation and emission spectrum of riboflavin taken at the emission wavelength 525 nm.

length was 280 nm, and all spectra were acquired between 300 and 600 nm. Detailed procedure of the acquisition and data treatment is given in Chapter 3.

The fluorescence spectra of the bifunctionalized gold nanoparticles with different riboflavin concentrations and corresponding bimolecular solutions are given in Figure 4.11. The concentrations of the fluorophores in the colloids are equal to the analogues samples of the solutions of free biomolecules. The analysed samples are denoted as ATRx and TRx, where x stands for the molar ratio of riboflavin to gold nanoparticles and takes values  $x = 0.25, 0.50, 0.75$  and 1. Also, in order to see how the proximity of the molecules affects the resonant energy transfer between them, we recorded the fluorescence spectra of two identical samples with different concentrations of the solutions. In Figure 4.11, the lower graphs show the PL spectra of the initial samples and the upper graphs the spectra of the same samples but doubly diluted.

The concentration of tryptophan molecules in the AT and ATRx samples is the same. This also applies to the T and TRx samples. However, it can be seen that an increase in the Rb concentration in the ATRx and TRx samples reduces the

intensity of the 360 nm emission peak of tryptophan. This effect is due to resonance energy transfer (RET) between Trp and Rb molecules [183].

Specifically, in the PL spectra of the TRx samples (Figure 4.11(b)), there is a drop in the intensity of the emission peak of Trp in the spectrum of the TR025 sample as compared to the PL spectrum of the T sample. However, the intensity of the Trp peak changes very slowly with the further increase of the Rb concentration (i.e. in the fluorescence spectra of the TR05, TR075 and TR1 samples). As expected, the analysis of the intensity of the emission peak of riboflavin located around 520 nm exhibit a consistent behaviour in the sense of RET presence. A slight increase in the intensity of the Rb peak is seen for the TR05 sample in comparison to the R05 sample, even though the concentration of riboflavin is the same. This additionally confirms the manifestation of RET from tryptophan to riboflavin molecules.

An analysis of the PL spectra of the ATRx samples also shows the presence of RET between tryptophan and riboflavin molecules adsorbed onto gold nanoparticles (Figure 4.11(a)). A continual drop in intensity of the emission peak of Trp is evident in the spectra of the samples as the Rb concentration increases. The RET effect on the intensity of the emission peak of riboflavin is also pronounced when comparing the spectra of the ATR05 and AR05 samples. However, the comparative analysis of the RET influence on the fluorescence properties between the ATR05 and AR05 samples versus the TR05 to R05 samples shows the higher intensity increment of the Rb emission when gold nanoparticles are present. This effect is seen for both dilutions of the samples.

Interestingly, the enhancement of the riboflavin emission peak in the fluorescence spectra of the TRx samples of both dilutions is of similar strength, contrary to the case of the ATRx samples. The separation between the PL spectra of the ATRx samples in the range of the Rb emission peak is more pronounced in the samples of the higher dilution. This might be due to the contribution of the surface plasmons of the gold nanoparticles. The SPR peak of gold is located in the same part of EM spectrum as the Rb emission peak ( $\approx 525$  nm for Rb emission and  $\approx 520$  nm for SPR of Au NPs). A part of the Rb emission can be therefore quenched by the nanoparticles. Consequently, an increase in the dilution of the samples might

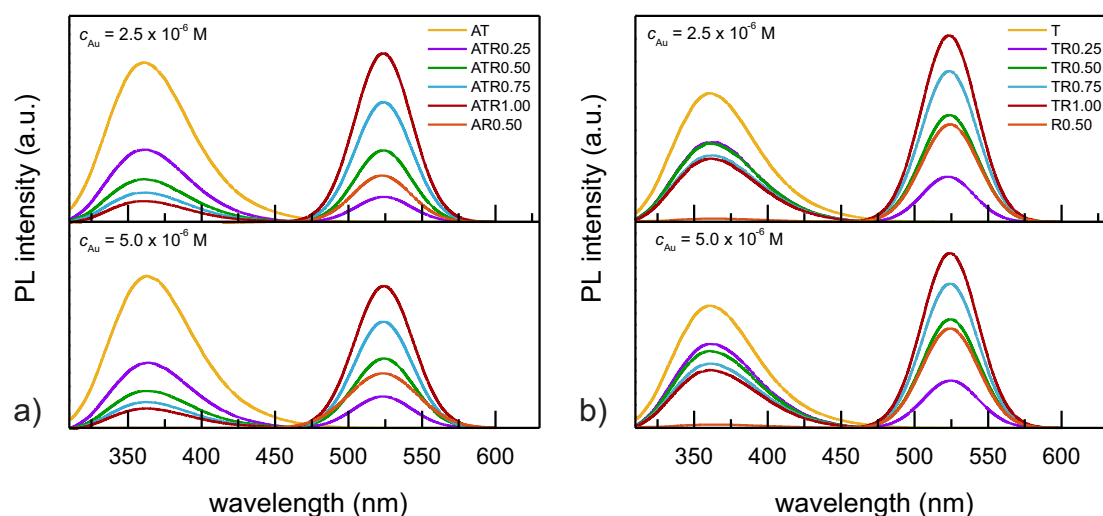


**Figure 4.11:** Photoluminescence spectra of a) gold nanoparticles bifunctionalized by tryptophan and riboflavin and of b) the corresponding tryptophan and riboflavin mixtures. In every group, the riboflavin concentration was varied from 0 to 1 (in molar ratio to gold nanoparticles), with step of 0.25. Control samples were also acquired for tryptophan-gold colloid, and riboflavin-gold colloid. The upper and lower graphs show the PL spectra of the same samples with different concentrations of the solutions. First, the PL spectra of the initial samples are recorded (lower graphs) and then the samples are doubly diluted and the PL spectra were recorded again (upper graphs). Excitation wavelength is 280 nm.



**Table 4.4:** List of the fluorescence intensities of the peaks located at 360 nm and 525 nm (attributed to Trp and Rb, respectively) observed in graphs in Figure 4.11.

$I_{360} / I_{525}$	ATR [5 $\mu$ M]	ATR [2.5 $\mu$ M]	TR [5 $\mu$ M]	TR [2.5 $\mu$ M]
(A)T	553/-	851/-	534/-	280/-
(A)TR025	237/114	385/133	336/206	174/99
(A)TR05	134/252	228/382	335/474	171/233
(A)TR075	93/386	156/638	280/629	145/329
(A)TR1	70/516	111/900	252/763	137/407
(A)R05	-/198	-/247	-/434	-/212

lead to the reduction of this "inner filter" effect of Au NPs. For easier analysis, the intensities of the observed fluorescence peaks located at 360 nm (corresponding to the Trp emission peak) and 525 nm (corresponding to the Rb emission peak) for all samples are listed in Table 4.4. It can be seen that the intensity of the Rb fluorescence peak for the ATR1 and ATR025 samples are 900 and 133 a.u. (for the higher dilution), and 516 and 114 a.u. (for the lower dilution). The differences of the intensities in the two dilutions are almost doubled (767 a.u. and 402 a.u.). This supports the hypothesis that the difference in the increment of the Rb fluorescence is due to the "inner filter" effect of the present nanogold.

In order to show the change in intensity of the Trp fluorescence peak, the ratio of the intensity of the tryptophan emission in riboflavin absence ( $F_0$ ) and the tryptophan emission in the riboflavin presence ( $F$ ) is plotted as a function of the molar content of the riboflavin in the samples (Figure 4.12(a)). It can be seen that the ratios are almost independent on the dilution in the both sample subgroups - ATRx and TRx, respectively. While for the tryptophan-riboflavin mixtures the ratio varies between 1 (no riboflavin in the sample) and 1.5 (at maximal Rb concentration), for bifunctionalized gold nanoparticles this ratio goes from 1 up to 7.85. This can be also presented in terms of the efficiency of resonance energy transfer. RET efficiency is usually defined as  $E_{RET} = 1 - \frac{F}{F_0}$  for donor fluorophores, where with  $F_0$  is noted the fluorescence intensity of the donor in the absence of the acceptor, while with  $F$  is in the other cases notation when the acceptor is present [133, 134, 135, 136]. The efficiency as a function of the acceptor (Rb) concentration is presented in Figure 4.12(b). The efficiency values for pure mixtures of tryptophan and riboflavin vary

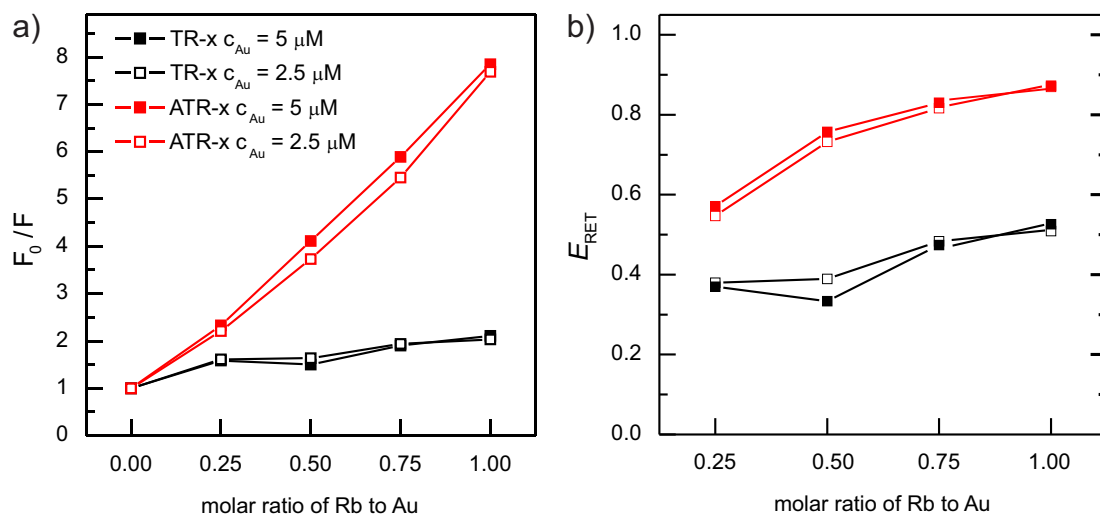


**Figure 4.12:** (a) Ratios of tryptophan peak in samples without ( $F_0$ ) and with riboflavin ( $F$ ) as a function of molar ratio of riboflavin in the samples. Samples with gold colloids are represented in red, while tryptophan-riboflavin mixtures are in black. (b) Efficiency of resonant energy transfer between tryptophan and riboflavin molecules when they are immobilized on the surface of gold nanoparticles (red squares) and when they are free in the solution (black squares).

between 0.37 and 0.52, and generally are in agreement with the reported values in literature [183]. On the other hand, for the same concentrations of donor and acceptor molecules, but in the presence of gold nanoparticles, these efficiency coefficients are in range of 0.54 to 0.87. These results suggest that the gold nanoparticles are promoting RET between Trp and Rb.

---

## Chapter 5

# Application of tryptophan and riboflavin functionalized gold nanoparticles in fluorescence microscopy

Since the era of immunogold labelling, gold nanoparticles have drawn attention as good candidates for application in nanomedicine. As mentioned in Chapter 2, numerous studies are carried out on exploring the potency of nanogold in roles of drug delivery agents, nanocarriers, as theranostics basis, supporters for several types of cancer therapies, and contrasting agents for several imaging techniques [79, 184]. Specifically, in fluorescence microscopy, the development of fluorescent non-organic nanoprobe made them an important alternative to commercially available dyes. Some advantages of these nanoprobe lie in higher degree of photostability and their versatility in tuning spectral and biological properties. Bioconjugation of nonfluorescent gold nanoparticles by fluorescent biomolecules provides fluorescence properties to the whole hybrid nanostructure. In addition, the nanosystem becomes more chemically stable and of improved biocompatibility. Functionalization of gold nanoparticles by fluorophores with excitation and emission maxima in the UV region of electromagnetic spectra extends their applicability. This type of hybrid nanomaterial is eligible for application in deep ultraviolet (DUV) fluorescence microscopy

studies, superior to conventional confocal microscopy techniques due to the smaller diffraction limit. By employing DUV imaging technique, it is possible to follow intrinsic autofluorescence signals of biological material without need of its additional labeling, on single cell levels. However, as it is an active research area, proposed nanoprobe frequently lack full physical characterization which impairs the possibility of drawing more general conclusions on studied nanosystems. Therefore, it is very important to report not only on behaviour of the nanosystem in biological research, but also on their intrinsic physicochemical properties.

Here, we report on bioconjugated gold nanoparticles by tryptophan and riboflavin as fluorescent nanoprobe for bioimaging of bacteria *Escherichia coli*, fungi *Candida albicans* and human hepatocellular carcinoma-derived Huh7.5.1 cell lines. Detailed physical characterization of the functionalized gold nanoparticles is given in Chapter 4, whereas the procedures on preparation are given in Chapter 3. This chapter is organized as follows: the first part consists of fluorescence microscopy study of bacteria *E. coli*, incubated with tryptophan-functionalized gold. In the second part, we analysed biological system fungus *C. albicans* incubated with riboflavin-functionalized gold nanoparticles. In the last section, we demonstrated alternative approach to bioimaging of human carcinoma-derived cell line incubated with biofunctionalized gold nanoparticles, relying on the effect of the resonance energy transfer between tryptophan and riboflavin attached to gold nanoparticles.

## **5.1 Tryptophan-functionalized gold nanoparticles as fluorescence probes for imaging of bacteria *Escherichia coli***

By conjugating gold nanoparticles with tryptophan, the largest of all amino acids and responsible for autofluorescence of proteins and generally any biological material, the hybrid nanostructure inherits its spectral characteristics located in the UV region of electromagnetic spectra. This fluorescent and biocompatible nanostructure is of high stability, and as such is a good candidate as a probe for fluorescence

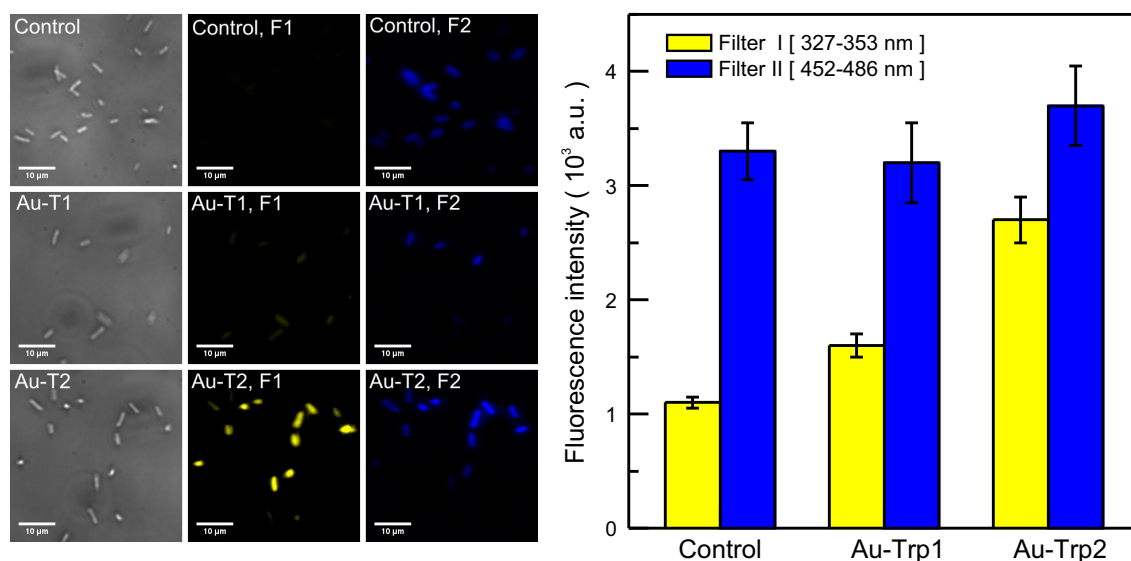


**Figure 5.1:** Bright field (first column) and fluorescence images in Filter I (second column) and Filter II (third column) of control *E. coli* cells (first row) and *E. coli* cells incubated with tryptophan-functionalized gold nanoparticles samples Au-T1 (second row) and Au-T2 (third row). Images were acquired under excitation wavelength of 280 nm, with acquisition exposure time 6 min, in spectral filters 327-353 nm (Filter I) and 452-486 nm (Filter II). Scale bar is 10  $\mu\text{m}$ . In the graph on right side, intensities of samples fluorescence signals are presented. The intensities with their standard deviations were averaged over 10 locations.

microscopy. We tested its potential by analysing incubated bacteria *Escherichia coli* with Au-Trp colloids by means of DUV imaging, and here we present the results. Preparation of samples is described in detail in Chapter 3. Typical bright field and the corresponding fluorescence images of *E. coli* control sample as well as the cells incubated with Au-T1 and Au-T2 colloids are given in Figure 5.1. The fluorescence images were acquired in two spectral regions: 327-353 nm, denoted as the Filter I, and 452-486 nm, denoted as the Filter II. The filters were chosen so that they separate the fluorescent signals coming from tryptophan in the samples (Filter I), from autofluorescence signal coming from the biological material (Filter II). Fluorescence images were acquired for 6 min under 280 nm excitation wavelength. The data was analysed in FIJI image processing software [164]. Intensities for 10 locations per condition were analysed and the results are presented in the graph in Figure 5.1. For samples control, Au-T1 and Au-T2 treated cells, the average intensities are presented with their standard deviation for both filters.

It can be seen that the fluorescence intensities in Filter II are within error margins for all three samples analysed. This indicates that this signal originates from the intrinsic fluorophores in bacteria, i.e. autofluorescence signal. On the other hand, the values of the intensities in Filter I vary with the change in samples, being higher for samples containing Au-T1 and Au-T2 than for the control. This implies that a part of the signal acquired in Filter I comes from the hybrid nanomaterial. The result proves that tryptophan-functionalized gold nanoparticles can be successfully used as a fluorescence probe for deep UV imaging. Also, the analysis of the signals in Filter I shows a correlation with molar content of the amino acid. The average signal for the cells incubated with Au-T2 is approximately 2.5 times higher than the one obtained from the control sample. A strong advantage of deep-UV imaging lies in its superior resolution, as already mentioned. In this study, the images were acquired with resolution of  $\approx 154$  nm per pixel, enabling a further analysis of spatial distribution of the fluorescence signal of the samples within a single cell. In Figure 5.2, a single cell of *E. coli* incubated with Au-T2 colloid is presented in bright-field and in both filters. Below the images, a representative transversal and longitudinal fluorescence profiles are plotted against the distances measured from one cell wall to another. The profiles are coloured in correspondence to the filter analysed and they are normalized for clarity, since their maximal values are different. It can be seen that the transversal profiles are constant as the interior of the bacterium is reached. Similar stands for the longitudinal profile, except that the bacterium dimension is smaller in this direction. The normalized profiles are monotonically increasing going from the exterior, reaching plateau in the bacterial interior. This is especially obvious for the longitudinal direction, as the bacteria are longer in this direction. This indicates that the functionalized gold nanoparticles are not being attached to the bacterial outer membrane, nor located in the periplasmic space, but that they are internalised by bacteria.

These results confirm the potential of tryptophan-functionalized gold nanoparticles in a role as fluorescence probes for imaging of bacteria *Escherichia coli* cells by means of deep-UV fluorescence microscopy.

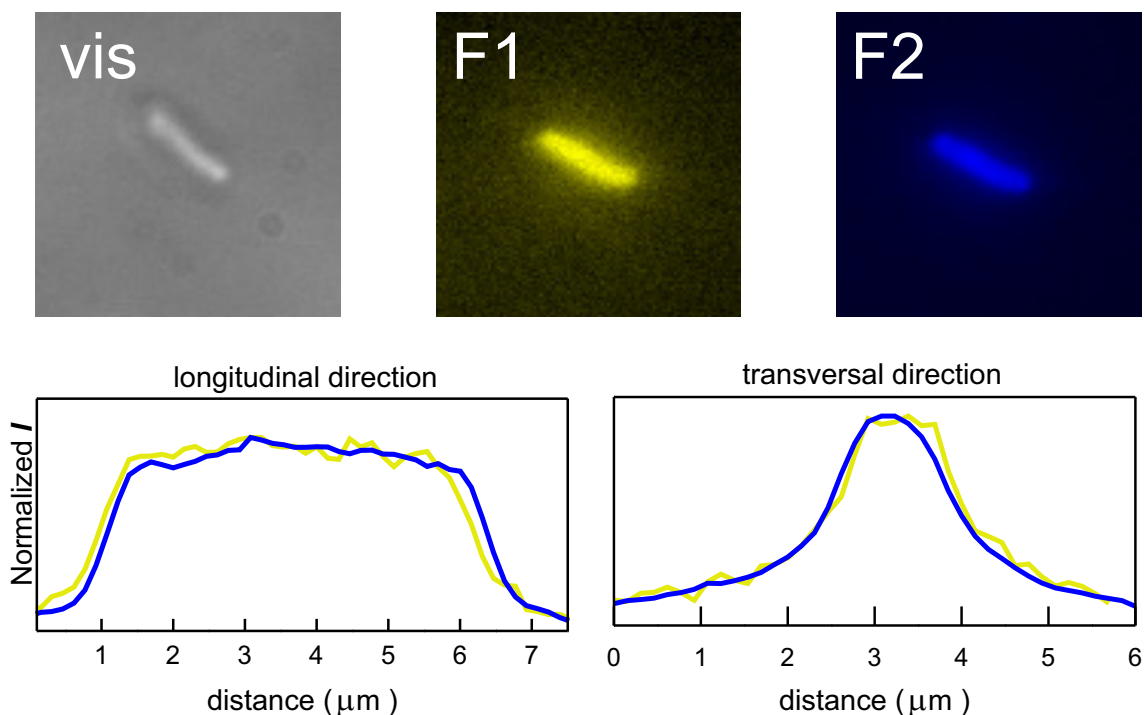


**Figure 5.2:** Bright field and fluorescence images (Filter I in yellow, Filter II in blue) of an *Escherichia coli* bacterium incubated with Au-T2 colloid are presented. Graphs show fluorescence profiles in transversal and longitudinal directions with colour corresponding to the filter.

## 5.2 Riboflavin-functionalized gold nanoparticles as fluorescence probes for imaging of fungus *Candida albicans*

The second nanosystem tested as a labelling agent for fluorescence microscopy involves riboflavin-functionalized gold nanoparticles. Its spectral characteristics are analysed in Chapter 4. Riboflavin, as well as tryptophan, is excited in deep-UV region, but riboflavin emission peak is located around 520 nm. This feature makes riboflavin-gold nanostructure also eligible as probes for deep-UV study of biological samples. However, riboflavin possesses an additional advantage as it has multiple excitation possibilities. This property is beneficial in cases where biological samples have additional but necessary steps in their preparation for microscopy analysis, i.e. fixation, as it will be demonstrated in this study. Riboflavin-functionalized gold nanoparticles (AuRb) were tested as fluorescent probes in study of cell lines of *Can-*

*Candida albicans* fungus. Synchrotron deep-UV fluorescence imaging was performed on glutaraldehyde-fixed *C. albicans* cells incubated with two different concentration of AuRb colloid, of two final gold concentrations of  $C_1$  0.06 mM and  $C_2$  0.12 mM. Detailed preparation procedures are given in Chapter 3.3. The imaging conditions consisted of two used excitation wavelengths corresponding to the excitation peaks of riboflavin: 290 nm and 350 nm. The fluorescence images were acquired in emission range 535-607 nm, corresponding to the emission peak of riboflavin. Typical images are presented in Figure 5.3, together with the average signal intensities obtained from 10 locations. The error bars represent three standard deviations of the averaged detectors signal for each sample, estimated as a square root of the integral number of counts.

It can be seen that the *C. albicans* cells fluoresce in this spectral range for both excitation wavelengths. In the case of 290 nm excitation (presented in green), the signal coming from the control sample is higher than in the samples where the fungus was incubated with AuRb nanoparticles. Lee *et al.* reported that this signal can be assigned to glutaraldehyde-induced fluorescence of *C. albicans*, as the consequence of its interactions with ethylenediamine and secondary amine compounds from the cell [185]. The authors hypothesised that the glutaraldehyde autofluorescence contribution can be lowered by using reductive chemicals. The decrease of the F1 signal obtained here is probably due to the electron donating properties of the gold nanoparticles or from unreacted sodium borohydride that might be present in the colloid, consequently disabling the formation of another fluorescent species on site. On the other hand, in the case of 350 nm excitation wavelength, the fluorescence signal of incubated *C. albicans* with AuRb colloid with  $C_2$  concentration was of higher intensity than the control sample. This increase can be attributed to riboflavin-gold nanoparticles. In addition, the difference between the two concentrations of AuRb sample suggests that there is a concentration threshold that needs to be satisfied in order to have a successful differentiation of the signal origin.

A detailed analysis of spatial distribution of fluorescence signal of *Candida albicans* cells incubated with AuRb colloids of higher concentration ( $C_2$ ) is presented in Figure 5.4. A bright field (Figure 5.4 (a)) and fluorescence image obtained with



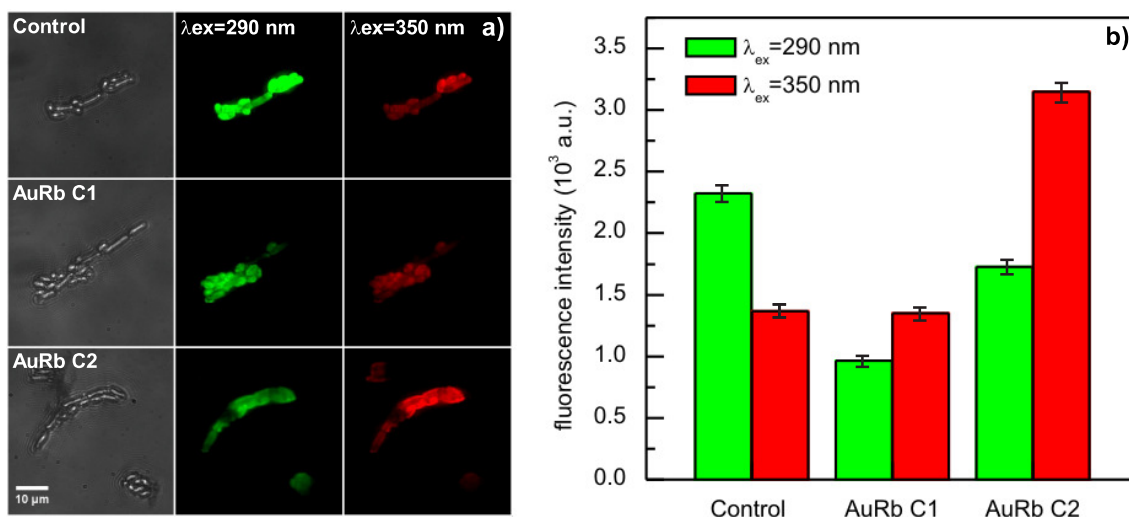


**Figure 5.3:** (a) Bright-field (first column) and fluorescence images for excitation wavelengths 290 nm (second column) and 350 nm (third column) of *Candida albicans* cells (first row) and *Candida albicans* cells incubated with riboflavin-gold colloid of two concentrations (lower  $C_1$  - second row, higher  $C_2$  - third row), in the 535-607 nm spectral range. (b) The average fluorescence intensities of the control sample and *C. albicans* incubated with riboflavin-gold colloid of two final gold concentrations of  $C_1$  0.06 mM and  $C_2$  0.12 mM.

the excitation wavelength of 350 nm (Figure 5.4 (b)) show typical images of the fungus containing both yeast and hyphae cells. It can be seen that the signal is heterogeneous depending on the type of the cells. Yeasts have more pronounced fluorescence than the hyphae. The local maxima of fluorescent signals are shown in Figure 5.4 (c), denoted in white circles of 3 pixels in diameter (462 nm). These local luminescence centres exclusively coincide with the membranes of the fungus. This result strongly suggests that these hybrid nanostructures do interact with *Candida albicans* membranes, but that they are not internalised by the fungus [186].

The analysis presented shows that the functionalization of gold nanoparticles by riboflavin is a good route toward fabrication of hybrid nanostructured suitable for DUV imaging of glutaraldehyde-fixed cell cultures due to biocompatibility and the versatile spectral properties of the biomolecule.

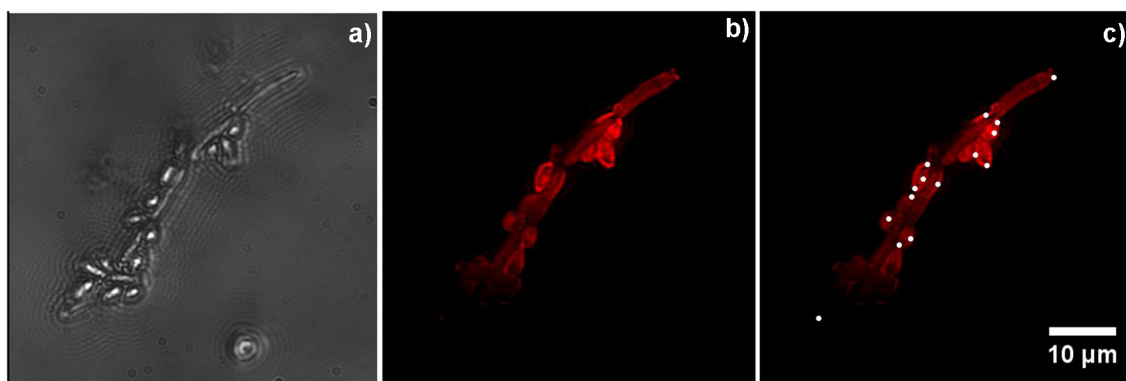


**Figure 5.4:** (a) Bright-field image of the *C. albicans* cells incubated with riboflavin-gold nanostructures (AuRb C<sub>2</sub>). (b) Fluorescence image obtained by 350 nm excitation in the 535-607 nm spectral range. (c) The fluorescence image with labelled local fluorescence maxima (white circles).

### 5.3 Fluorescence imaging study of human hepatocellular carcinoma-derived Huh7.5.1 cells incubated with gold nanoparticles bifunctionalized by tryptophan and riboflavin

Conventional optical microscopy techniques are the most often used for research of biologically relevant processes on a single cell level. They give insight into molecular dynamics of living cell lines and tissues in different environmental conditions, which is crucial for the development of scientific knowledge, as well as new medical approaches for illness treatments. Typical fluorescence microscopy approach is based on differentiating the fluorescent signal of the molecule or structure under investigation from the residual fluorescence in the cell and locating the signal's origins within a biological sample. This is a widely employed technique, especially for prokaryotic microorganisms, as they have a simple cell structure. However, when it comes to more complex cells, such as human tissue cells, signal differentiation is far from a trivial task, since the biomaterial is highly heterogeneous. Moreover, in the case of studies of nanomaterial interaction with cells and tissues, such as for the nanomedicine development, the nanoparticles are of smaller dimensions than the spatial resolution of the optical setup. All of this leads to necessity of other

approaches in utilization of conventional techniques. In this sense, functionalized metal nanoplatforms offer an additional discrimination criterion, as they can have a distinct fluorescence dynamics compared to typical fluorophores that are found in biological samples. This feature of functionalized nanoparticles can be exploited by employing photobleaching imaging techniques. The main rationale behind the photobleaching imaging technique lies in photochemical alteration of studied fluorophores, so that their signal changes in a detectable way upon prolonged exposure to the photoexcitation. Fluorescent molecules that are in an excited state experience photobleaching process via singlet to triplet state transitions or charge-exchange with the surrounding molecules. Consequently, this process results in the deterioration of the molecules fluorescent properties [141, 142]. Since the photobleaching process occurs while the fluorophore is in an excited state, its efficiency is proportional to the lifetime of the particular excited state. The photobleaching imaging techniques are commonly used for studying molecular diffusion in biological materials.

We employed the photobleaching imaging technique to investigate of Huh7.5.1 liver cancer cells incubated with gold nanoparticles functionalized using both tryptophan and riboflavin. We have developed and used this specific nanomaterial since these biomolecules are spectrally coupled fluorophores, more specifically there is an overlap of tryptophans emission and riboflavins excitation bands (see Figure 4.4 in Section 4.1), so they are a suitable pair for the resonance energy transfer (RET). The RET process increases the acceptors fluorescence at the expense of the donors, which is demonstrated in Figure 4.5. In addition, the lifetimes of the donors and acceptors excited states should be affected in the same manner, consequently affecting their photobleaching dynamics [139, 140]. The changes in the lifetimes should be more pronounced in the presence of Au NPs, since the fluorophores adsorbed onto the gold surfaces exhibit higher RET efficiency (see Subsection 4.2.2). Our aim was to use the influence of gold nanoparticles on biomolecules states to study photobleaching dynamics of liver cancer cells incubated with bifunctionalized nanostructures by synchrotron excitation DUV fluorescence imaging. Due to the gold influence on RET pairs dynamics, we expect that photobleaching efficiency will be

lower for tryptophan (donor) and higher for riboflavin (acceptor) in the presence of gold nanoparticles than in the samples that are composed of just tryptophan and riboflavin. This effect will be used as a basis for the differentiation of the fluorescence signal of the nanostructures from the autofluorescence of the cells.

Our chosen biological system was human hepatocellular carcinoma-derived Huh7.5 cell. This cell line is characteristic for its triangular cell shape and highly heterogeneous fluorescence distribution. The cells were incubated with gold nanoparticles bifunctionalized with amino acid tryptophan and vitamin riboflavin. A detailed sample preparation procedure and the list of samples are given in Chapters 3 and 4. Briefly, the bifunctionalized nanoparticle samples were ATR025, ATR05, ATR075 and ATR1 that stands for samples in which gold to tryptophan molar ratio is 1:2, while the gold to riboflavin molar ratios is 0.25, 0.5, 0.75 and 1, respectively. The control samples (gold nanoparticles-A, tryptophan-gold nanoparticles-AT, riboflavin-gold nanoparticles-AR) were prepared using the same procedure using maximal amounts of the biomolecules, while maintaining the same concentration of gold. Finally, for each bifunctionalized nanoparticle sample, a corresponding mixed biomolecule solution was made, using the same concentration of fluorophores, but with the addition of ultrapure water instead of gold colloid. These samples are labelled TR025, TR05, TR075, TR1, T, and R. Overall, fourteen samples of incubated Huh7.5 cells were prepared for deep-UV fluorescence microscopy study, which will be referred to as Huh-ATRx and Huh-TRx. Experimental conditions for the DUV imaging is described in Chapter 3 in detail. Briefly, DUV imaging for each sample consisted of two parts - steady state fluorescence imaging of several locations, after which a time-lapse acquisition was done on a specific representative location. Excitation wavelength was 280 nm, and fifteen fluorescence images were iteratively collected in each of two spectral ranges: 355-405 nm (F1) and 510-560 nm (F2), for 30 seconds of acquisition time for each filter. The spectral ranges were chosen to discriminate between tryptophan and riboflavin emission peaks.

Bright-field images of human liver cancer cells incubated with bifunctionalized gold nanoparticles, the control samples and the samples treated with the corresponding biomolecular solutions are shown in Figure 5.5. It can be seen that the

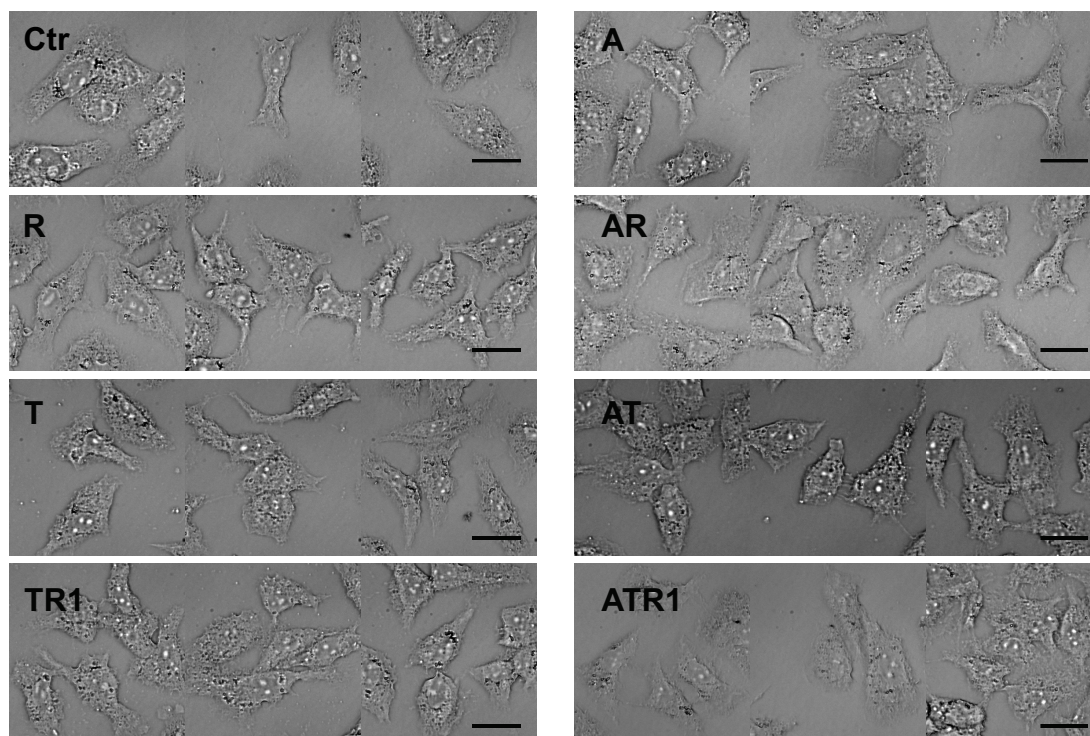


**Figure 5.5:** Bright-field images of treated human liver cancer Huh7.5.1 cells. A stack of three different locations is shown for each sample. The denotation of the samples is given in the upper left corner of the image: Ctr - control; A - bare gold nanoparticles; R - riboflavin incubated cells; AR - riboflavin-functionalized gold NPs; T - tryptophan incubated cells; AT - tryptophan-functionalized gold NPs, TR1 - tryptophan-riboflavin solution; ATR1 - bifunctionalized gold NPs. Scale bar represents  $30\ \mu\text{m}$ .

cells preserve their typical triangular shape with distinctive separation of the nucleus. This observation is consistent with literature that reports that bioconjugated gold nanoparticles in low concentrations are not cytotoxic for human cell lines and are being easily internalised [77, 95, 96, 127, 128, 130, 187].

The steady-state fluorescence images of the control, as well as the Huh-A, Huh-AT and Huh-ATR1 samples for both F1 and F2 are presented in Figure 5.6. It can be seen that fluorescence signals in the F1 spectral range are spread over the cells, whereas in the F2 spectral range the nuclei can be spotted easily. Unfortunately, the analysis of the images proved inconclusive in any attempt of nanostructures colocalization due to a strong autofluorescent signal in the second filter, 510-560 nm, which impaired comparison with the signal in the first filter, 355-405 nm. Strong signal in F2 is characteristic for cells endogenous autofluorescent species and also

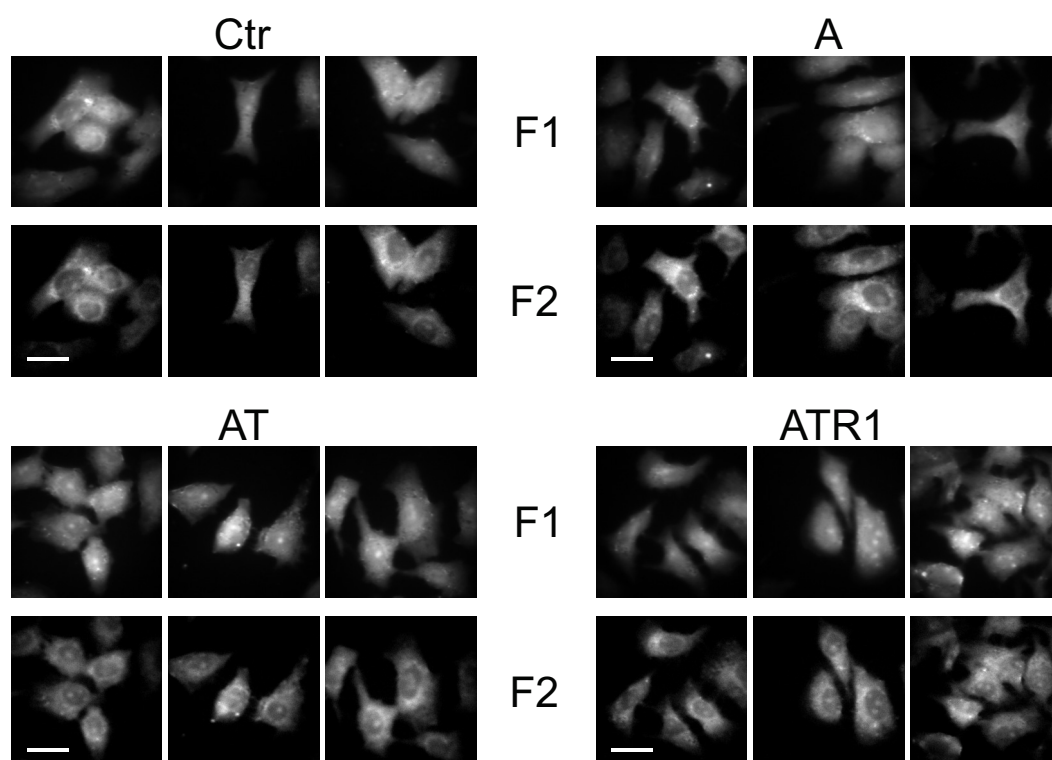
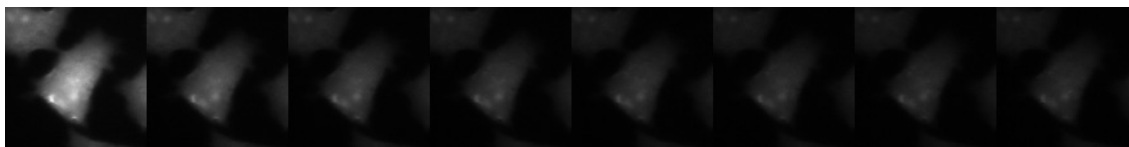


**Figure 5.6:** Fluorescence images of treated human liver cancer cells. A stack of three different locations is shown for each sample. The denotation of the samples is given in the above the image stack for samples: Ctr - control; A - bare gold nanoparticles; AT - tryptophan-functionalized gold NPs, ATR1 - bifunctionalized gold NPs. Fluorescence images were equalized in minimum and maximum display range within each filter for all samples. Scale bar represents 30  $\mu\text{m}$ .

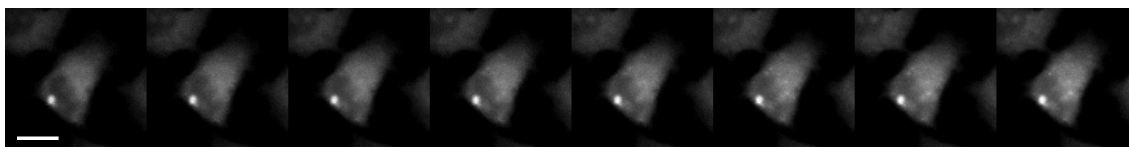
attributed to photocreation of new fluorescent molecules in biological environment, such as NAD(P)H, that are fluorescent in this spectral range [188, 189, 190].

For the mentioned reasons, we performed time-lapse measurements with the aim of studying spatial distribution of the nanostructures by analysing differences in the fluorescence dynamics. Representative locations were chosen for each sample by looking for the cancer cells of characteristic triangular shape. An example of such time-lapse acquisition is given in Figure 5.7. The figure shows every second image acquired in both filters (F1 - upper row, F2 - lower row), with denoted timeline. The fluorescence intensity in the F1 spectral range, assigned to tryptophans emission peak, is decreasing in time showing on-going photobleaching process. On the other hand, the emission peak of riboflavin, located in the second filter F2, slowly increases in time. This observation is consistent with the general evolution of the

F1 : 355 - 405 nm



F2 : 510 - 560 nm



time

**Figure 5.7:** Time-lapse images acquired for Huh7.5 liver cancer cells incubated with the ATR1 sample. For clarity, every second image acquired is presented. Fluorescence images were recorded in two spectral filters: 355-405 nm (F1), and 510-560 nm (F2), with acquisition time of 30 seconds per image for each filter. Scale bar represents 30  $\mu\text{m}$ .

autofluorescent signal in this spectral range [189].

Uptake of nanostructured gold particles is generally well established in literature [21, 125, 126, 127, 129, 187]. However, the nanomaterials internalization by the cells nuclei highly depends on the encapsulation materials used [124, 130, 191]. Only few conclusive reports give evidence of the nanoparticles nuclei penetration, as, for example, in the study of *Nativo et al.* on HeLa cells that used functionalized gold nanoparticles by nuclear localization signal peptides [124, 191]. In our study of Huh7.5.1, the treatment with bifunctionalized nanoparticles did not produce observable changes in the nucleus fluorescence. Therefore, we limited our analysis to the cells cytoplasmic region, which is the most probable location of the nanoparticle accumulation in the cells. The selection was done manually for each sample by comparing visible and both fluorescence images. Afterwards, the overall intensities were calculated by applying obtained cytoplasmic masks onto fluorescence images and averaging selected pixels values. The time-course signals were normalized to their first time point, as presented in Figures 5.8, 5.9 and 5.10.

The time dependence of normalized average fluorescence intensities in cytoplasmic region for cancer liver cells incubated with gold nanoparticles (A), tryptophan solution (T), tryptophan-functionalized gold nanoparticles (AT), tryptophan-



riboflavin solution (TR1) and bifunctionalized gold nanoparticles (ATR1) in the spectral window F1 are shown in Figure 5.8(a). It can be seen that each sample exhibits photobleaching (PB) in the F1 range. However, there is a remarkable difference in the rate of the PB processes between the samples. This difference is particularly pronounced in the Huh-ATR1 sample, since it showed the highest saturation intensity ( $F1_{sat}$ ). The inset to Figure 5.8(a) shows comparison between the saturation intensities of the treated Huh cells samples. A higher  $F1_{sat}$  value for the Huh-ATR1 sample in comparison to the Huh-AT sample suggests that it takes more time for the photoluminescence to decay *via* photobleaching. This indicates that the lifetime of tryptophan in the excited state is shorter, thus new deexcitation pathways are being formed. This is a consequence of a RET process between tryptophan and riboflavin molecules adsorbed on the Au NPs ([183]). The effect is far less pronounced for the Huh-TR1 sample. It is interesting to notice that incubation with non-functionalized gold nanoparticles results in  $F1_{sat}$  that is in between the Huh-ATR1 and Huh-TR1 samples. This effect is probably a consequence of a decrease in the lifetimes of the excited states of endogenous fluorophores found in Huh cells that are in vicinity of gold nanoparticles.

The effect of the successive acquisitions upon exposure to the 280 nm radiation for the same samples, but for the luminescence in the 510-560 nm range (filter F2) is shown in Figure 5.8(b). As noticed in Figure 5.7, the F2 signals generally increase with time which is a typical behaviour of the fluorescence of endogenous fluorophores present in the biomaterial in this spectral range. However, there is an obvious difference in the increase of the fluorescence rates of the particular samples. In the F2 spectral range, the signals coming from the cells incubated with both tryptophan and riboflavin increase by a lower extent than the signals coming from the cells incubated with just one type of the molecule. This effect is even more pronounced in the presence of gold. The lower increase rate of the fluorescence in the case of the Huh-ATR1 sample in comparison to the Huh-TR1 sample is a consequence of a higher RET efficiency of the bifunctionalized nanoparticles (see Figure 4.12). More specifically, the presence of tryptophan in the vicinity of riboflavin induces an increase in the lifetime of riboflavin excited states resulting in more efficient



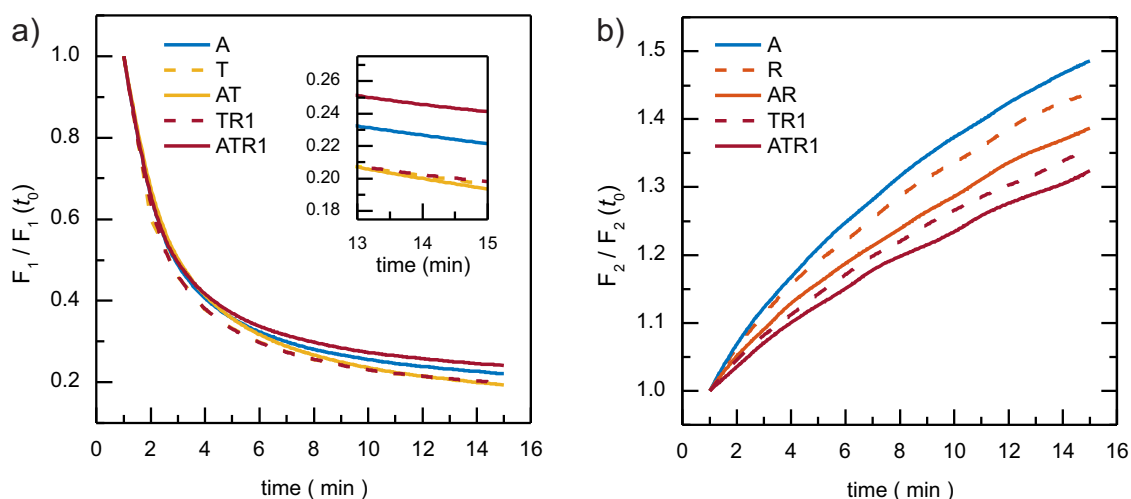


**Figure 5.8:** Time dependence of the normalized averaged fluorescence intensities in cytoplasmic region of Huh treated cells with colloids (a) A (solid blue line), T (dashed yellow line), AT (solid yellow line), TR1 (dashed maroon line), and ATR1 (solid maroon line) in the F1 spectral range (305-405 nm); the inset shows last three time points of the same signals; and (b) A (solid blue line), R (dashed orange line), AR (solid orange line), TR1 (dashed maroon line), and ATR1 (solid maroon line) in F2 spectral range (510-560 nm).

photobleaching in the F2 channel. This effect is manifested by a lower increase of the fluorescence. In the case of Huh-AR *vs* Huh-R samples, the situation is more complicated. From the photoluminescence results (Chapter 4), it is known that gold quenches riboflavin fluorescence as the SPR peak coincides with the Rb emission peak. This results in a lower overall fluorescence in the F2 range. However, the fluorescence quenching by the Au NPs would result in reverse order of the curves, which implies another dominant effect of gold on the PB of riboflavin. The observed behaviour is probably related to the fact that riboflavin concentration on the nanoparticle surface is higher than the concentration of the biomolecule in solution, which increases the detection probability in cell imaging. Also, since the valence level of riboflavin, unlike the one of tryptophan, coincides with the  $5d$  band of gold (see Subsection 4.2.2, Figure 4.6), the photoexcited electron in riboflavin can be transferred to the metal, which would contribute to the PB of the biomolecule.

In Figure 5.9 (a), a comparison is made between the fluorescent dynamics of Huh cells incubated with bifunctionalized gold nanoparticles with different Rb concentrations in the F1 range (the average fluorescence evolution curves of the control sam-

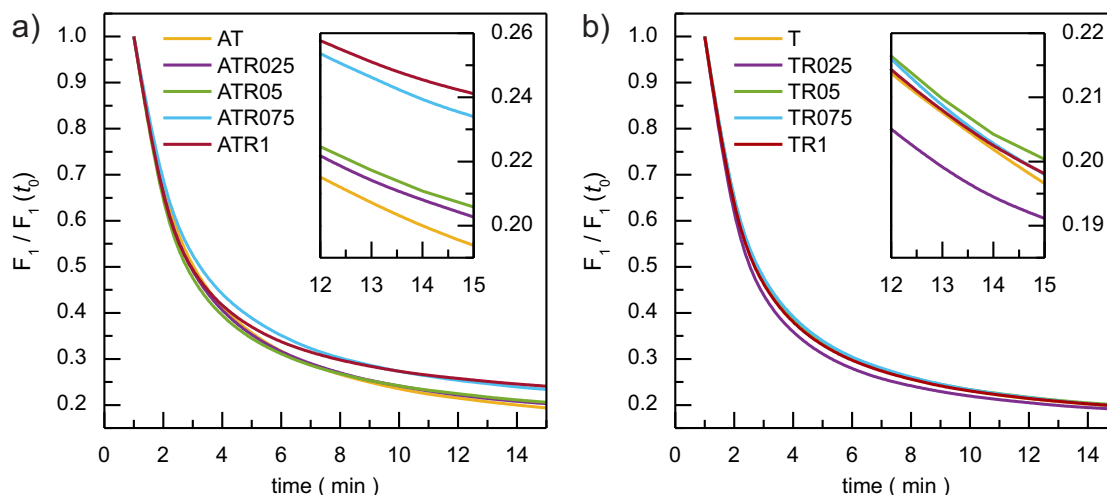


**Figure 5.9:** Time dependence of the normalized averaged fluorescence intensities in cytoplasmic region in the F1 range (355-405 nm) for (a) AT (yellow), ATR025 (violet), ATR05 (green), ATR075 (blue) and ATR1 (maroon) samples, as well as (b) T (yellow), TR025 (violet), TR05 (green), TR075 (blue) and TR1 (maroon) samples. Insets graphs present magnified last four time points in same signals.

ples, i.e. those that do not contain gold nanoparticles, are given in Figure 5.9 (b)). The time dependence of the normalized averaged signals in the cells cytoplasmic region are given for (A)T, (A)TR025, (A)TR05 and (A)TR1 colloids. It can be seen that the PB degree for Huh cells incubated with bifunctionalized gold nanoparticles increases as the riboflavin concentration decreases. On the other hand, Huh cells treated with tryptophan-riboflavin solutions have similar saturation values. The fact that Huh-ATR1 and Huh-ATR075 display lower PB efficiency ( $F_{1\text{sat}}$  0.23-0.24) in comparison to the rest of the samples, which are below 0.21, also suggests a possibility of existence of a concentration threshold for the detection of the riboflavin photoluminescence.

Figure 5.10 shows the change in the fluorescence intensity over time in the F2 range for the same set of samples. The time dependent fluorescent behaviour is a bit different, due to generally low signals in this spectral range (as it will be seen later in text). Nevertheless, a general trend can be observed, since Huh cells treated with bifunctionalized gold colloids show lower increase (30-40%) of the initial value than it is the case with the Huh-TR samples, where the increase goes up to 55%.

Due to the observed differences in time dependence of normalized averaged signals between the samples, we decided to study signal evolutions in more detail. The

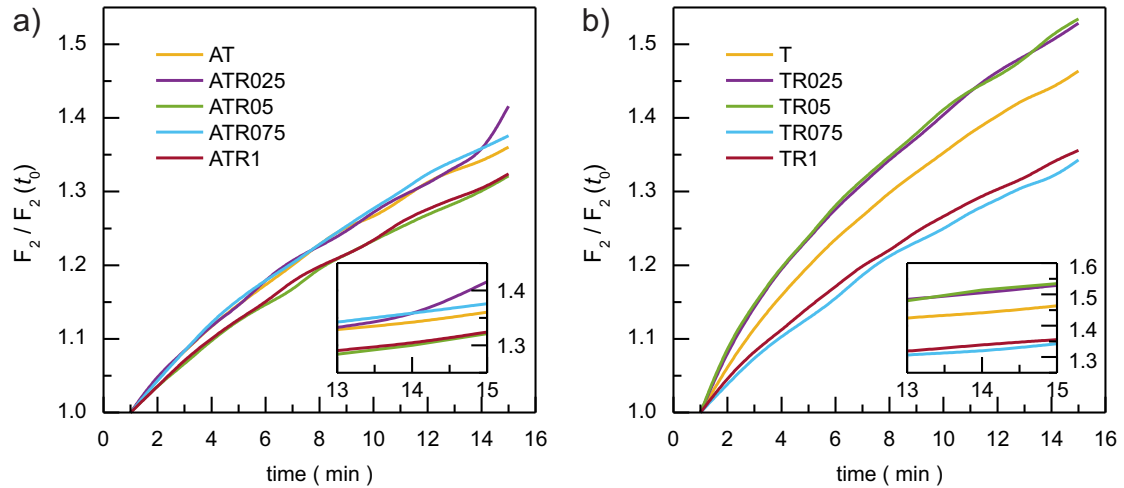


**Figure 5.10:** Time dependence of the normalized averaged fluorescence intensities in the Huh7.5 cytoplasmic region in the F2 range for (a) AT (yellow), ATR025 (violet), ATR05 (green), ATR075 (blue) and ATR1 (maroon) samples, as well as (b) T (yellow), TR025 (violet), TR05 (green), TR075 (blue) and TR1 (maroon) samples. Insets graphs present magnified last three time points in same signals.

difference in the PB dynamics between samples imposed a criterion for pixel classification that would separate the areas of different composition. As radiation processes are generally described by exponential time dependencies, the photobleaching processes inherit this functional dependency on time [139]. The higher PB degree would induce lower saturation values of the particular signal, which we used as a classification marker. The images obtained in the F1 channel were given preference for the classification due to higher intensity values, which provided the robustness to the analysis. The value of each pixel in the images was subtracted by  $\approx 80\%$  of the background contribution from its raw value, to avoid division by small numbers in the normalization process that could induce false conclusions. The fluorescence intensity of the pixels related to the cytoplasm steadily decrease with time, whereas the background pixels, had low initial values and did not vary with time, resulting in high saturation values. The pixel categorization consisted of selecting pixels with the saturation values falling into intervals between 0.15 and 0.45 separated by 0.05. For instance, the pixels in the category 0.20-0.25 have their normalized saturation values between 0.20 and 0.25. Note that there is a difference between these categories and the saturation values shown in Figures 5.8-5.10, due to the background subtraction. A typical results obtained by using procedure for pixel categorization for the Huh

control, Huh-A, Huh-AT and Huh-ATR1 sample is shown in Figure 5.11. For each sample, the pixel classification procedure produced a mask that corresponds to different PB dynamics areas, denoted as a category. The saturation values in the F1 range fluorescence images that were higher than 0.45 represented the background in all the samples and this value was taken as the upper limit of the categorization. On the other hand, there were very few pixels below the 0.15 saturation value in all the samples, and that imposed the lower limit of the categorization. It can be seen that higher categories cover regions closer to the cell edges. Bearing in mind that the biological material on the microscopy coverslips is of non-homogenous thickness that increases towards the centre of the cell, this spatial distribution is expected, since higher saturation values in the images correspond to a lower concentration of the fluorophores. However, as it can be seen in the figure, the spatial distribution of the pixels in a given category changes between samples, which implies the presence of external fluorophores and justifies the classification approach.

For each category, the calculated mask was used to extract the average signal intensities in F1 and F2 ranges from each of the preselected areas, as well as their standard deviations. The standard deviations were taken as intervals of the fluorescence intensities in a given category. The number of pixels differed for the each category, and the histogram of the number of pixels in each category divided by the total number of selected pixels in the given sample ( $\delta N_{F1}$ ) is represented in Figure 5.12. The calculated values of  $\delta N_{F1}$  for the Huh-A, Huh-AR, Huh-AT and Huh-ATR1 sample are presented in Figure 5.12(a), while the fractions that correspond to the cells treated with biomolecular solutions, the Huh-control, Huh-R, Huh-T and Huh-TR1 samples, are presented in Figure 5.12(b). The figures show that pixel distribution for the control sample is leaning towards higher saturation values. This implies that the fluorescence intensity of the control sample does not change significantly with time due to generally low intensity of its initial fluorescence. The cells treated solely with biomolecules (R, T and TR1), and the cells treated with single functionalized nanoparticles (AR and AT) show the highest number of pixels in the 0.20 - 0.25 category. On the other hand, in the images of the cells that contained the bifunctionalized nanoparticles ATR1 and the bare gold nanoparticles, the largest

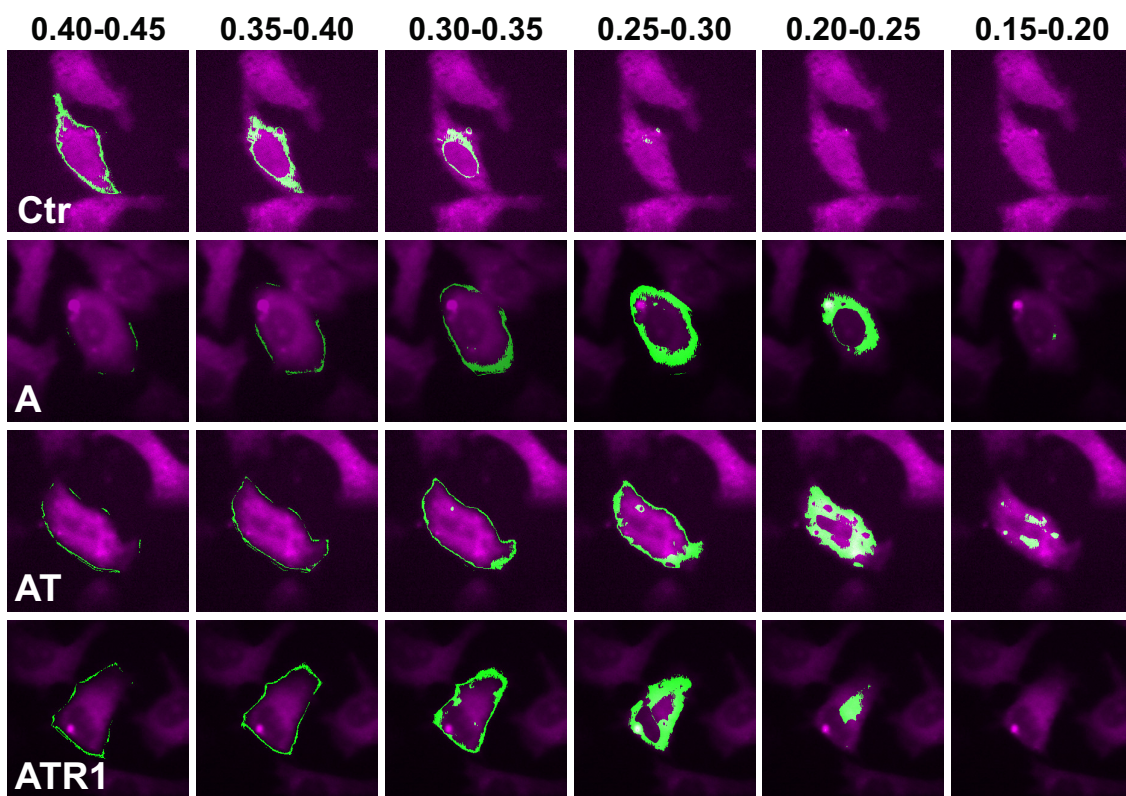


**Figure 5.11:** An example of F1 categorization for the control, A, AT and ATR1 sample. Every category presents a pixel classification based on their normalized saturation values based on their saturation values in F1 spectral range, as described in the text.

contribution comes from the pixels that belong to the 0.25-0.30 category.

We were also interested in the change in the  $\delta N_{F1}$  distribution with change in the concentration of riboflavin. The  $\delta N_{F1}$  values obtained from the images of the cells treated with bifunctionalized gold nanoparticles and the biomolecular solutions are shown in Figure 5.12 (c) and (d). The figure shows that there is a consistent shift of the maximum in the  $\delta N_{F1}$  distribution from lower to higher category with an increase in the riboflavin to gold molar ratio. This is more apparent for the cells treated with ATRx colloids than for the cells treated with TRx solutions. Overall, the largest fraction of  $\delta N_{F1}$  in the images of the Huh-ATRx samples belongs to the category 0.25-0.30, whereas for Huh-TRx, they belong to the category 0.20-0.25. Specifically, the sample Huh-ATR025 shows a monotonous decrease in  $\delta N_{F1}$  values as the category increases. The same stands for the sample Huh-ATR05, although it contains a similar number of pixels in categories 0.20-0.25 and 0.25-0.30. On the other hand, the samples Huh-ATR075 and Huh-ATR1 have the largest number of pixels in the category 0.25-0.30 and a slightly lower number in the category 0.30-0.35. Additionally, there were no pixels in the 0.15-0.20 category for these two samples. It also worth to notice that there are no significant differences in the images of the samples treated with Trp-Rb biomolecular solutions with respect to those of the samples treated with the single-biomolecule solutions. The category with the highest number of pixels is the 0.20-0.25 category for the samples Huh-TR025 and Huh-TR05, whereas for Huh-TR1 the categories 0.20-0.25 and 0.25-0.30 are equal. The sample Huh-TR075 shows inconsistency with the other Huh-TRx samples, by having the highest values of  $\delta N_{F1}$  in the 0.25-0.30 category. This is probably of the experimental origin, as the inconsistencies of the cells incubated with TR075 persists and will be seen later in text. Overall, these results suggest that the presence of bifunctionalized colloids in the cells generally reduce the degree of photobleaching of the cells. This is the most apparent in the case of Huh-ATR075 and Huh-ATR1 samples.

The category masks were used to calculate the average intensity values for each sample at every time point. The temporal change of dependence of the intensity in the F2 spectral range on the intensity in the F1 range is presented in Figure 5.13.

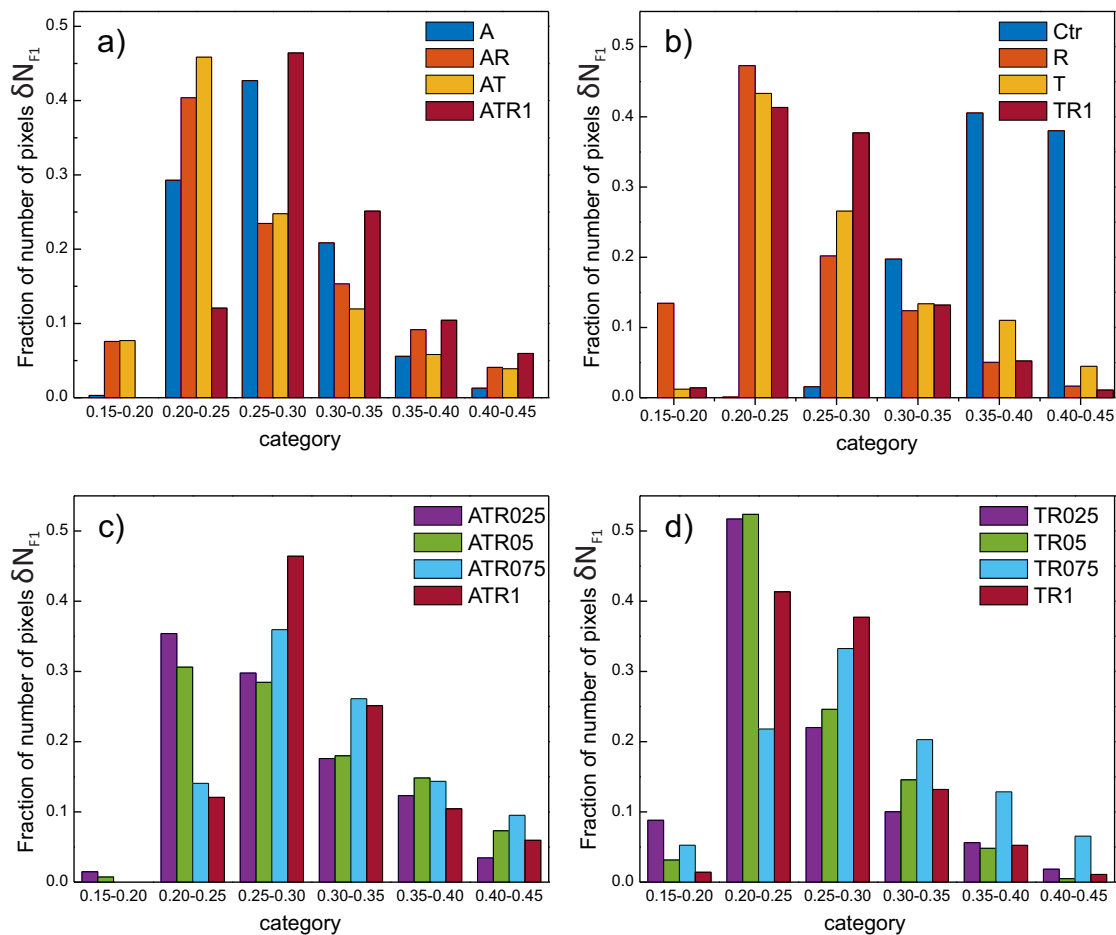


**Figure 5.12:** The histograms of the fractions of number of pixels in the each category,  $\delta N_{F1}$ , for the Huh cells treated with the (a) A (blue), AR (orange), AT (yellow) and ATR1 (maroon) colloids; the (b) Ctr (blue), R (orange), T (yellow) and TR1 (maroon) solutions; the (c) ATR025 (violet), ATR05 (green), ATR075 (blue) and ATR1 (maroon) colloids; and the (d) TR025 (violet), TR05 (green), TR075 (blue) and TR1 (maroon) solutions.  $\delta N_{F1}$  represents a number of pixels per category divided by the total number of detected pixels in a sample.

The background subtraction from raw values was done for all the samples, which was estimated as a mean value of the darkfield of the detector. The maximal errors were estimated to be only 65 counts for the highest intensity values and are excluded from graphs for the sake of clarity. It can be seen that as the category lowers, the intensities increase. This is expected since the areas closer to the cells interior have higher values of the fluorescence signals. The curves of the signal evolutions of the samples are grouped for categories 0.40-0.45 and 0.35-0.40, which is consistent with the cell selection in these categories the covers the very borders of the cells (as inspection of corresponding masks confirms, Figure 5.11). The only exception is the control sample, where the high categories cover the whole cytoplasmic region. However, its intensities are low, positioning the curve of the control sample in the proximity to the other samples. On the other hand, the F2/F1 dependencies are different for lower categories. The most pronounced sample separation is observable for the categories 0.25-0.30 and 0.20-0.25, suggesting that the colloids fluorescence is detected within the pixels that follow this particular type of the PB dynamics, which manifests through significantly higher intensities of the Huh-ATR1, Huh-ATR075 and Huh-A samples.

As a next step, we wanted to analyse contributions from the pixels assigned to each category to the overall mean fluorescence intensity. To this purpose, the intensities in each category were weighted by the fraction of the number of pixels in the corresponding category. These weighted fluorescence evolutions for each sample are presented in Figure 5.14 for the F1 spectral range and Figure 5.15 for the F2 spectral range. Summing over all categories, overall fluorescence could be obtained for each sample. It can be seen that in the majority of the samples, the category 0.20-0.25 (denoted in green) contributes the most to the overall intensity. Still, the fluorescence signal of the control sample exhibits different pattern, consistent with the previous analysis. The intensity of the control fluorescence is generally lower, which consequently led to high normalized saturation values. On the other hand, the situation changes from the Huh-AT sample toward Huh-ATR1. It can be seen that as the concentration of the riboflavin in the colloid increases, the contribution of the category 0.25-0.30 to the samples overall average fluorescence becomes higher.



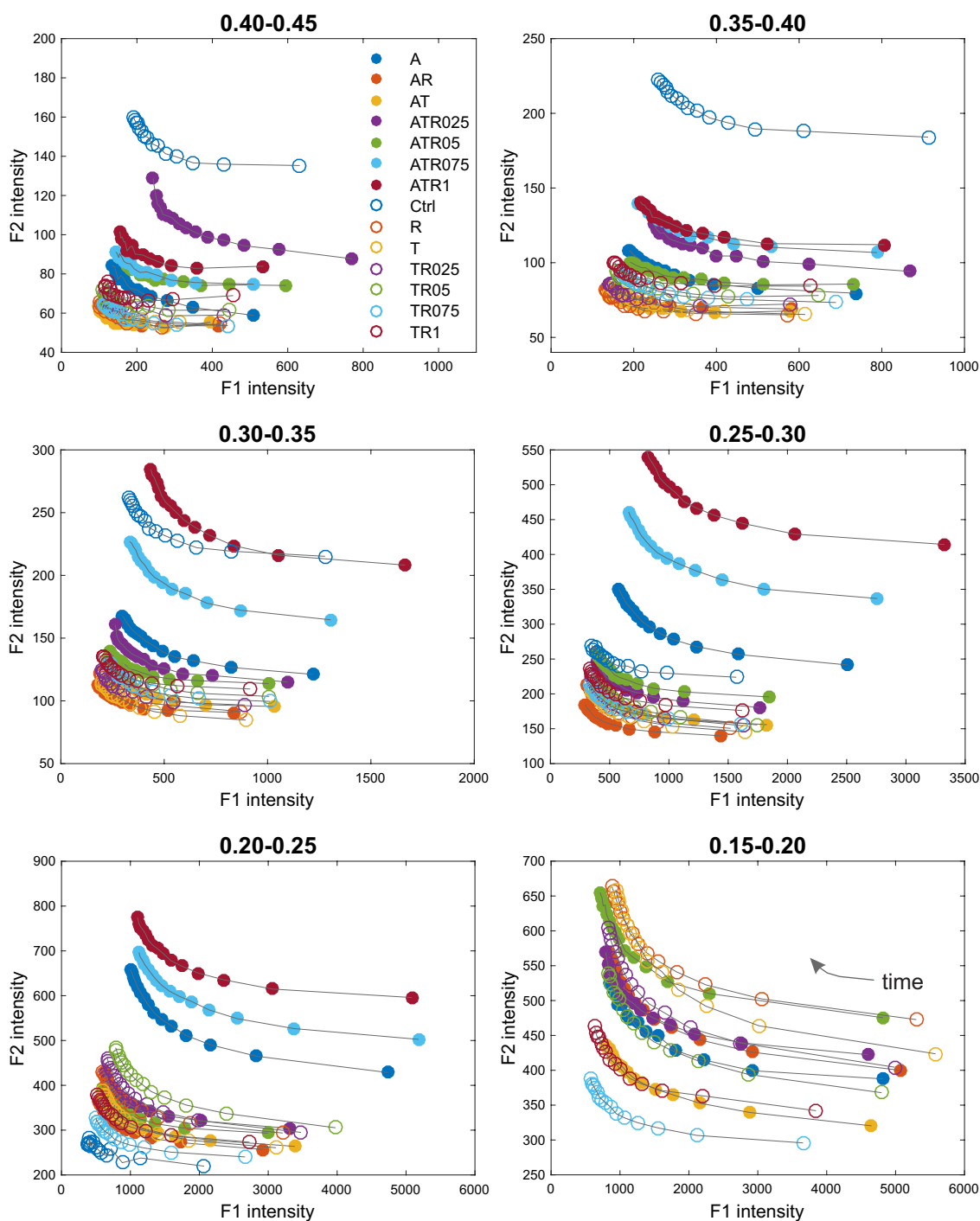


**Figure 5.13:** The evolution of the fluorescence intensity in the F2 spectral range as a function of the fluorescence intensity in the F1 range are presented for Huh7.5 cells incubated with bifunctionalized gold nanoparticles and corresponding bimolecular solutions for each category (noted in the graph titles). The categories correspond to the different photobleaching dynamic of the fluorophores present in the samples. The listed samples and their representation colours are given in the legend. Time progress is marked by an arrow in the lower right graph, indicating the evolution is oriented from right to left. Errors are estimated to be maximum 65 counts for the highest intensity values (excluded from graphs for the sake of clarity).

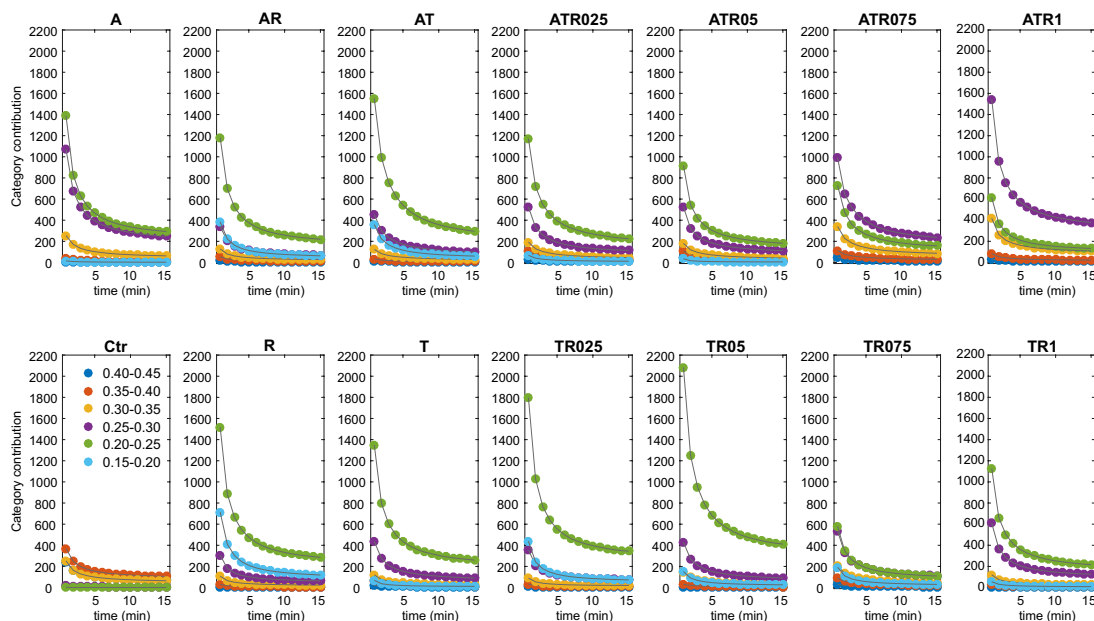


**Figure 5.14:** Contributions of the pixels in a given category to the overall fluorescence intensity for all samples in the F1 spectral range. Mean fluorescence intensities were weighted by the fraction of the number of pixels in the corresponding category. The weighted fluorescence signals belonging to the category in 0.40-0.45 are represented in blue, 0.35-0.40 in orange, 0.30-0.35 in yellow, 0.25-0.30 in violet, 0.20-0.25 in green and 0.15-0.20 in light blue. The sample notations are given in the title of each graph.

Moreover, it becomes dominant for the Huh-ATR075 sample and especially for the Huh-ATR1 sample. The fluorescence signals in the 0.30-0.35 category shows the same tendency among the samples as 0.25-0.30 with the increase in the riboflavin concentration.

Similar situation is in the case of weighted signal contributions in the F2 spectral range, presented in Figure 5.15. Besides different time-dependencies, the intensities are generally lower in the F2 spectral range than in the F1 range. The weighted fluorescence evolutions are in the agreement with the previously drawn conclusions made for the F1 range. However, mentioned discrepancies in the fluorescence behaviour of the sample Huh-TR075 compared to the other Huh-TRx samples are also present. Additionally, the behaviour of the fluorescent signals of the cancer cells treated with bare gold nanoparticles is specific. Generally, the fluorescence intensities of the Huh-A sample are comparable to the values obtained for Huh-ATR1 and Huh-ATR075 samples, even though there are no added fluorophores. Further

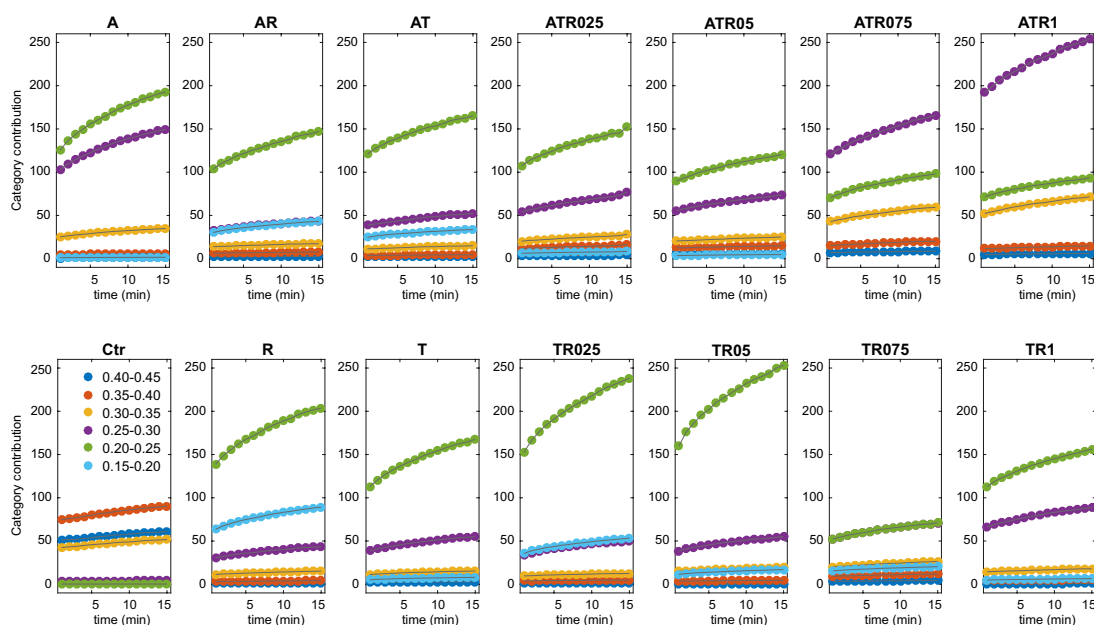


**Figure 5.15:** Contributions of the pixels in a given category to the overall fluorescence intensity for all samples in the F2 spectral range. Mean fluorescence intensities were weighted by fraction of the number of pixels in the corresponding category. Category contributions in 0.40-0.45 are represented in blue, 0.35-0.40 in orange, 0.30-0.35 in yellow colour, 0.25-0.30 in violet, 0.20-0.25 in green and 0.15-0.20 in light blue. Sample names are given in the title of each graph.

studies will be made to elucidate the influence of bare gold nanoparticles on the fluorescence dynamic of the endogenous fluorophores present in human cancer cell lines.

Additionally, we wanted to check how fluorescence intensities are distributed at the initial time point of the acquisition. A  $\delta N_{F1}$  - weighted fluorescence intensity in the F2 spectral range at the first time point for each sample separated by the photobleaching dynamics (i.e. the categories) is presented in Figure 5.16. The bars represent weighted intensity intervals of the fluorescence in each category. The idea is to analyse the intensities in F2 range (riboflavin filter), prior to complete photobleaching of tryptophan. Weighted fluorescence in every category gives insight into mutual relations between the samples in the F2 range. During the fluorescence activity of the tryptophan, the RET process is the most pronounced. Also, the increase in the riboflavin fluorescence is expected as its concentration in the samples increases. Obviously, the expected ordering of the samples Huh-(A)TR<sub>x</sub> by their

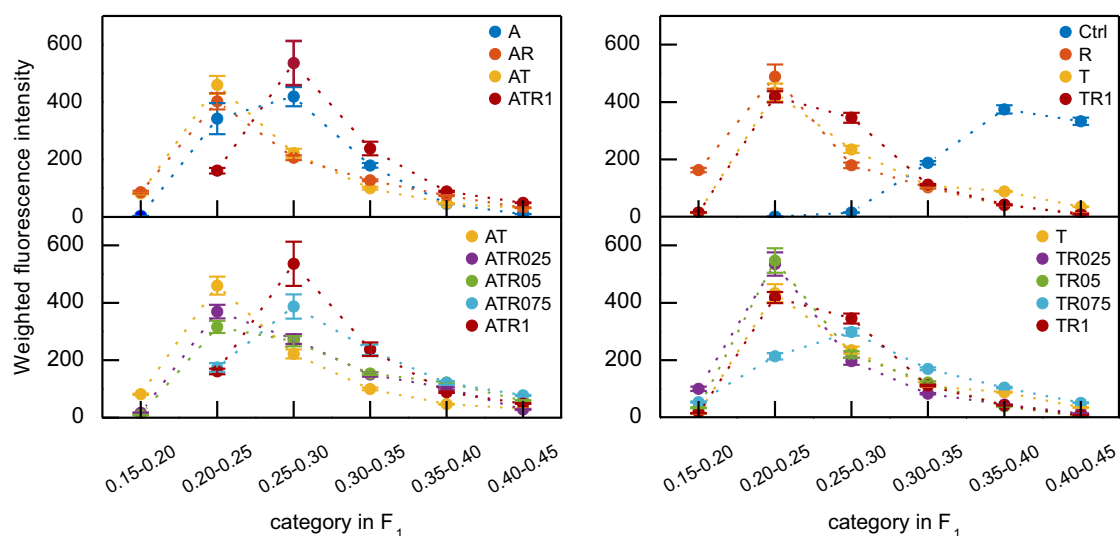


**Figure 5.16:** Weighted fluorescence intensity of the Huh7.5 cell samples in the F2 spectral region at the first time point in the categories based on the photobleaching dynamics. Bars represent intervals of the weighted fluorescence intensity in each category. The samples are denoted as following: A/Ctr - dark blue, (A)R - orange, (A)T - yellow, (A)TR025 - violet, (A)TR05 - green, (A)TR075 - light blue, (A)TR1 - maroon. Dashed lines are added for the easier overview.

fluorescence intensity is present in the 0.25-0.30 category. Also, in this category, the largest difference in the fluorescence intensity between Huh-AR and Huh-ATR1 sample was observed, although the concentration of the riboflavin in the samples was the same. In both cases, Huh-ATRx and Huh-TRx, as the concentration of riboflavin increases, the signal increases. So, the last part of the analyses will be focused on fluorescence intensities in the 0.25-0.30 category.

The previous analysis based on the distribution of the number of pixels and the corresponding fluorescence intensities among the samples suggested that the most probable detection of bifunctionalized gold nanoparticles is in the 0.25-0.30 category, so we wanted to see if the same approach but in the F2 spectral range would support the previous findings. We used the same procedure for the pixel classifications previously explained for the F1 range. Unlike the signals in the F1, the intensities in the F2 range increase over time. We separated the fluorescence signals in the categories from the lowest to the highest increase, which imposed categories above 1, in the steps of 0.1. Note that the samples Huh-ATR1 and Huh-ATR075 manifested the lowest intensity increment compared to the other samples.

This indicates that the classification is supposed to be opposite - instead of looking for the highest normalized saturation values, the fluorescence signals coming from bifunctionalized nanomaterial in the incubated cells would be of lower saturation values. A detailed analysis of the F2 signals evolutions showed that there were only few pixels belonging in F2 category below 1.1 (concerning only cytoplasmic region and excluding exterior of the cells) and are exclusively located on the very borders of the cells. The very next category showed pixels spread throughout the cells, indicating inhomogeneity in the origins of the fluorescence signal located in the cells interior.

The results of this analysis are presented for the samples Huh-ATR1, Huh-ATR075 and Huh control in Figure 5.17. The visible and the fluorescence images acquired in the F1 spectral range are overlaid with masks obtained for the F1 category 0.25 - 0.30, F2 category 1.10 - 1.20, as well as the overlap of the two. For the control sample there were almost no selected pixels in the 0.25 - 0.30 F1 category, as it can be seen in Figure 5.11. Even though the pixels belonging to the F2 category 1.1 - 1.2 are distributed throughout the cytoplasmic region, the overlap of the two masks shows that there are no pixels behaving with this particulate PB dynamic. On the other hand, the F1 category mask is covering area that is close to the cells border, with a tendency of selecting pixels toward the interior for the Huh-ATR1 and Huh-ATR075 samples. As for the F2 category, the selection can be separated in two subareas - the first is highlighting the cells border and the second is spread out in the cytoplasmic region. Finally, the overlap of these two masks points out the areas of desired behaviour in both spectral ranges. Detailed inspection of the overlap shows again two areas - close to border and in the cells interior. The images done in transmission mode (visible images) refute that the selection in the overlap is due to lack of biological material. Bearing in mind that there were no pixels selected by using these conditions in the control sample, the results of the analyses of the Huh-ATR1 and Huh-ATR075 samples strongly suggest that this signal is coming from the bifunctionalized gold nanoparticles. These findings imply the internalization of the nanomaterial into the cytoplasmic space and elucidate on the region of their localization that was the objective of this study.

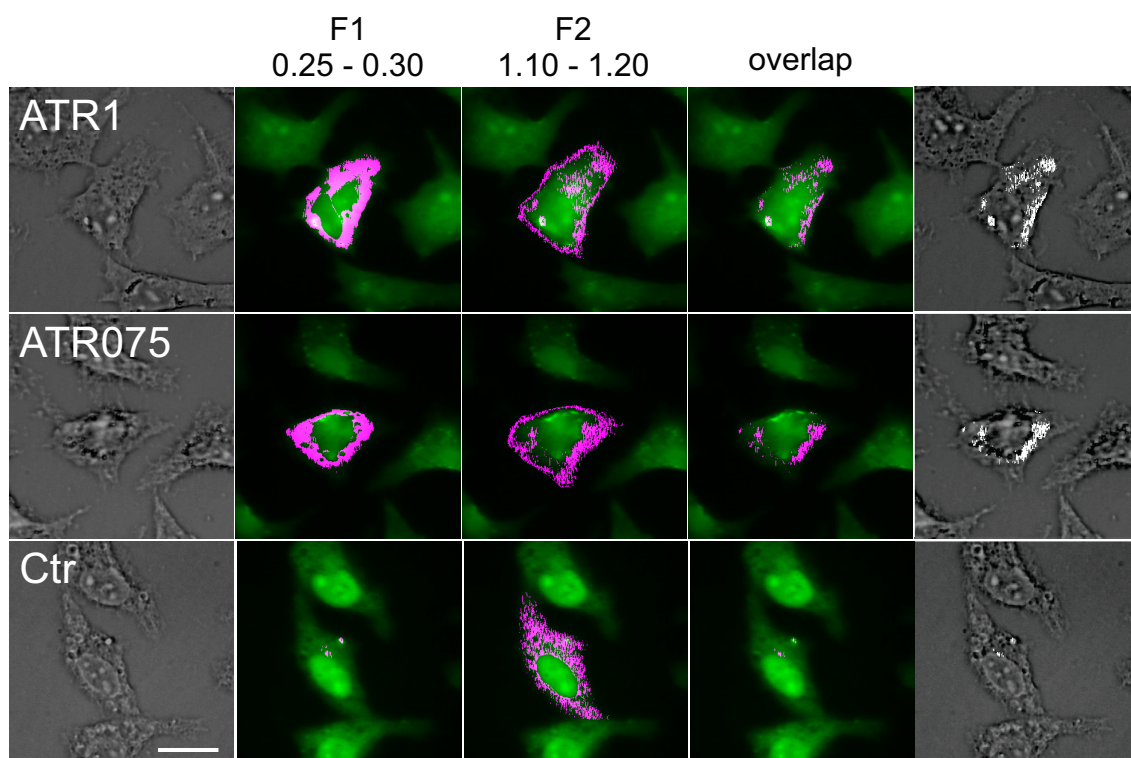


**Figure 5.17:** Visible (first column) and fluorescence images obtained in the F1 spectral range of the Huh-ATR1 (first row), Huh-ATR075 (second row) and Huh-Ctr (third row) samples overlaid with category masks in F1 (0.20 - 0.30, second column) and F2 (1.10 - 1.20, third column), and their overlap on the fluorescence images recorded in F1 spectral range (fourth column) and the visible images (fifth column). Scale bar represents 30  $\mu\text{m}$ .

---

The results demonstrate the detection-versatility of functionalized metal-based nanomaterial in research of their interaction with the biological material. The spectral properties of functionalized nanoparticles enable use of wide spectrum of experimental approaches. The research of their interaction with biological material is possible even by using conventional microscopy techniques of much lower resolution than the physical dimensions of the nanomaterial. Not only that fluorescent metal nanoparticles influence the fluorescence signals of the biomaterial, but they show different spectral dynamics than the untreated cells. This important characteristic can be employed as an additional detection modality in biomedical research, as it can be fruitful source of information.

---

# Chapter 6

## Conclusion

In this dissertation, we present the results of the investigation of the photoexcitation processes in hybrid nanostructures obtained by functionalization of gold nanoparticles with fluorescent biomolecules tryptophan and riboflavin. These fluorescent nanomaterials were also used as fluorescent probes for imaging of bacteria *Escherichia coli*, fungus *Candida albicans* and human hepatocellular carcinoma-derived cell line Huh7.5.1. An attempt was made to elucidate preferential locations of nanoparticle accumulation in these biological systems.

Fluorescent nanostructures were prepared by mixing of the colloid of bare gold nanoparticles with solutions of amino acid tryptophan and/or vitamin riboflavin. The morphology of the functionalized particles was investigated by means of transmission electron microscopy (TEM). TEM images of functionalized gold nanoparticles revealed that the initial spherical shape of the bare gold nanoparticles is preserved after the functionalization. It was found that the average size of the nanoparticles is approximately 8 nm regardless of the biomolecule used in functionalization process.

The study of the biomolecule-gold interactions by Raman spectroscopy suggested the potential functional groups of the biomolecules that participated in the interaction with gold surfaces. It was shown that tryptophan interacts with gold nanoparticles *via* indole part of the molecule, which is similar to the interaction of the biomolecule with gold macroscopic surfaces. In the case of riboflavin, the results strongly suggested that interaction of riboflavin with gold nanoparticles is *via* its



benzene rings, implying that the molecule is tilted with the respect to the gold surface. The Raman spectroscopy of the tryptophan-riboflavin bifunctionalized gold nanoparticles showed the presence of the normal modes of both biomolecules. Also, no other biomolecular adducts were observed before nor after the functionalization.

Vacuum-ultraviolet photoelectron spectroscopy (VUV-PES) measurements on isolated functionalized nanoparticles were employed to determine their valence-level electron structure and follow the changes in the electronic configuration of the components upon functionalization. The photoelectron spectrum of bare gold nanoparticles showed a slight shift of the work function with respect to the reported results for macroscopic crystals, which was explained as a combined effect of the Coulomb charge and small size of the particles. In addition, the  $6s$  and  $5d$  bands were also observed, confirming successful detection of valence electron density of states of gold nanoparticles in gas phase, without any contribution from the substrate. The results of the VUV-PES of free-standing functionalized gold nanoparticles confirmed that the biomolecules were indeed adsorbed on the surfaces of gold nanoparticles, offering important information on the valence band alignment of the constituents. The slight band shifts toward lower binding energies were observed in photoelectron spectra of the tryptophan-functionalized gold nanoparticles with the respect to the pure tryptophan solution. The observed shift was attributed to the vacuum level decrease suggested in studies on photoelectron spectroscopy of organic layers deposited onto gold surfaces. The additional shift toward lower binding energies detected for the Au  $5d$  band was explained *via* redistribution of the valence gold electrons due to the presence of the adsorbed tryptophan molecules. The photoelectron spectra of riboflavin solution and riboflavin-functionalized gold nanoparticles showed that the gold nanoparticles affect the valence electron spectra of the biomolecule in a similar way as in the case of tryptophan-gold nanostructure. Finally, the photoelectron spectra of bifunctionalized gold nanoparticles exhibited the mixed features of the spectra of all three constituents.

The results of photoluminescent spectroscopy of the functionalized nanoparticles showed that the fluorescent properties of the biomolecules were preserved after the functionalization. The absorbance and fluorescence spectra of the bifunctionalized

nanomaterial supported previously drawn conclusion that tryptophan and riboflavin do not interact and do not create new products during the mixing stage i.e. they interact with gold nanoparticles in their pure forms. Also, tryptophan and riboflavin are a specific pair of molecules where resonance energy transfer may occur under exposure to excitation radiation. The transfer efficiency from tryptophan to riboflavin was analysed after the fluorophores were attached onto gold nanoparticles. It was found that the adsorbed fluorophores exhibited more efficient transfer than in the case when they are free in the solutions. This is probably a consequence of the reduced distance between the biomolecules when they are attached onto surfaces of the nanoparticles.

After detailed investigation of the photoexcitation processes, single- and bi functionalized gold nanoparticles were tested as fluorescent probes for deep-ultraviolet (DUV) microscopy of various biological cell lines. Tryptophan-functionalized gold nanoparticles were successfully used in imaging of bacteria *Escherichia coli*. It was found that after incubation with the nanostructures there was an increase in fluorescence signals in the spectral region that corresponds to the tryptophan emission. The average intensity of the fluorescence of the nanoparticle - treated cells were approximately 2.5 times higher than that obtained from the control sample. The detailed investigation of the spatial distribution of the fluorescence signal with the single cell resolution indicated that the functionalized gold nanoparticles were internalized by the bacteria through their double membranes. These results suggested that the tryptophan-functionalized gold nanoparticles can potentially be used as fluorescence probes for bioimaging of bacteria. In the study of fungus *Candida albicans* incubated with riboflavin-gold nanostructures, the fluorescent signal attributed to the nanostructure was detected by using multiple excitations that enabled the presence of riboflavin molecule. The spatial distribution of the obtained fluorescent signal strongly suggested that the hybrid nanostructures interact with membranes of *Candida albicans* cells, but that they were not internalized by the fungus. The obtained results showed that the functionalization of gold nanoparticles by riboflavin was a good route toward fabrication of hybrid nanostructures suitable for DUV imaging of glutaraldehyde-fixed cell cultures. Additionally, we employed the pho-

---

to bleaching imaging technique to investigate Huh7.5.1 liver cancer cells incubated with gold nanoparticles bifunctionalized by both tryptophan and riboflavin. The bifunctionalized metal nanoplatforms presented in this study enabled an additional possibility to study the nanoprobe-cell interactions, since it exhibits a distinct fluorescence dynamic compared to typical fluorophores present in biological samples. The main advantage of this specific nanomaterial was based on the fact that presence of gold nanoparticles elevated the efficiency of the resonance energy transfer that was taking place between tryptophan and riboflavin molecules. This effect was successfully used as a basis for the separation of the fluorescence signals that is coming from the nanostructures from the autofluorescence of the cells. The employed procedure enabled the localization of the nanostructures in the cytoplasmic regions of treated Huh7.5.1 cells.

The obtained results in DUV fluorescence imaging suggest that using biomolecule functionalized metal nanoparticles as the fluorescent nanoprobes may offer additional information about the nature of the interaction of the nanostructured particles with the biological material. The spectral properties of functionalized nanoparticles allow for the use of a number of strategies for the analyses in the field of bioimaging. The approach developed in the present study enabled the detection and localization of the nanostructures in the cells, although microscopy technique employed here did not have sufficient resolution to distinguish objects of such sizes. It was demonstrated that fluorescent metal nanoparticles increase the overall intensity of the fluorescence signals of the cells after the incubation, while, at the same time, there is a change in fluorescence dynamics with respect to that of the untreated cells. We strongly believe that the suggested approach might be a fruitful source of information in bioimaging research, and we plan on continuing its development in our future work. Along this lines, we plan on exploring the multimodality of bioconjugated gold nanoparticles for photodynamic and photothermal applications in bionanotechnology.

---

# Bibliography

- [1] Yiwei Tan, Yongfang Li, and Daoben Zhu. *Noble metal nanoparticles*, volume 7. American Scientific Publishers, 2004.
- [2] Alaaldin M. Alkilany and Catherine J. Murphy. Toxicity and cellular uptake of gold nanoparticles: What we have learned so far? *Journal of Nanoparticle Research*, 12(7):2313–2333, 2010.
- [3] K. Saha, S.S. Agasti, C Kim, X Li, and V.M. Rotello. Gold nanoparticles in chemical and biological sensing. *Chemical reviews*, 112(5):2739–2779, 2012.
- [4] D. Michael P. Mingos. *Historical introduction to gold colloids, clusters and nanoparticles*. Springer International Publishing, 2014.
- [5] Susie Eustis and Mostafa A El-Sayed. Why gold nanoparticles are more precious than pretty gold: noble metal surface plasmon resonance and its enhancement of the radiative and nonradiative properties of nanocrystals of different shapes. *Chemical society reviews*, 35(3):209–217, 2006.
- [6] Ravi Shukla, Vipul Bansal, Minakshi Chaudhary, Atanu Basu, Ramesh R. Bhonde, and Murali Sastry. Biocompatibility of gold nanoparticles and their endocytotic fate inside the cellular compartment: A microscopic overview. *Langmuir*, 21(23):10644–10654, 2005.
- [7] Nastassja Lewinski, Vicki Colvin, and Rebekah Drezek. Cytotoxicity of nanoparticles. *Small*, 4(1):26–49, 2008.
- [8] Pekka Pyykkö. Theoretical chemistry of gold. *Angewandte Chemie - International Edition*, 43(34):4412–4456, 2004.
- [9] Pekka Pyykkö. Theoretical chemistry of gold. ii. *Inorganica chimica acta*, 358(14):4113–4130, 2005.
- [10] Pekka Pyykkö. Theoretical chemistry of gold. III. *Chemical Society Reviews*, 37(9):1967, 2008.

- 
- [11] Miguel Larginho and Pedro V. Baptista. Gold and silver nanoparticles for clinical diagnostics - From genomics to proteomics. *Journal of Proteomics*, 75(10):2811–2823, 2012.
- [12] Adam D McFarland and Richard P Van Duyne. Single silver nanoparticles as real-time optical sensors with zeptomole sensitivity. *Nano letters*, 3(8):1057–1062, 2003.
- [13] Srujan K. Dondapati, Tapan K. Sau, Calin Hrelescu, Thomas A. Klar, Fernando D. Stefani, and Jochen Feldmann. Label-free biosensing based on single gold nanostars as plasmonic transducers. *ACS Nano*, 4(11):6318–6322, 2010.
- [14] P. D. Howes, R. Chandrawati, and M. M. Stevens. Colloidal nanoparticles as advanced biological sensors. *Science*, 346(6205):1247390–1247390, 2014.
- [15] Otto S. Wolfbeis. An overview of nanoparticles commonly used in fluorescent bioimaging. *Chemical Society Reviews*, 44(14):4743–4768, 2015.
- [16] Lai-Kwan Chau and Huan-Tsung Chang, editors. *From bioimaging to biosensors*. Pan Stanford Publishing, 2012.
- [17] Eduardo Moros, editor. *Physics of thermal therapy: fundamentals and clinical applications*. CRC Press, Boca Raton, 2012.
- [18] Martina E. Wieder, Duncan C. Hone, Michael J. Cook, Madeleine M. Handley, Jelena Gavrilović, and David A. Russell. Intracellular photodynamic therapy with photosensitizer-nanoparticle conjugates: cancer therapy using a 'Trojan horse'. *Photochemical and Photobiological Sciences*, 5(8):727–734, 2006.
- [19] Kaspar Haume, Soraia Rosa, Sophie Grellet, Małgorzata A. Śmiałek, Karl T. Butterworth, Andrey V. Solov'yov, Kevin M. Prise, Jon Golding, and Nigel J. Mason. Gold nanoparticles for cancer radiotherapy: a review. *Cancer Nanotechnology*, 7(1):8, 2016.
- [20] Maung Kyaw Khaing Oo, Yamin Yang, Yue Hu, Maria Gomez, Henry Du, and Hongjun Wang. Gold nanoparticle-enhanced and size-dependent generation of reactive oxygen species from protoporphyrin ix. *ACS nano*, 6(3):1939–1947, 2012.

- 
- [21] Nikhil R. Jana, Nandan Erathodiyil, Jiang Jiang, and Jackie Y. Ying. Cysteine-functionalized polyaspartic acid: A polymer for coating and bio-conjugation of nanoparticles and quantum dots. *Langmuir*, 26(9):6503–6507, 2010.
- [22] Wen Zhou, Xia Gao, Dingbin Liu, and Xiaoyuan Chen. Gold nanoparticles for in vitro diagnostics. *Chemical Reviews*, 115(19):10575–10636, 2015.
- [23] Catherine Bréchnignac, Philippe Houdy, and Marcel Lahmani. *Nanomaterials and nanochemistry*. Springer - Verlag Berlin Heidelberg, 2007.
- [24] Miguel Valcárcel and Ángela I López-Lorente. *Gold nanoparticles in analytical chemistry*, volume 66. Elsevier, 2014.
- [25] John Blackman. *Metallic nanoparticles*, volume 5. Elsevier, 2008.
- [26] Roy L Johnston and J P Wilcoxon, editors. *Frontiers of nanoscience: metal nanoparticles and nanoalloys*, volume 3. Elsevier Ltd., 2012.
- [27] Hubert Schmidbaur. *Gold chemistry: applications and future directions in the life sciences*. John Wiley & Sons, 2009.
- [28] Pekka Pyykkö and Jean Paul Desclaux. Relativity and the periodic system of elements. *Accounts of Chemical Research*, 12(8):276–281, 1979.
- [29] Katharine Page, Thomas Proffen, Humberto Terrones, Mauricio Terrones, Lily Lee, Yan Yang, Susanne Stemmer, Ram Seshadri, and Anthony K. Cheetham. Direct observation of the structure of gold nanoparticles by total scattering powder neutron diffraction. *Chemical Physics Letters*, 393(4-6):385–388, 2004.
- [30] MG Ramchandani. Energy band structure of gold. *Journal of Physics C: Solid State Physics*, 3(1S):S1, 1970.
- [31] D. A. Shirley. High-resolution X-ray photoemission spectrum of the valence bands of gold. *Physical Review B*, 5(12):4709–4714, 1972.
- [32] DE Eastman and JK Cashion. Photoemission from Cu, Ag, and Au in the 10 to 27 eV energy range. *Physical Review Letters*, 24(7):310, 1970.
- [33] P. H. Citrin, G. K. Wertheim, and Y. Baer. Core-level binding energy and density of states from the surface atoms of gold. *Physical Review Letters*, 41(20):1425–1428, 1978.

- 
- [34] P. H. Citrin and G. K. Wertheim. Photoemission from surface-atom core levels, surface densities of states, and metal-atom clusters: A unified picture. *Physical Review B*, 27(6):3176–3200, 1983.
- [35] P. Heimann, J. F. van der Veen, and D. E. Eastman. Structure-dependent surface core level shifts for the Au(111), (100), and (110) surfaces. *Solid State Communications*, 38(7):595–598, 1981.
- [36] Anton Visikovskiy, Hisashi Matsumoto, Kei Mitsuhara, Toshitaka Nakada, Tomoki Akita, and Yoshiaki Kido. Electronic *d*-band properties of gold nanoclusters grown on amorphous carbon. *Physical Review B - Condensed Matter and Materials Physics*, 83(16):1–9, 2011.
- [37] H. Hövel, B. Grimm, M. Pollmann, and B. Reihl. Cluster-substrate interaction on a femtosecond time scale revealed by a high-resolution photoemission study of the Fermi-level onset. *Physical Review Letters*, 81(21):4608–4611, 1998.
- [38] Akinori Tanaka, Yuitsu Takeda, Tazumi Nagasawa, Hiroyuki Sasaki, Yosuke Kuriyama, Shoji Suzuki, and Shigeru Sato. Photoemission study of metallic nanoparticles passivated by dodecanethiolates: silver nanoparticles. *Surface science*, 532:281–286, 2003.
- [39] Neil W. Ashcroft and N. David Mermin. *Solid state physics*. Philadelphia, PA: Saunders, 1976.
- [40] Fabio. Della Sala and Stefania D’Agostino. *Handbook of molecular plasmonics*. Pan Stanford Publishing, 2013.
- [41] Catherine Bréchnignac, Philippe Houdy, and Marcel Lahmani. *Nanomaterials and nanochemistry*. Springer Science & Business Media, 2008.
- [42] Anastasiya Derkachova, Krystyna Kolwas, and Iraidia Demchenko. Dielectric function for gold in plasmonics applications: size dependence of plasmon resonance frequencies and damping rates for nanospheres. *Plasmonics*, 11(3):941–951, 2016.
- [43] Andreas Trügler. *Optical properties of metallic nanoparticles*. Springer International Publishing, 2016.
- [44] Craig F Bohren and D.R. Huffman. *Absorption and Scattering of Light by Small Particles*. Wiley, New York, 1983.

- 
- [45] Chris D. Geddes, editor. *Metal-enhanced fluorescence*. John Wiley & Sons, Inc., may 2010.
- [46] Joel Gersten and Abraham Nitzan. Spectroscopic properties of molecules interacting with small dielectric particles. *The Journal of Chemical Physics*, 75(3):1139–1152, 1981.
- [47] R. Ruppin. Decay of an excited molecule near a small metal sphere. *The Journal of Chemical Physics*, 76(4):1681–1684, 1982.
- [48] Joel I. Gersten and Abraham Nitzan. Accelerated energy transfer between molecules near a solid particle. *Chemical Physics Letters*, 104(1):31–37, 1984.
- [49] D. A. Weitz, S. Garoff, J. I. Gersten, and A. Nitzan. The enhancement of Raman scattering, resonance Raman scattering, and fluorescence from molecules adsorbed on a rough silver surface. *The Journal of Chemical Physics*, 78(9):5324–5338, 1983.
- [50] Chris D. Geddes, editor. *Surface plasmon enhanced, coupled and controlled fluorescence*. John Wiley & Sons, Inc., 2017.
- [51] Felicia Tam, P. Glenn Goodrich, R. Bruce Johnson, and J. Naomi Halas. Plasmonic enhancement of molecular fluorescence. *Nano Letters*, 7(2):496, 2007.
- [52] Zhenpeng Zhou, Hongduan Huang, Yang Chen, Feng Liu, Cheng Zhi Huang, and Na Li. A distance-dependent metal-enhanced fluorescence sensing platform based on molecular beacon design. *Biosensors and Bioelectronics*, 52:367–373, 2014.
- [53] Zhenpeng Zhou, Tian Li, Hongduan Huang, Yang Chen, Feng Liu, Chengzhi Huang, and Na Li. A dual amplification strategy for DNA detection combining bio-barcode assay and metal-enhanced fluorescence modality. *Chemical Communications*, 50(87):13373–13376, 2014.
- [54] Shan Jiang, Khin Yin Win, Shuhua Liu, Choon Peng Teng, Yuangang Zheng, and Ming-Yong Han. Surface-functionalized nanoparticles for biosensing and imaging-guided therapeutics. *Nanoscale*, 5(8):3127, 2013.
- [55] Detlef Schroder, Helmut Schwarz, Jan Hrusak, and Pekka Pykkö. Cationic gold(I) complexes of xenon and of ligands containing the donor atoms oxygen. *Inorganic Chemistry*, 37(1):624–632, 1998.
-



- 
- [56] Ton V.W. Janssens, Bjerne S. Clausen, Britt Hvolbæk, Hanne Falsig, Claus H. Christensen, Thomas Bligaard, and Jens K. Nørskov. Insights into the reactivity of supported Au nanoparticles: Combining theory and experiments. *Topics in Catalysis*, 44(1-2):15–26, 2007.
- [57] Carl S. Weisbecker, Margaret V. Merritt, and George M. Whitesides. Molecular self-assembly of aliphatic thiols on gold colloids. *Langmuir*, 12(16):3763–3772, 1996.
- [58] Louis Catherine and Pluchery Olivier. *Gold nanoparticles for physics, chemistry and biology*. World Scientific, 2012.
- [59] L. Barrio, P. Liu, J. A. Rodríguez, J. M. Campos-Martín, and J. L.G. Fierro. A density functional theory study of the dissociation of H<sub>2</sub> on gold clusters: Importance of fluxionality and ensemble effects. *Journal of Chemical Physics*, 125(16), 2006.
- [60] Laura Barrio, Ping Liu, Jose A. Rodriguez, Jose M. Campos-Martin, and Jose L G Fierro. Effects of hydrogen on the reactivity of O<sub>2</sub> toward gold nanoparticles and surfaces. *Journal of Physical Chemistry C*, 111(51):19001–19008, 2007.
- [61] Ton VW Janssens, Bjerne S Clausen, Britt Hvolbæk, Hanne Falsig, Claus H Christensen, Thomas Bligaard, and Jens K Nørskov. Insights into the reactivity of supported Au nanoparticles: combining theory and experiments. *Topics in Catalysis*, 44(1-2):15, 2007.
- [62] Noko S Phala and Eric Van Steen. Intrinsic reactivity of gold nanoparticles: Classical, semi-empirical and dft studies. *Gold Bulletin*, 40(2):150–153, 2007.
- [63] N. Lopez, T. V.W. Janssens, B. S. Clausen, Y. Xu, M. Mavrikakis, T. Bligaard, and J. K. Nørskov. On the origin of the catalytic activity of gold nanoparticles for low-temperature CO oxidation. *Journal of Catalysis*, 223(1):232–235, 2004.
- [64] Jennifer L. Brennan, Nikos S. Hatzakis, T. Robert Tshikhudo, Nijole Dirvian-skyte, Valdemaras Razumas, Shamkant Patkar, Jesper Vind, Allan Svendsen, Roeland J.M. Nolte, Alan E. Rowan, and Mathias Brust. Bionanoconjugation via click chemistry: The creation of functional hybrids of lipases and gold nanoparticles. *Bioconjugate Chemistry*, 17(6):1373–1375, 2006.
- [65] Tae Joon Cho, Rebecca A Zangmeister, Robert I MacCuspie, Anil K Patri, and Vincent A Hackley. Newkome-type dendron-stabilized gold nanoparticles:
-

- 
- Synthesis, reactivity, and stability. *Chemistry of materials*, 23(10):2665–2676, 2011.
- [66] Maurie E Garcia, Lane A Baker, and Richard M Crooks. Preparation and characterization of dendrimer- gold colloid nanocomposites. *Analytical chemistry*, 71(1):256–258, 1999.
- [67] Daniel V. Leff, Lutz Brandt, and James R. Heath. Synthesis and characterization of hydrophobic, organically-soluble gold nanocrystals functionalized with primary amines. *Langmuir*, 12(20):4723–4730, 1996.
- [68] Andrea BR Mayer and James E Mark. Colloidal gold nanoparticles protected by cationic polyelectrolytes. *Journal of Macromolecular Science, Part A: Pure and Applied Chemistry*, 34(11):2151–2164, 1997.
- [69] Dušan K Božanić, Adriaan S Luyt, Lidija V Trandafilović, and Vladimir Djoković. Glycogen and gold nanoparticle bioconjugates: controlled plasmon resonance via glycogen-induced nanoparticle aggregation. *RSC Advances*, 3(23):8705–8713, 2013.
- [70] R Griffith Freeman, Katherine C Grabar, Keith J Allison, Robin M Bright, Jennifer A Davis, Andrea P Guthrie, Michael B Hommer, Michael A Jackson, Patrick C Smith, and Daniel G Walter. Self-assembled metal colloid monolayers: an approach to SERS substrates. *Science*, 267(5204):1629–1632, 1995.
- [71] Kevin B. Stavens, Stephen V. Puzstay, Shouzhong Zou, Ronald P. Andres, and Alexander Wei. Encapsulation of neutral gold nanoclusters by resorcinarenes. *Langmuir*, 15(24):8337–8339, 1999.
- [72] Marie Christine Mc. Daniel and Didier Astruc. Gold nanoparticles: assembly, supramolecular chemistry, quantum-size related properties and applications toward biology, catalysis and nanotechnology. *Chemical Reviews*, 104:293–346, 2004.
- [73] Katherine C. Grabar, Keith J. Allison, Bonnie E. Baker, Robin M. Bright, Kenneth R. Brown, R. Griffith Freeman, Audrey P. Fox, Christine D. Keating, Michael D. Musick, and Michael J. Natan. Two-dimensional arrays of colloidal gold particles: a flexible approach to macroscopic metal surfaces. *Langmuir*, 12(10):2353–2361, 1996.
- [74] Andrew N. Shipway, Michal Lahav, and Itamar Willner. Nanostructured gold colloid electrodes. *Advanced Materials*, 12(13):993–998, 2000.
-

- 
- [75] T. Sato and H. Ahmed. Observation of a Coulomb staircase in electron transport through a molecularly linked chain of gold colloidal particles. *Applied Physics Letters*, 70(20):2759–2761, 1997.
- [76] Toshihiko Sato, Haroon Ahmed, David Brown, and Brian F.G. Johnson. Single electron transistor using a molecularly linked gold colloidal particle chain. *Journal of Applied Physics*, 82(2):696–701, 1997.
- [77] P Ghosh. Intracellular delivery of a membrane-impermeable enzyme in active form using functionalized gold nanoparticles. *Journal of the American Chemical Society*, 132(11):2642–2645, 2010.
- [78] Yu Tao, Zhenhua Li, Enguo Ju, Jinsong Ren, and Xiaogang Qu. Polycations-functionalized water-soluble gold nanoclusters: A potential platform for simultaneous enhanced gene delivery and cell imaging. *Nanoscale*, 5(13):6154–6160, 2013.
- [79] Jeff WM Bulte and Michel Modo. *Nanoparticles in biomedical imaging: emerging technologies and applications*, volume 3. Springer Science & Business Media, 2007.
- [80] Rosa Di Felice and Annabella Selloni. Adsorption modes of cysteine on Au(111): Thiolate, amino-thiolate, disulfide. *Journal of Chemical Physics*, 120(10):4906–4914, 2004.
- [81] a H Pakiari and Z Jamshidi. Interaction of amino acids with gold and silver clusters. *The journal of physical chemistry. A*, 111:4391–4396, 2007.
- [82] Prachi Joshi, Vasundhara Shewale, Ravindra Pandey, Virendra Shanker, Saber Hussain, and Shashi P. Karna. Tryptophan-gold nanoparticle interaction: A first-principles quantum mechanical study. *Journal of Physical Chemistry C*, 115(46):22818–22826, 2011.
- [83] Shafqat Hussain and Yoonsoo Pang. Surface geometry of tryptophan adsorbed on gold colloidal nanoparticles. *Journal of Molecular Structure*, 1096:121–128, 2015.
- [84] Marco P. Monopoli, Christoffer Åberg, Anna Salvati, and Kenneth A. Dawson. Biomolecular coronas provide the biological identity of nanosized materials. *Nature Nanotechnology*, 7(12):779–786, 2012.
- [85] Iseult Lynch and Kenneth A. Dawson. Protein-nanoparticle interactions. *Nano Today*, 3(1-2):40–47, 2008.
-

- 
- [86] Hua Jin Zhai and Lai Sheng Wang. Chemisorption sites of CO on small gold clusters and transitions from chemisorption to physisorption. *Journal of Chemical Physics*, 122(5):2005–2008, 2005.
- [87] Ching W Tang and Steven A VanSlyke. Organic electroluminescent diodes. *Applied physics letters*, 51(12):913–915, 1987.
- [88] A.R. Brown, D.D.C. Bradley, J.H. Burroughes, R.H. Friend, N.C. Greenham, P.L. Burn, A.B. Holmes, and A.M. Kraft. Light-emitting diodes based on conjugated polymers, 1992.
- [89] Jayesh M. Bharathan and Yang Yang. Polymer/metal interfaces and the performance of polymer light-emitting diodes. *Journal of Applied Physics*, 84(6):3207–3211, 1998.
- [90] J. S. Kim, M. Granström, R. H. Friend, N. Johansson, W. R. Salaneck, R. Daik, W. J. Feast, and F. Cacialli. Indium–tin oxide treatments for single- and double-layer polymeric light-emitting diodes: The relation between the anode physical, chemical, and morphological properties and the device performance. *Journal of Applied Physics*, 84(12):6859–6870, dec 1998.
- [91] Annica Andersson, Nicklas Johansson, Per Bröms, Nu Yu, Donald Lupo, and William R. Salaneck. Fluorine tin oxide as an alternative to indium tin oxide in polymer LEDs. *Advanced Materials*, 10(11):859–863, 1998.
- [92] Martin Oehzelt, Norbert Koch, and Georg Heimel. Organic semiconductor density of states controls the energy level alignment at electrode interfaces. *Nature Communications*, 5(May):1–8, 2014.
- [93] Marco Gruenewald, Laura K. Schirra, Paul Winget, Michael Kozlik, Paul F. Ndione, Ajaya K. Sigdel, Joseph J. Berry, Roman Forker, Jean Luc Brédas, Torsten Fritz, and Oliver L.A. Monti. Integer charge transfer and hybridization at an organic semiconductor/conductive oxide interface. *Journal of Physical Chemistry C*, 119(9):4865–4873, 2015.
- [94] Hisao Ishii, Kiyoshi Sugiyama, Eisuke Ito, and Kazuhiko Seki. Energy level alignment and interfacial electronic structures at organic/metal and organic/organic interfaces. *Advanced materials*, 11(8):605–625, 1999.
- [95] Suphiya Parveen, Ranjita Misra, and Sanjeeb K. Sahoo. Nanoparticles: A boon to drug delivery, therapeutics, diagnostics and imaging. *Nanomedicine: Nanotechnology, Biology, and Medicine*, 8(2):147–166, 2012.
-

- 
- [96] Karrina McNamara and Syed A. M. Tofail. Nanoparticles in biomedical applications. *Advances in Physics: X*, 2(1):54–88, 2017.
- [97] Hrushikesh M. Joshi, Devika R. Bhumkar, Kalpana Joshi, Varsha Pokharkar, and Murali Sastry. Gold nanoparticles as carriers for efficient transmucosal insulin delivery. *Langmuir*, 22(1):300–305, 2006.
- [98] Chong H Ahn, Boris Anczykowski, MZ Atashbar, W Bacsa, WS Bainbridge, A Baldi, PD Barnes, J Batteas, R Bennewitz, and B Bhushan. *Springer handbook of nanotechnology*. Springer, 2004.
- [99] Peter Schuck. Use of surface plasmon resonance to probe the equilibrium and dynamic aspects of interactions between biological macromolecules. *Annual Review of Biophysics and Biomolecular Structure*, 26(1):541–566, 1997.
- [100] R J Fisher and M Fivash. Surface plasmon resonance based methods for measuring the kinetics and binding affinities of biomolecular interactions. *Current opinion in biotechnology*, 5(4):389–395, 1994.
- [101] Lev A Dykman, Yaroslav M Krasnov, Vladimir A Bogatyrev, and Nikolai G Khlebtsov. Quantitative immunoassay method based on the extinction spectra of colloidal gold bioconjugates. In *Saratov Fall Meeting 2000: Optical Technologies in Biophysics and Medicine II*, volume 4241, pages 37–42. International Society for Optics and Photonics, 2001.
- [102] Robert Elghanian, James J. Storhoff, Robert C. Mucic, Robert L. Letsinger, and Chad A. Mirkin. Selective colorimetric detection of polynucleotides based on the distance-dependent optical properties of gold nanoparticles. *Science*, 277(5329):1078–1081, 1997.
- [103] L Andrew Lyon, Michael D Musick, and Michael J Natan. Colloidal Au-enhanced surface plasmon resonance immunosensing. *Science*, 70(24):5177–5183, 1998.
- [104] Lev A. Dykman, Vladimir A. Bogatyrev, Boris N. Khlebtsov, and Nikolai G. Khlebtsov. A protein assay based on colloidal gold conjugates with trypsin. *Analytical Biochemistry*, 341(1):16–21, 2005.
- [105] Kenneth R. Brown, Audrey P. Fox, and Michael J. Natan. Morphology-dependent electrochemistry of cytochrome c at Au colloid-modified SnO<sub>2</sub> electrodes. *Journal of the American Chemical Society*, 118(5):1154–1157, jan 1996.

- 
- [106] Anand Gole, Chandravanu Dash, Vidya Ramakrishnan, S. R. Sainkar, A. B. Mandale, Mala Rao, and Murali Sastry. Pepsin-gold colloid conjugates: Preparation, characterization, and enzymatic activity. *Langmuir*, 17(5):1674–1679, 2001.
- [107] Chad A. Mirkin, Robert L. Letsinger, Robert C. Mucic, and James J. Storhoff. A DNA-based method for rationally assembling nanoparticles into macroscopic materials. *Nature*, 382(6592):607–609, 1996.
- [108] Avinash Bajaj, Oscar R. Miranda, Ronnie Phillips, Ik Bum Kim, D. Joseph Jerry, Uwe H.F. Bunz, and Vincent M. Rotello. Array-based sensing of normal, cancerous, and metastatic cells using conjugated fluorescent polymers. *Journal of the American Chemical Society*, 132(3):1018–1022, 2010.
- [109] Chang Cheng You, Oscar R. Miranda, Basar Gider, Partha S. Ghosh, Ik Bum Kim, Belma Erdogan, Sai Archana Krovi, Uwe H.F. Bunz, and Vincent M. Rotello. Detection and identification of proteins using nanoparticle-fluorescent polymer 'chemical nose' sensors. *Nature Nanotechnology*, 2(5):318–323, 2007.
- [110] Ronnie L. Phillips, Oscar R. Miranda, Chang-Cheng You, Vincent M. Rotello, and Uwe H. F. Bunz. Rapid and efficient identification of bacteria using gold-nanoparticle–poly(para-phenyleneethynylene) constructs. *Angewandte Chemie International Edition*, 47(14):2590–2594, 2008.
- [111] A Bajaj, O R Miranda, I B Kim, R L Phillips, D J Jerry, U H F Bunz, and V M Rotello. Detection and differentiation of normal, cancerous, and metastatic cells using nanoparticle-polymer sensor arrays. *Proceedings of the National Academy of Sciences of the United States of America*, 106(27):10912–10916, 2009.
- [112] W Page Faulk and G Malcolm Taylor. Communication to the editors: an immunocolloid method for the electron microscope. *Immunochemistry*, 8(11):1081–1083, 1971.
- [113] René Hermann, Paul Walther, and M. Müller. Immunogold labeling in scanning electron microscopy. *Histochemistry and Cell Biology*, 106(1):31–39, 1996.
- [114] W Baschong and NG Wrigley. Small colloidal gold conjugated to fab fragments or to immunoglobulin g as high-resolution labels for electron microscopy: a technical overview. *Journal of electron microscopy technique*, 14(4):313–323, 1990.

- 
- [115] Dean A Handley, Cynthia M Arbeeny, Larry D Witte, and Shu Chien. Colloidal gold–low density lipoprotein conjugates as membrane receptor probes. *Proceedings of the National Academy of Sciences*, 78(1):368–371, 1981.
- [116] Cristina Neagu, KO Van der Werf, CAJ Putman, YM Kraan, BG De Grooth, NF Van Hulst, and J Greve. Analysis of immunolabeled cells by atomic force microscopy, optical microscopy, and flow cytometry. *Journal of structural biology*, 112(1):32–40, 1994.
- [117] Dean A Handley and Shu Chien. Colloidal gold: a pluripotent receptor probe. *Proceedings of the Society for Experimental Biology and Medicine*, 174(1):1–11, 1983.
- [118] Adalberto Merighi and Laura Lossi, editors. *Immunocytochemistry and related techniques*. Springer, New York, 2015.
- [119] Steven D Schwartzbach, Omar Skalli, and Thomas Schikorski. *High-resolution imaging of cellular proteins*. Springer, New York, 2016.
- [120] Chen Zhou, Shengyang Yang, Jinbin Liu, Mengxiao Yu, and Jie Zheng. Luminescent gold nanoparticles: A new class of nanoprobes for biomedical imaging. *Experimental Biology and Medicine*, 238(11):1199–1209, 2013.
- [121] Sharbari Palmal and Nikhil R. Jana. Gold nanoclusters with enhanced tunable fluorescence as bioimaging probes. *Wiley Interdisciplinary Reviews: Nanomedicine and Nanobiotechnology*, 6(1):102–110, 2014.
- [122] Hua He, Chao Xie, and Jicun Ren. Non-bleaching fluorescence of gold nanoparticles and its applications in cancer cell. *Analytical Chemistry*, 80(15):5951–5957, 2008.
- [123] Jie Zheng, Chen Zhou, Mengxiao Yu, and Jinbin Liu. Different sized luminescent gold nanoparticles. *Nanoscale*, 4(14):4073, 2012.
- [124] Robert B.P. Elmes, Kim N. Orange, Suzanne M. Cloonan, D. Clive Williams, and Thorfinnur Gunnlaugsson. Luminescent ruthenium(II) polypyridyl functionalized gold nanoparticles; Their DNA binding abilities and application as cellular imaging agents. *Journal of the American Chemical Society*, 133(40):15862–15865, 2011.
- [125] Aleksandra Jaworska, Tomasz Wojcik, Kamilla Malek, Urszula Kwolek, Mariusz Kepczynski, Abu A. Ansary, Stefan Chlopicki, and Malgorzata Baranska.

- 
- Rhodamine 6G conjugated to gold nanoparticles as labels for both SERS and fluorescence studies on live endothelial cells. *Microchimica Acta*, 182(1-2):119–127, 2015.
- [126] Doyeon Kim, Nuri Oh, Kyoohyun Kim, SangYun Lee, Chan-Gi Pack, Ji-Ho Park, and YongKeun Park. Label-free high-resolution 3-D imaging of gold nanoparticles inside live cells using optical diffraction tomography. *Methods*, 2017.
- [127] Bradley Duncan, Chaekyu Kim, and Vincent M. Rotello. Gold nanoparticle platforms as drug and biomacromolecule delivery systems. *Journal of Controlled Release*, 148(1):122–127, 2010.
- [128] Subinoy Rana, Avinash Bajaj, Rubul Mout, and Vincent M. Rotello. Monolayer coated gold nanoparticles for delivery applications. *Advanced Drug Delivery Reviews*, 64(2):200–216, 2012.
- [129] Sarah D. Brown, Paola Nativo, Jo-Ann Smith, David Stirling, Paul R. Edwards, Balaji Venugopal, David J. Flint, Jane A. Plumb, Duncan Graham, and Nial J. Wheate. Gold nanoparticles for the improved anticancer drug delivery of the active component of oxaliplatin. *Journal of the American Chemical Society*, 132(13):4678–4684, 2010.
- [130] Jingyuan Li, Xuemei Wang, Chunxia Wang, Baoan Chen, Yongyuan Dai, Renyun Zhang, Min Song, Gang Lv, and Degang Fu. The enhancement effect of gold nanoparticles in drug delivery and as biomarkers of drug-resistant cancer cells. *ChemMedChem: Chemistry Enabling Drug Discovery*, 2(3):374–378, 2007.
- [131] Steven K. Libutti, Giulio F. Paciotti, Adriana A. Byrnes, H. Richard Alexander, William E. Gannon, Melissa Walker, Geoffrey D. Seidel, Nargiza Yuldasheva, and Lawrence Tamarkin. Phase I and pharmacokinetic studies of CYT-6091, a novel PEGylated colloidal gold-rhTNF nanomedicine. *Clinical Cancer Research*, 16(24):6139–6149, 2010.
- [132] Wei-Chieh Huang, Pei-Jane Tsai, and Yu-Chie Chen. Functional gold nanoparticles as photothermal agents for selective-killing of pathogenic bacteria. *Nanomedicine*, 2(6):777–787, 2007.
- [133] Bernard Valeur and Mário Nuno Berberan-Santos. *Molecular fluorescence: principles and applications*. John Wiley & Sons, 2012.
-



- 
- [134] Peter Jomo Walla. *Modern biophysical chemistry: detection and analysis of biomolecules*. John Wiley & Sons, 2014.
- [135] Alexander Govorov, Pedro Ludwig Hernández, Martínez Hilmi, and Volkan Demir. *Understanding and modeling Förster-type resonance energy transfer (FRET)*, volume 1. Springer, 2016.
- [136] Gregory D. Scholes. Long-range resonance energy transfer in molecular systems. *Annual Review of Physical Chemistry*, 54(1):57–87, oct 2003.
- [137] Akbar Salam. *Molecular quantum electrodynamics: long-range intermolecular interactions*. John Wiley & Sons, 2010.
- [138] D. L. Andrews. A unified theory of radiative and radiationless molecular energy transfer. *Chemical Physics*, 135(2):195–201, 1989.
- [139] R. M. Young, J. K. Arnette, D. A. Roess, and B. G. Barisas. Quantitation of fluorescence energy transfer between cell surface proteins via fluorescence donor photobleaching kinetics. *Biophysical Journal*, 67(2):881–888, 1994.
- [140] Yuansheng Sun, Richard N Day, and Ammasi Periasamy. Investigating protein-protein interactions in living cells using fluorescence lifetime imaging microscopy. *Nature protocols*, 6(9):1324, 2011.
- [141] Ralph A Bradshaw and Edward A Dennis. *Handbook of cell signaling*. Academic press, 2009.
- [142] Peter J. Verveer, editor. *Advanced fluorescence microscopy*. Springer New York, 2015.
- [143] C. Dinant, M. E. Van Royen, W. Vermeulen, and A. B. Houtsmuller. Fluorescence resonance energy transfer of GFP and YFP by spectral imaging and quantitative acceptor photobleaching. *Journal of Microscopy*, 231(1):97–104, 2008.
- [144] Tomasz Zal and Nicholas R.J. Gascoigne. Photobleaching-corrected FRET efficiency imaging of live cells. *Biophysical Journal*, 86(6):3923–3939, 2004.
- [145] X. M. Hua, J. I. Gersten, and A. Nitzan. Theory of energy transfer between molecules near solid state particles. *The Journal of Chemical Physics*, 83(7):3650–3659, 1985.

- 
- [146] Tuncay Ozel, Pedro Ludwig Hernandez-Martinez, Evren Mutlugun, Onur Akin, Sedat Nizamoglu, Ilkem Ozge Ozel, Qing Zhang, Qihua Xiong, and Hilmi Volkan Demir. Observation of selective plasmon-exciton coupling in nonradiative energy transfer: donor-selective versus acceptor-selective plexcitons. *Nano letters*, 13(7):3065–3072, 2013.
- [147] Manuela Lunz, Valerie A Gerard, Yurii K Gun’ko, Vladimir Lesnyak, Nikolai Gaponik, Andrei S Susha, Andrey L Rogach, and A Louise Bradley. Surface plasmon enhanced energy transfer between donor and acceptor cdte nanocrystal quantum dot monolayers. *Nano letters*, 11(8):3341–3345, 2011.
- [148] Manuela Lunz, Xia Zhang, Valerie A Gerard, Yurii K Gun’ko, Vladimir Lesnyak, Nikolai Gaponik, Andrei S Susha, Andrey L Rogach, and A Louise Bradley. Effect of metal nanoparticle concentration on localized surface plasmon mediated Förster resonant energy transfer. *The Journal of Physical Chemistry C*, 116(50):26529–26534, 2012.
- [149] Cristian A. Marocico, Xia Zhang, and A. Louise Bradley. A theoretical investigation of the influence of gold nanosphere size on the decay and energy transfer rates and efficiencies of quantum emitters. *Journal of Chemical Physics*, 144(2), 2016.
- [150] Jian Zhang, Yi Fu, and Joseph R. Lakowicz. Enhanced förster resonance energy transfer (FRET) on a single metal particle. *The Journal of Physical Chemistry C*, 111(1):50–56, jan 2007.
- [151] Jian Zhang, Yi Fu, Mustafa H Chowdhury, and Joseph R Lakowicz. Enhanced förster resonance energy transfer on single metal particle. 2. dependence on donor- acceptor separation distance, particle size, and distance from metal surface. *The Journal of Physical Chemistry C*, 111(32):11784–11792, 2007.
- [152] Frank Reil, Ulrich Hohenester, Joachim R Krenn, and Alfred Leitner. Förster-type resonant energy transfer influenced by metal nanoparticles. *Nano Letters*, 8(12):4128–4133, 2008.
- [153] Lei Zhao, Tian Ming, Lei Shao, Huanjun Chen, and Jianfang Wang. Plasmon-controlled Förster resonance energy transfer. *The Journal of Physical Chemistry C*, 116(14):120328120034006, 2012.
- [154] Laurent Nahon, Nelson De Oliveira, Gustavo A. Garcia, Jean François Gil, Bertrand Pilette, Olivier Marcouillé, Bruno Lagarde, and François Polack.

- 
- DESIRS: A state-of-the-art VUV beamline featuring high resolution and variable polarization for spectroscopy and dichroism at SOLEIL. *Journal of Synchrotron Radiation*, 19(4):508–520, 2012.
- [155] François Gaie-Levrel, Gustavo A. Garcia, Martin Schwell, and Laurent Nahon. VUV state-selected photoionization of thermally-desorbed biomolecules by coupling an aerosol source to an imaging photoelectron/photoion coincidence spectrometer: case of the amino acids tryptophan and phenylalanine. *Physical Chemistry Chemical Physics*, 13(15):7024, 2011.
- [156] Héloïse Dossmann, Adrián Schwarzenberg, Denis Lesage, Marie Pérot-Taillandier, Carlos Afonso, Barbara Cunha de Miranda, and Gustavo A. Garcia. Vacuum ultraviolet photoionization study of gas phase vitamins A and B1 using aerosol thermodesorption and synchrotron radiation. *The Journal of Physical Chemistry A*, 118(47):11185–11192, nov 2014.
- [157] Gustavo A. Garcia, Laurent Nahon, Chris J. Harding, Elisabeth A. Mikajlo, and Ivan Powis. A refocusing modified velocity map imaging electron/ion spectrometer adapted to synchrotron radiation studies. *Review of Scientific Instruments*, 76(5):1–11, 2005.
- [158] Gustavo A. Garcia, Laurent Nahon, and Ivan Powis. Two-dimensional charged particle image inversion using a polar basis function expansion. *Review of Scientific Instruments*, 75(11):4989–4996, 2004.
- [159] Frederic Jamme, Sandrine Villette, Alexandre Giuliani, Valerie Rouam, Frank Wien, Bruno Lagarde, and Matthieu Réfrégières. Synchrotron UV fluorescence microscopy uncovers new probes in cells and tissues. *Microscopy and microanalysis*, 16(5):507–514, 2010.
- [160] A. Giuliani, P. Limão-Vieira, D. Dufflot, A. R. Milosavljević, B. P. Marinković, S. V. Hoffmann, N. Mason, J. Delwiche, and M. J. Hubin-Franskin. Electronic states of neutral and ionized tetrahydrofuran studied by VUV spectroscopy and ab initio calculations. *European Physical Journal D*, 51(1):97–108, 2009.
- [161] M. Réfrégières, F. Jamme, V. Rouam, F. Wien, A. Giuliani, S. Douix, F. Auvray, J. Pasquier, and C. Pisapia. DUV Fluorescence Microscopy on Telemos. *Journal of la Terrasse*, 120(18):2016–2018, 2016.
- [162] Arthur Edelstein, Nenad Amodaj, Karl Hoover, Ron Vale, and Nico Stuurman. Computer control of microscopes using  $\mu$ manager. *Current protocols in molecular biology*, 92(1):14–20, 2010.
-

- 
- [163] Julia Vergalli, Estelle Dumont, Jelena Pajović, Bertrand Cinquin, Laure Maire, Muriel Masi, Matthieu Réfrégiers, and Jean-Marie Pagés. Spectrofluorimetric quantification of antibiotic drug concentration in bacterial cells for the characterization of translocation across bacterial membranes. *Nature protocols*, 13(6):1348, 2018.
- [164] Johannes Schindelin, Ignacio Arganda-Carreras, Erwin Frise, Verena Kaynig, Mark Longair, Tobias Pietzsch, Stephan Preibisch, Curtis Rueden, Stephan Saalfeld, Benjamin Schmid, Jean Yves Tinevez, Daniel James White, Volker Hartenstein, Kevin Eliceiri, Pavel Tomancak, and Albert Cardona. Fiji: An open-source platform for biological-image analysis. *Nature Methods*, 9(7):676–682, 2012.
- [165] Jelena D Pajović, Radovan Dojčilović, Dušan K Božanić, Slavka Kaščáková, Matthieu Réfrégiers, Suzana Dimitrijević-Branković, Vesna V Vodnik, Aleksandar R Milosavljević, Emanuela Piscopiello, Adriaan S Luyt, and Vladimir Djokovic. Tryptophan-functionalized gold nanoparticles for deep UV imaging of microbial cells. *Colloids and Surfaces B: Biointerfaces*, 135:742–750, 2015.
- [166] M.M. Campos Vallette, R.G. Diaz F., A.M. Edwards, S. Kennedy, E. Silva, J. Derouault, and M. Rey-Lafon. Photo-induced generation of the riboflavin-tryptophan adduct and a vibrational interpretation of its structure. *Vibrational Spectroscopy*, 6(2):173–183, jan 1994.
- [167] Marcela Dendisová-Vyškovska, Alžběta Kokaislová, Milan Ončák, and Pavel Matějka. SERS and in situ SERS spectroscopy of riboflavin adsorbed on silver, gold and copper substrates. Elucidation of variability of surface orientation based on both experimental and theoretical approach. *Journal of Molecular Structure*, 1038:19–28, 2013.
- [168] Fangfang Liu, Huaimin Gu, Yue Lin, Yajing Qi, Xiao Dong, Junxiang Gao, and Tiantian Cai. Surface-enhanced Raman scattering study of riboflavin on borohydride-reduced silver colloids: Dependence of concentration, halide anions and pH values. *Spectrochimica Acta - Part A: Molecular and Biomolecular Spectroscopy*, 85(1):111–119, 2012.
- [169] Chi-Hung Chuang and Yit-Tsong Chen. Raman scattering of L-tryptophan enhanced by surface plasmon of silver nanoparticles: vibrational assignment and structural determination. *Journal of Raman Spectroscopy*, 40(2):150–156, 2009.

- 
- [170] Xiaolin Cao and Gad Fischer. Infrared spectral, structural and conformational studies of zwitterionic L-tryptophan. *Journal of Physical Chemistry A*, 103:9995–10003, 1999.
- [171] APHC Schmidt-Ott, P Schurtenberger, and HC Siegmann. Enormous yield of photoelectrons from small particles. *Physical Review Letters*, 45(15):1284, 1980.
- [172] Richard E Watson and Morris L Perlman. X-ray photoelectron spectroscopy application to metals and alloys. In *Photoelectron Spectrometry*, pages 83–132. Springer, 1975.
- [173] Lei Zhou and Michael R Zachariah. Size resolved particle work function measurement of free nanoparticles: Aggregates vs. spheres. *Chemical Physics Letters*, 525:77–81, 2012.
- [174] Carl Neil Berglund and William Edward Spicer. Photoemission studies of copper and silver: theory. *Physical Review*, 136(4A):A1030, 1964.
- [175] Antoine Kahn. Fermi level, work function and vacuum level. *Materials Horizons*, 3(1):7–10, 2016.
- [176] GV Hansson and SA Flodström. Photoemission study of the bulk and surface electronic structure of single crystals of gold. *Physical Review B*, 18(4):1572, 1978.
- [177] A. Sekiyama, J. Yamaguchi, A. Higashiya, M. Obara, H. Sugiyama, M. Y. Kimura, S. Suga, S. Imada, I. A. Nekrasov, M. Yabashi, K. Tamasaku, and T. Ishikawa. The prominent 5d-orbital contribution to the conduction electrons in gold. *New Journal of Physics*, 12:1–8, 2010.
- [178] Patrik R Callis.  $^1L_a$  and  $^1L_b$  transitions of tryptophan: Applications of theory and experimental observations to fluorescence of proteins. *Methods in enzymology*, 278:113–150, 1997.
- [179] Laura Zanetti-Polzi, Massimiliano Aschi, Isabella Daidone, and Andrea Amadei. Theoretical modeling of the absorption spectrum of aqueous riboflavin. *Chemical Physics Letters*, 669:119–124, 2017.
- [180] Ewa Sikorska, Igor Khmelinskii, Anna Komasa, Jacek Koput, Luis F V Ferreira, Jose R. Herance, Jose L. Bourdelande, Siân L. Williams, David R. Worrall, Małgorzata Insińska-Rak, and Marek Sikorski. Spectroscopy and

---

photophysics of flavin related compounds: Riboflavin and iso-(6,7)-riboflavin. *Chemical Physics*, 314(1-3):239–247, 2005.

- [181] E. Silva, V. Rückert, E. Lissi, and E. Abuin. Effects of pH and ionic micelles on the riboflavin-sensitized photoprocesses of tryptophan in aqueous solution. *Journal of Photochemistry and Photobiology B: Biology*, 11(1):57–68, oct 1991.
- [182] Jacob W Petrich, MC Chang, DB McDonald, and GR Fleming. On the origin of nonexponential fluorescence decay in tryptophan and its derivatives. *Journal of the American Chemical Society*, 105(12):3824–3832, 1983.
- [183] Pingping Li, Shaopu Liu, Xiaodan Wang, Zhengqing Liu, and Youqiu He. Fluorescence quenching studies on the interaction of riboflavin with tryptophan and its analytical application. *Luminescence*, 28(6):910–914, 2012.
- [184] Prashant K. Jain, Kyeong Seok Lee, Ivan H. El-Sayed, and Mostafa A. El-Sayed. Calculated absorption and scattering properties of gold nanoparticles of different size, shape, and composition: applications in biological imaging and biomedicine. *The Journal of Physical Chemistry B*, 110(14):7238–7248, apr 2006.
- [185] Kwahun Lee, Sungmoon Choi, Chun Yang, Hai-Chen Wu, and Junhua Yu. Autofluorescence generation and elimination: a lesson from glutaraldehyde. *Chemical Communications*, 49(29):3028–3030, 2013.
- [186] Jelena D Pajović, Radovan Dojčilović, Dušan K Božanić, Vesna V Vodnik, Suzana Dimitrijević-Branković, Slavka Kaščaková, Matthieu Réfrégiers, Milica Markelić, and Vladimir Djoković. Deep UV fluorescence imaging study of *Candida albicans* cells treated with gold-riboflavin hydrocolloids. *Optical and Quantum Electronics*, 48(6):311, 2016.
- [187] Ellen E. Connor, Judith Mwamuka, Anand Gole, Catherine J. Murphy, and Michael D. Wyatt. Gold nanoparticles are taken up by human cells but do not cause acute cytotoxicity. *Small*, 1(3):325–327, 2005.
- [188] Frédéric Jamme, Slavka Kaščaková, Sandrine Villette, Fatma Allouche, Stéphane Pallu, Valérie Rouam, and Matthieu Réfrégiers. Deep UV autofluorescence microscopy for cell biology and tissue histology. *Biology of the Cell*, 105(7):277–288, 2013.
- [189] Bertrand Cinquin, Laure Maigne, Elizabeth Pinet, Jacqueline Chevalier, Robert A Stavenger, Scott Mills, Matthieu Réfrégiers, and Jean-Marie Pagès.

---

Microspectrometric insights on the uptake of antibiotics at the single bacterial cell level. *Scientific reports*, 5:17968, 2015.

- [190] Sandrine Villette, Sophie Pigaglio-Deshayes, Christine Vever-Bizet, Pierre Validire, and Geneviève Bourg-Heckly. Ultraviolet-induced autofluorescence characterization of normal and tumoral esophageal epithelium cells with quantitation of NAD(P)H. *Photochemical & photobiological sciences*, 5(5):483–492, 2006.
- [191] Paola Nativo, Ian A Prior, and Mathias Brust. Uptake and intracellular fate of surface-modified gold nanoparticles. *ACS nano*, 2(8):1639–1644, 2008.

---

## Biography of the author

Jelena Pajović was born on May 31st, 1988, in Belgrade, Serbia. She graduated from Mathematical Grammar School in Belgrade in 2007. As a high school student, she participated in physics seminars at Petnica Science Center, an extracurricular educational center in Valjevo, Serbia. After high school, she enrolled in the Faculty of Physics at the University of Belgrade, department Theoretical and Experimental Physics. She obtained her BSc degree in 2011 (grade 9.85), and a year later her MSc degree (grade 9.67). During her studies, she was an assistant at Petnica Science Center, as well as a demonstrator (2007-2009) and a coordinator of two physics exhibitions (2010 and 2011) at the Science Festival, Belgrade. In 2010, she was on a two-month internship at Technische Universität Ilmenau, Germany.

She enrolled in the PhD study program (scientific field: Condensed matter physics and statistical physics) on the Faculty of Physics, University of Belgrade, as a part of the group of Dr Vladimir Đoković (Institute of nuclear sciences Vinča) in 2012. She was also a teaching assistant on the subjects Laboratory of Physics 1 & 2 in 2013 and 2014, as well as for the experimental part of the subject Solid state physics in 2014 at the Faculty of Physics. She continued her participation at Petnica Science Center, where she was head of the Physics seminar for two years. During her PhD studies, she participated in six research projects at Synchrotron Soleil (France). Between 2016 and 2018, she was on a research stay at DISCO beamline, synchrotron Soleil, on a European project TRANSLOCATION. She was involved in deep-ultraviolet fluorescence microscopy studies of antibiotic translocation through membranes of Gram-negative bacterial strains.

She is the author and coauthor of 10 scientific papers.



## Изјава о ауторству

Име и презиме аутора - Јелена Пајовић

Број индекса – 2012/8016

### Изјављујем

да је докторска дисертација под насловом

Biomolecule functionalized gold nanoparticles: photoexcitation processes and  
application in fluorescence microscopy

- резултат сопственог истраживачког рада;
- да дисертација у целини ни у деловима није била предложена за стицање друге дипломе према студијским програмима других високошколских установа;
- да су резултати коректно наведени и
- да нисам кршио/ла ауторска права и користио/ла интелектуалну својину других лица.

### Потпис аутора

У Београду, 30.07.2018.



---

## **Изјава о истоветности штампане и електронске верзије докторског рада**

Име и презиме аутора - Јелена Пајовић

Број индекса - 2012/8016

Студијски програм - Физика кондензоване материје и статистичка физика

Наслов рада - Biomolecule functionalized gold nanoparticles: photoexcitation processes and application in fluorescence microscopy

Ментор - др Душан К. Божанић


Изјављујем да је штампана верзија мог докторског рада истоветна електронској верзији коју сам предала ради похрањења у **Дигиталном репозиторијуму Универзитета у Београду**.

Дозвољавам да се објаве моји лични подаци везани за добијање академског назива доктора наука, као што су име и презиме, година и место рођења и датум одбране рада.

Ови лични подаци могу се објавити на мрежним страницама дигиталне библиотеке, у електронском каталогу и у публикацијама Универзитета у Београду.

**Потпис аутора**

У Београду, 30.07.2018.



---

## Изјава о коришћењу

Овлашћујем Универзитетску библиотеку „Светозар Марковић“ да у Дигитални репозиторијум Универзитета у Београду унесе моју докторску дисертацију под насловом:

Biomolecule functionalized gold nanoparticles: photoexcitation processes and application in fluorescence microscopy

која је моје ауторско дело.

Дисертацију са свим прилозима предао/ла сам у електронском формату погодном за трајно архивирање.

Моју докторску дисертацију похрањену у Дигиталном репозиторијуму Универзитета у Београду и доступну у отвореном приступу могу да користе сви који поштују одредбе садржане у одабраном типу лиценце Креативне заједнице (Creative Commons) за коју сам се одлучио/ла.

1. Ауторство (CC BY)
2. Ауторство – некомерцијално (CC BY-NC)
3. Ауторство – некомерцијално – без прерада (CC BY-NC-ND)
- 4. Ауторство – некомерцијално – делити под истим условима (CC BY-NC-SA)**
5. Ауторство – без прерада (CC BY-ND)
6. Ауторство – делити под истим условима (CC BY-SA)

(Молимо да заокружите само једну од шест понуђених лиценци.  
Кратак опис лиценци је саставни део ове изјаве).

**Потпис аутора**

У Београду, 30.07.2018.



---

1. **Ауторство.** Дозвољаваате умножавање, дистрибуцију и јавно саопштавање дела, и прераде, ако се наведе име аутора на начин одређен од стране аутора или даваоца лиценце, чак и у комерцијалне сврхе. Ово је најслободнија од свих лиценци.

2. **Ауторство – некомерцијално.** Дозвољаваате умножавање, дистрибуцију и јавно саопштавање дела, и прераде, ако се наведе име аутора на начин одређен од стране аутора или даваоца лиценце. Ова лиценца не дозвољава комерцијалну употребу дела.

3. **Ауторство – некомерцијално – без прерада.** Дозвољаваате умножавање, дистрибуцију и јавно саопштавање дела, без промена, преобликовања или употребе дела у свом делу, ако се наведе име аутора на начин одређен од стране аутора или даваоца лиценце. Ова лиценца не дозвољава комерцијалну употребу дела. У односу на све остале лиценце, овом лиценцом се ограничава највећи обим права коришћења дела.

4. **Ауторство – некомерцијално – делити под истим условима.** Дозвољаваате умножавање, дистрибуцију и јавно саопштавање дела, и прераде, ако се наведе име аутора на начин одређен од стране аутора или даваоца лиценце и ако се прерада дистрибуира под истом или сличном лиценцом. Ова лиценца не дозвољава комерцијалну употребу дела и прерада.

5. **Ауторство – без прерада.** Дозвољаваате умножавање, дистрибуцију и јавно саопштавање дела, без промена, преобликовања или употребе дела у свом делу, ако се наведе име аутора на начин одређен од стране аутора или даваоца лиценце. Ова лиценца дозвољава комерцијалну употребу дела.

6. **Ауторство – делити под истим условима.** Дозвољаваате умножавање, дистрибуцију и јавно саопштавање дела, и прераде, ако се наведе име аутора на начин одређен од стране аутора или даваоца лиценце и ако се прерада дистрибуира под истом или сличном лиценцом. Ова лиценца дозвољава комерцијалну употребу дела и прерада. Слична је софтверским лиценцама, односно лиценцама отвореног кода.